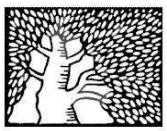

מכון ויצמן למדע
Weizmann Institute of Science

Thesis for the degree
Doctor of Philosophy

חיבור לשם קבלת התואר
דוקטור לפילוסופיה

by
Anders Levermann

מאת
אנדרס לוורמן

הפיסיקה של מיבנים פרקטליים: טרנספורמציות קונפורמיות של שדות לפלסיאנים ובילפלסיאנים

The physics of fractal patterns: Conformal transformations for Laplacian and bi-Laplacian fields

advised by
Prof. Itamar Procaccia

בהדרכת
פרופ' איתמר פרוקצ'יה

July 2003

יולי 2003

Submitted to the Scientific Council
of the Weizmann Institute of Science
Rehovot, Israel

מוגש למועצה המדעית של
מכון ויצמן למדע
רחובות, ישראל

Contents

1 Introduction

The presented thesis deals with the subject of pattern formation in nonlinear dynamical system. It follows two lines of research. One focus is the understanding of the statistical properties of two-dimensional Laplacian growth processes. The other is the development of a new tool for investigating the propagation of fractures in disordered media.

The evolution of an interface between two physical phases according to a harmonic field is called Laplacian growth. These growth processes have been under investigation, in different physical realizations, for more than a century [1-3]. A lot of insight has been gained due to experimental [4-11], numerical [12-19] and analytical [20-39] work. Despite this extensive investigation of Laplacian growth processes, they still provide a number of interesting and unsolved problems. One being the multi-fractal properties of their discreet, probabilistic and serial version, Diffusion Limited Aggregation (DLA) [3]. It has long been speculated [40-44] that the multi-fractal measure of DLA exhibits a phase transition, i.e. that there exists a critical value q_c such that the generalized fractal dimensions D_q [45] do not exist for $q < q_c$. The method of iterated conformal maps [46, 47] offers an analytic tool to calculate the probability field at an arbitrary position on a DLA cluster to machine precision. We are able to compute a converged fractal spectrum (sections 3.1 and 3.2) resolving probabilities as low as 10^{-35} which can not be probed by conventional techniques. Additionally, we are able to show that a phase transition exists and that the critical value, $q_c = -0.2 \pm 0.05$, is negative. By relating the value q_c to the dominating opening angle of the deepest fjords, we provide a physical reason for the extraordinary result of a negative q_c.

In an attempt to understand the relation of DLA to its continuous, deterministic and parallel analog [1, 2], we developed a model for continuous

Laplacian growth by the iteration of conformal maps (section 3.3 and [48]). With the help of this model we are able to *falsify* the long standing conjecture [13] that both growth processes belong to the same universality class, i.e. have the same fractal dimension D. We are able to show that the UV-regularized and parallel Laplacian growth process develops asymptotically two dimensional clusters and is therefore not fractal (sections 2.1.2 and 3.4). Since the newly developed model and DLA have the same UV-regularization we conjecture that the physical reason for the two dimensionality is the parallelity of the growth and does not originate from a particular kind of regularization (as for example surface tension).

The second focus of my work is the solution of elasticity problems around complex structures in two-dimensions. Propagating fractures exhibit dynamical instabilities that already, in two dimensions, result in roughened surfaces which show self-affine geometry [49-56]. Therefore a number of direct numerical attempts to compute the stress fields around complex structure have been made [57-62]. However the analytical treatment of the problem has mainly [63, 64] resorted to the investigation of regular fracture geometries due to the lack of an analytic description of the complicated structures arising [65-67]. A general method to model the front of crack propagation directly [68] has the disadvantage that it is not based on an energy- or force-balance and can therefore not be considered a first principle approach. Similar criticism applies to the description of the fractured material by a phase field which is coupled to the stress field [69-72]. Here the physical interpretation of the phase-field poses the main difficulty.

Based on the method of iterated conformal maps, we develop a way to solve linear elasticity problems in two dimensions around complicated structures given by the conformal map from the surface of the crack to the unit

circle (sections 4.1 and 4.2). Distinct from the situation of Laplacian growth this, in general, requires the solution of the bi-Laplace equation in two dimensions.

After computing the stress tensor around the structure we quasi-statically propagate the fracture. Given analytically the conformal map onto the crack we investigate its geometrical properties for different loadings at infinity (the so-called fracture modes I, II and III) and different rules for crack propagation.

In analogy to the Laplacian case (DLA) we introduce in section 4.3 a model for bi-Laplacian growth. In this case the loading is given by a liquid which presses into a two dimensional elastic media, replacing it through quasi-static fracturing events. The model serves as a limiting case for the displacement of visco-elastic media such as associated polymers, clays, foams etc. by a fluid [59, 73, 74], in cases where the Deborah number of the process is sufficiently high, i.e. when elastic phenomena dominate the viscous effects.

We propose these models as tools to verify possible candidates of the microscopic fracture dynamics such as plastic deformation and surface diffusion [75]. By comparing the resulting geometrical properties, one could identify, for example, onsets of instabilities and roughness exponents of the surfaces. As will be shown in sections 2.2.1 and 4.2, these geometrical properties depend on the rule for fracture propagation and can be compared with experiment in order to check microscopic theories.

The next section 2 gives the scope of the thesis. It is a survey through the articles in sections 3 and 4. The main results and conclusions are presented and some additional unpublished figures are shown. Section 5 contains a discussion including remarks on future work that is desirable to complement this thesis.

2 Scope of the thesis

2.1 Laplacian growth processes

Laplacian growth processes are defined through a potential $\mathcal{P}$ which fulfills Laplace's equation $\nabla^2\mathcal{P} = 0$ outside a domain while the domain is growing locally with a normal velocity v_n proportional to the gradient of $\mathcal{P}$

$$v_n \propto |\nabla\mathcal{P}| \,. \tag{1}$$

In order for the problem to be well-posed, the potential needs to fulfill certain conditions on the boundary of the domain which depend on the physical situation that is described. We consider only the case of a two-dimensional domain in order to be able to use complex functions.

One physical realization of Laplacian growth is the displacement of a more viscous fluid by a less viscous one in a narrow gap between two planes (Hele-Shaw cell [1, 7, 8]). In this case the potential is the pressure p in the displaced fluid. When the flux of fluid is constant, p decays logarithmically at infinity. Due to surface tension the pressure on the interface is proportional to the local curvature. The surface tension suppresses the growth of sharp edges in the interface. It therefore serves as a UV-regularization in the problem. In principle other, less physical, ways to regularize the flow are possible. In section 2.1.2 we introduce as an example the growth in terms of layers of particles. In this case the sharpest possible edge of the interface is given by the smallest particle in a layer.

The Hele-Shaw flow is a continuous and parallel evolution, in the sense that the interface advances time-continuously and simultaneously everywhere with a velocity $v_n \propto |\nabla p|$ (D'Arcy's law). Even though the dynamics is deterministic, it develops complicated shapes because smooth interfaces are

linearly unstable up to a wavenumber given by the surface tension (Saffman-Taylor instability [2]). We will discuss the relation of this parallel Laplacian growth with Diffusion Limited Aggregation (DLA) in section 2.1.2.

DLA is a probabilistic form of Laplacian growth involving diffusing particles. Initially one particle is placed at the center of a plane. Another particle starts to diffuse from infinity and sticks to the first particle upon arrival. Then another particle is released, iteratively growing a cluster. Since each particle starts only after the previous one has arrived, the probability density P for the particle fulfills Laplace's equation (time-independent diffusion equation). The boundary conditions are the same as in the Hele-Shaw cell in the limit of vanishing surface tension. The probability for a particle to arrive at a specific point $z(s)$ on the surface of a grown cluster is called its harmonic measure ρ_h and is given by the gradient of P.

$$\rho_h(s) \propto |\nabla P(z(s))| \tag{2}$$

Section 2.1.1 explains how to use the method of iterated conformal maps to compute the multi-fractal spectrum of this measure, to detect its phase transition and to provide a geometrical explanation for the transition point q_c.

2.1.1 The multi-fractal spectrum of the harmonic measure of Diffusion Limited Aggregation

The probability that a random walker will stick to a certain point $z(s)$ on a given DLA cluster, the harmonic measure, varies significantly along the surface of the cluster. It is very large at the tips, which shield off the fjords, reducing the probability of arrival there strongly. It is therefore impossible to use direct simulation techniques to measure the arrival probabilities at the fjords [40, 41].

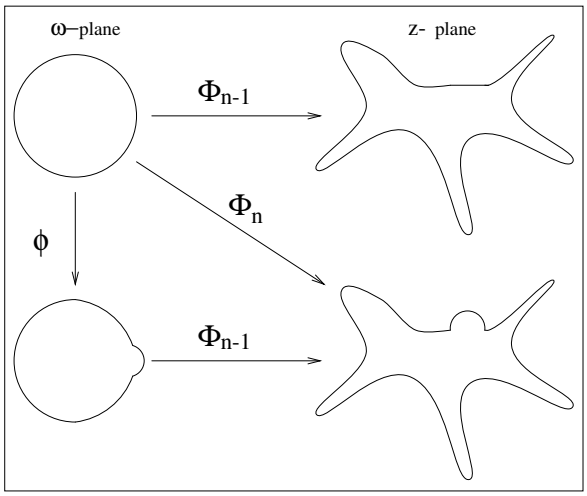

Figure 1: Iteration scheme for the construction of the conformal map on to a DLA cluster following Hastings and Levitov [46]

The method of iteration of conformal maps, introduced by Hastings and Levitov [46], on the other hand, provides an analytic expression for the surface of a DLA cluster and therefore makes it possible to compute the harmonic measure everywhere to machine precision.

The Hasting-Levitov algorithm is illustrated in figure 1 and goes as follows: assume that the conformal map Φ_{n-1} from the exterior of the unit circle to the exterior of a cluster with n-1 particles is given. We construct the map Φ_n to the exterior of a cluster with n particles by iteration with a fundamental map ϕ_n.

$$\Phi_n(w) = \Phi_{n-1}\left(\phi_n(w)\right) \tag{3}$$

The fundamental map ϕ_n adds onto the unit circle a small bump, representing a grown particle, with area λ_n and angular position θ_n. The potential P is then given by the inverse map

$$P(z) = \Re\left[\log\left(\Phi_n^{-1}(z)\right)\right] \tag{4}$$

and the growth measure transforms onto the uniform measure on the unit circle. Thus, if we choose the positions of the bumps θ_n uniformly random in $[0, 2\pi]$ we grow a DLA cluster. The areas λ_n are chosen such that the particles have equal size λ_0. The specific form of the fundamental map is not important as long as the bump is localized and has no tails on the circle. In our case this is achieved by two branch-points which mark the beginning and ending of the particle on the circle.

In order to compute the generalized fractal dimensions D_q for a cluster [45], we use the inverse maps of Φ_n to track the positions of these branch-cuts on the unit circle while growing the cluster (see section 3.1). After the cluster is grown we compute the harmonic measure ρ_h in between each neighboring pair of branch-cuts that was not covered by later particles. Figure 2 shows that by tracking the branch-cuts the entire geometry of a DLA cluster is resolved (right panel). By probing the cluster with random walkers (left panel) the fjords are practically never visited.

The images s_j of the positions between each pair of exposed branch-cuts have approximately the same distance on the cluster. By computing ρ_h in these positions, according to equation (2) we can obtain the fractal spectrum through the relation

$$\sum_j \rho_h^q(s_j) \sim n^{-(q-1)D_q/D} \tag{5}$$

which follows directly from its definition [45]. Some numerical difficulties have to be overcome because the branch-cuts representing the fjords of the cluster get closer and closer on the unit circle while the cluster is growing. Furthermore the values of the harmonic measure inside the fjords of a cluster of 30000 particles get as small as $\rho_h(fjord) \sim 10^{-35}$ which demands some numerical care (see section 3.2 for details.).

From the described procedure we obtained the fractal spectrum $\tau(q) =$

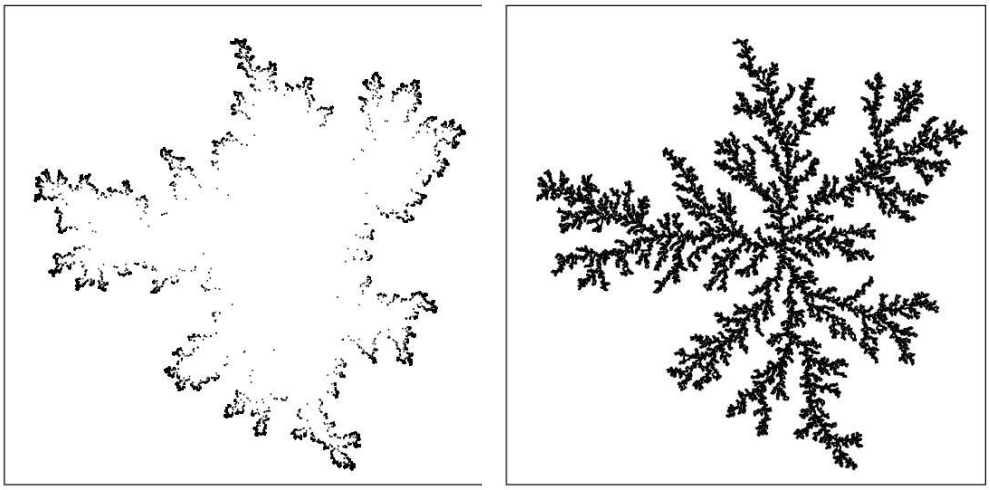

Figure 2: Left: probing a DLA cluster of 50000 particles with 50000 random walkers. The fjords of the structure are not resolved. right: plotting all exposed branch-cuts of the cluster resolves its entire geometry.

$(q-1)D_q$ as shown in figure 3 for increasing cluster sizes $n = 10000, 15000, 25000$ and 30000. The singularity spectrum $f(\alpha)$, i.e. the Legendre transform of $\tau(q)$ is shown for $n = 30000$ in figure 4. Both spectra are in agreement with previous analytical and numerical prediction for specific values of q and α. For example the fractal dimension D can be found in the spectra

$$D = D_0 = -\tau(0) = \max_{\alpha} f(\alpha) = \tau(3) \approx 1.71 \tag{6}$$

in agreement with the definition of D as D_0 [45], its value $D \approx 1.713$ [37] and the electrostatic law of Halsey [29]. Furthermore $\tau(1) = 0$ and $f'(1) = 1$ agree with the analytic result of Makarov [23] that $D_1 = 1$.

From the graphs of $\tau(q)$ and its second derivative in figure 3, it can be seen that $\tau(q)$ decreases without bound for $q < q_c = -0.2 \pm 0.05$ while the spectra are convergent for values of $q > q_c$. The value of q_c can be quantified by the slope of $f(\alpha)$ at the maximal α value for which $f(\alpha)$ exists, as seen in figure 4, the slope agrees with the value obtained from $\tau(q)$.

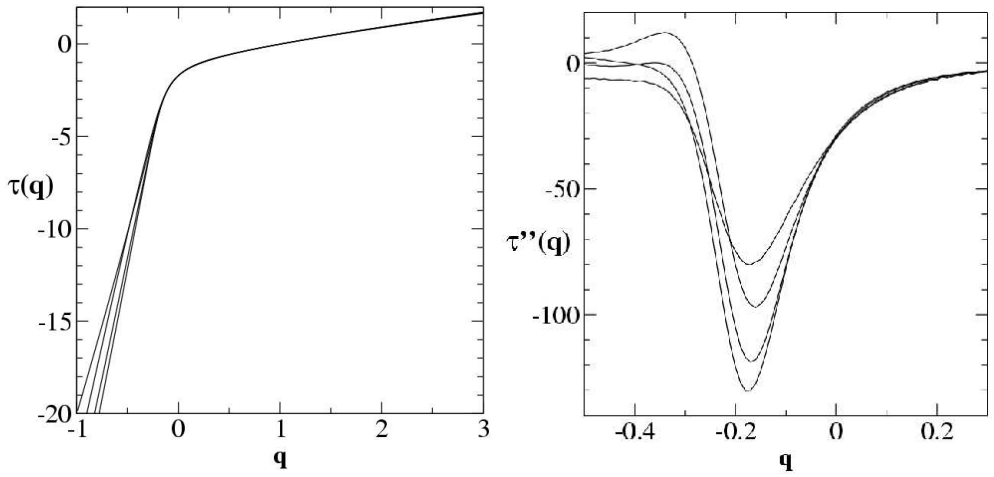

Figure 3: Left: fractal spectrum $\tau(q) = (q-1)D_q$ of the harmonic measure of DLA for increasing cluster sizes $n = 10000, 15000, 25000$ and 30000. The spectra are convergent for $q > q_c = -0.2 \pm 0.05$ while they are decreasing without bound for smaller values of q. right: the second derivative of $\tau(q)$ reveals the exact position of the phase transition.

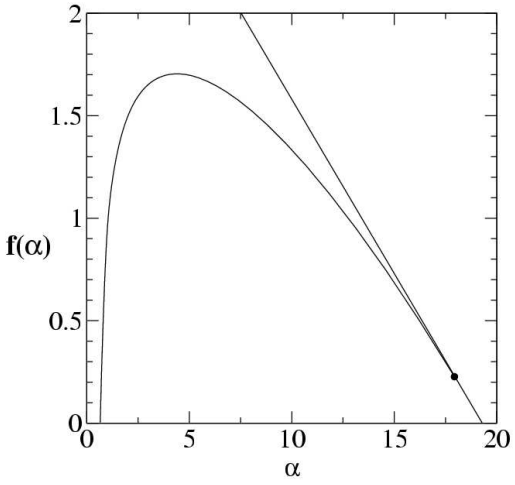

Figure 4: Singularity spectrum $f(\alpha)$ of the harmonic measure of DLA corresponding to the fractal spectrum of figure 3 for n=30000 particles. The $f(\alpha)$ ceases to exist for $\alpha > \alpha_{max} \approx 18$ corresponding to a phase transition in $\tau(q)$. The position of the transition at $q_c \approx -0.2$ is in agreement with the slope $f'(\alpha_{max}) = 0.18$ which is represented by the straight line.

In order to obtain a geometrical explanation for the position of the phase transition at a negative value of q_c we identified the regions on the cluster that provide support for the values of ρ_h that result in the phase transition (see section 3.2 for details.). We found that these regions show a wedge-like structure with a characteristic opening angle of $\gamma = 35° \pm 6°$. When translated to the critical value q_c of the fractal spectrum of an infinite wedge, we obtain $q_c = -0.24 \pm 0.05$ in agreement with the previous results. Note that the more common value of $q_c = 0$ corresponds to an opening-angle $\gamma = 0°$, i.e. to a channel geometry. Thus the local wedge-like structure of the deepest fjords of a DLA cluster provides the explanation for a phase transition at a negative $q_c = -0.2 \pm 0.05$.

2.1.2 The relation of serial and parallel Laplacian growth

In order to investigate the effect of parallel growth as opposed to the serial growth of DLA, we use the conformal mapping technique to construct a model with varying degree of parallelity (see [48] and section 3.3 for details).

In the model we grow not only one particle according to the harmonic measure of a cluster but a number of non-overlapping particles until a ratio $\mathcal{C}$ of the surface of the cluster is covered. $\mathcal{C} = 1$ corresponds to a full layer of non-overlapping particles. Only after choosing these particles we advance the surface and update the harmonic measure accordingly. Using this rule the averaged normal velocity on the cluster surface is no longer proportional to the harmonic measure. We therefore introduce a second parameter β which governs the relation of the particle size to the local harmonic measure (or local pressure gradient in the terminology of the Hele-Shaw cell). The particle size is given by

$$\text{area of particle at position } z \;\propto\; \rho_h(z)^\beta \;\propto\; |\nabla P(z)|^\beta \qquad (7)$$

i.e. for $\beta = 0$ we grow equal size particles while for $\beta = 2$ the *linear* local particle size is proportional to the harmonic measure (or the pressure gradient). This leaves us with a two parameter family of models where the combinations $(\beta = 0, \mathcal{C} = 0)$ and $(\beta = 2, \mathcal{C} = 1)$ correspond to DLA and parallel Laplacian growth, respectively[1]. The left panel of figure 5 shows clusters for $\beta = 0$ for two values of coverage. $\mathcal{C} = 0.01$ corresponds to a DLA cluster, since up to the shown cluster size of $n = 100000$ one particle per layer is enough to reach the prescibed coverage of $\mathcal{C} = 0.01$. Higher coverage of $\mathcal{C} = 0.5$ already results in two dimensional growth as seen in the right panel of figure 5. In figure 6 clusters are shown for $\beta = 2$ and the same coverages. Although we can not claim that the structure for $\mathcal{C} = 0.5$ is already two-dimensional, it is denser than the DLA cluster of figure 5.

By utilizing the first Laurent coefficient of the conformal map Φ_n as a measure for the radius of the cluster we obtained lower bounds for the fractal dimensions for varying values of $-1 \leq \beta \leq 2$ and $0 \leq \mathcal{C} \leq 0.65$ (see section 3.3). Figure 7 shows a phase diagram with lines which describe lower bounds for regions with fractal dimension equal to or higher than $D = 1.90, 1.95$ and 1.99 from top to bottom. By extrapolating to $\mathcal{C} = 1$ one can see that the model with $\beta = 2$ and $\mathcal{C} = 1$ is in fact two-dimensional and therefore not in the same universality class as DLA (see section 3.4). We conjecture that this property carries over to the case of continuous Laplacian growth in a Hele-Shaw cell. This is because the dimension of the β-$\mathcal{C}$-clusters serves as a lower bound for the continuous case, as can be seen from the following reasoning.

[1]For a discussion on the relationship between parallel Laplacian growth with $\beta = 2$ and $\mathcal{C} = 1$ and the Hele-Shaw flow in the limit of low surface tension paramenter see appendix B.

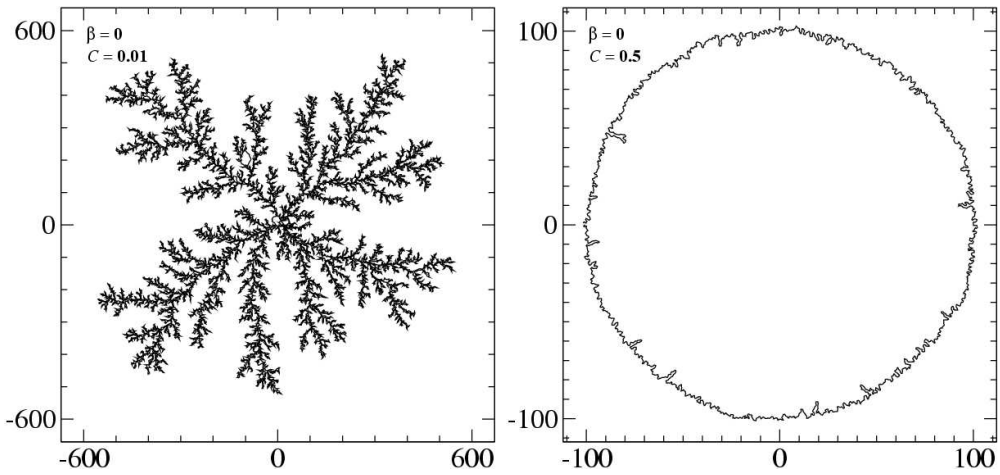

Figure 5: Clusters for $\beta = 0$: left: DLA cluster corresponding to minimal coverage of $\mathcal{C} = 0.01$ which up to the shown cluster size allows to grow only one particle per layer. right: two-dimensional growth resulting from high coverage of $\mathcal{C} = 0.5$

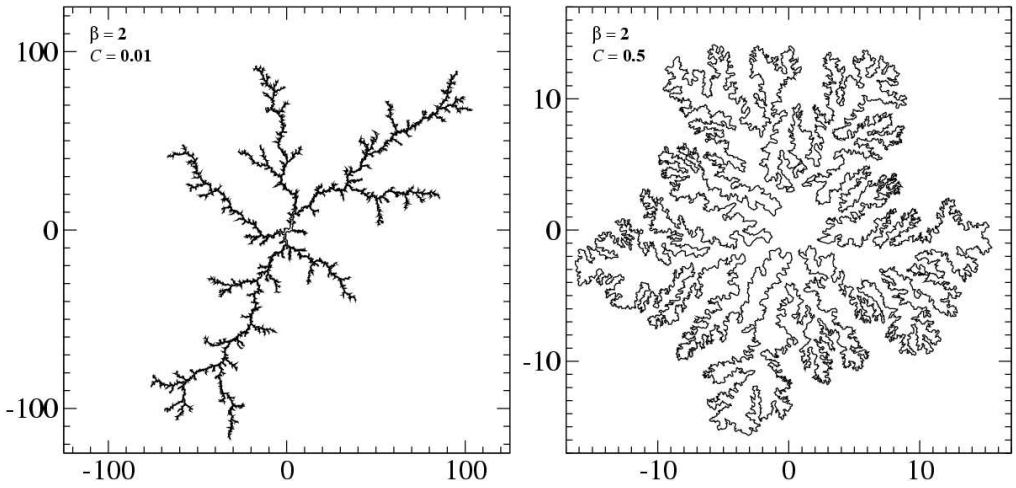

Figure 6: Clusters for $\beta = 2$: left: low coverage of $\mathcal{C} = 0.01$ results in less dense structures than DLA (left panel of figure 5). right: high coverage of $\mathcal{C} = 0.5$ results in a dense structure with a fractal dimension of at least D=1.75

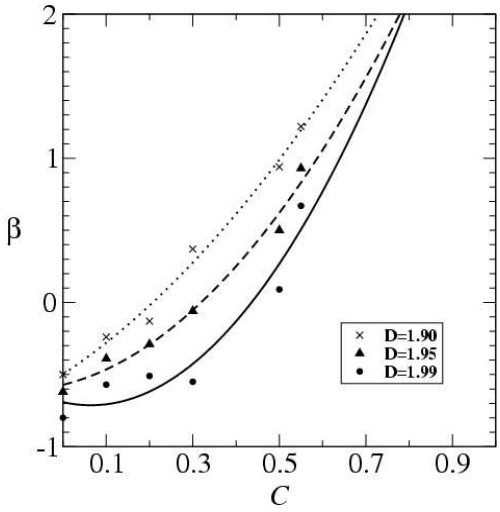

Figure 7: Phase diagram of the β-$\mathcal{C}$-model. The lines describe lower bounds for regions with fractal dimension equal or higher than $D = 1.90, 1.95$ and 1.99 from top to bottom. The extrapolation to $\mathcal{C} = 1$ shows that the model of parallel Laplacian growth ($\beta = 2, \mathcal{C} = 1$) clearly lies within the two-dimensional domain.

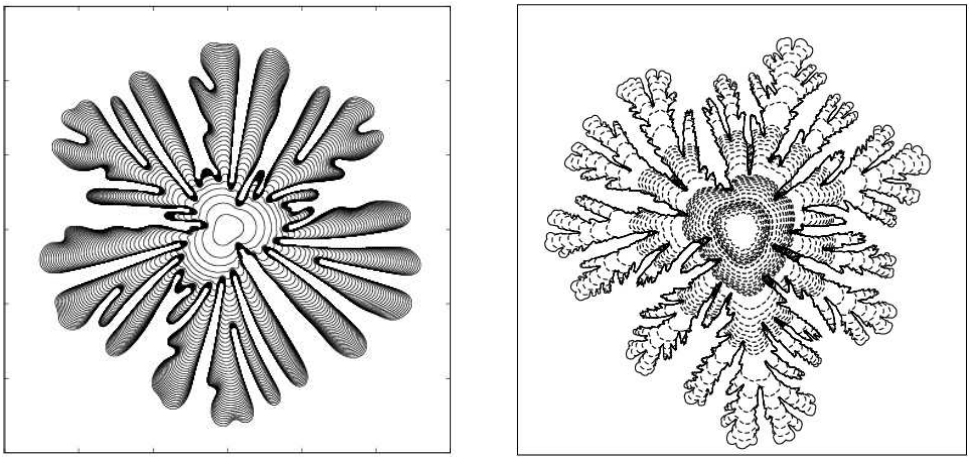

Figure 8: Left: computer simulation of a Hele-Shaw cell by Hou, Lowengrub and Shelley [17]. right: Cluster of the β-$\mathcal{C}$-model with full coverage $\mathcal{C} = 1$ obtained by locally approximating the harmonic measure during the growth process [76]. The value $\beta = 2$ corresponds to a linear particle size proportional to the local pressure gradient as in a Hele-Shaw cell.

The main differences between the β-$\mathcal{C}$-model and the continuous Laplacian growth are the bumpiness of the surface and the UV-regularization. The first can only result in an increased instability and should therefore only decrease the dimension of the β-$\mathcal{C}$-model compared to the Hele-Shaw flow. A similar argument holds with respect to the difference in UV-regularization. Any finite value of surface tension introduces a length-scale cut-off into the Hele-Shaw problem which is fixed for the duration of the flow. On the other hand does the length scale regularization in the β-$\mathcal{C}$-model decrease from layer to layer for any positive value of β [47]. This again should favor the development of smaller branches and decreased fractal dimension. We therefore conjecture that the Saffman-Taylor flow in a Hele-Shaw cell is two-dimensional and that the reason for this lies in the parallelity of the growth as opposed to a specific UV-regularization. The right panel of figure 8 shows a cluster with $\beta = 2$ and full coverage $\mathcal{C} = 1$. This is achieved by locally approximating the pressure field based on the conformal mapping technique and then growing deterministically a full layer [76]. The structure looks qualitatively identical to simulations of the Hele-Shaw problem [17] as shown in the left panel of figure 8. This similarity strengthens our conjecture that the presented model captures the main characteristics of the Hele-Shaw problem.

2.2 Quasi-static fracture propagation

The propagation of fractures in elastic solids is a complex problem. The microscopic physics of the evolution is not yet fully understood. However, despite this difficulty it is clear that the dynamics is driven by the stress field in the elastic material.

Thus, in order to quasi-statically[2] propagate a fracture, we need to compute the stress tensor σ around the fracture. We assume that all body forces in the material can be neglected in comparison to the intermolecular forces and the applied loadings. In terms of the stress field this means that inside the material it is

$$\sum_j \partial_j \sigma_{jk} = 0 \quad \forall k \tag{8}$$

Note that in particular we neglect here the inertial body forces. This excludes any dynamical effects such as sound evolution and makes our propagation quasi-static.

In linear elasticity theory (see for example [65-67]) the derivatives of the displacement vector **u** form the strain tensor

$$\epsilon_{jk} = \frac{1}{2} \left(\partial_j u_k + \partial_k u_j\right) \tag{9}$$

which is linearly related to the stress tensor

$$\sigma_{jk} = 2\mu \cdot \epsilon_{jk} + \delta_{jk} \cdot \lambda \cdot \sum_l \epsilon_{ll} \tag{10}$$

where λ and μ are Lamé's coefficients which depend on the material under consideration. These equations are supplemented by specific boundary conditions which follow from the loading applied to surfaces of the material.

[2]For a discussion on the validity of the quasi-static assumption in fracture propagation see appendix C.

2.2.1 Quasi-static fracture problems: modes I, II and III

We first consider the situation in which the fracture surface itself is free of any pressure or shear forces. This means that the stresses on the normal surface are zero. However the material may hold tensile tangential forces which may cause cracking. The external loading is applied at infinity, far away from the fracture and one distinguishes three kinds of configurations.

So called Mode III fracturing corresponds to an out-of-plane shear loading, for example in z-direction, $\lim_{y\to\infty} \sigma_{yz} = \sigma_\infty$. In this case there is no displacement of the material in x or y direction and the displacement in z direction is independent of z. Equations (8-10) then reduce to the Laplace equation for the displacement in z-direction $\nabla^2 u_z(x,y) = 0$ which is solved by the real part of a complex analytic function f. Given the conformal map from the outside of the unit circle to the outside of a structure Φ_n (compare section 2.1) this map is given by

$$f(w) = -i\,\frac{\sigma_\infty}{\mu}\,F_1^{(n)} \cdot \left(\Phi_n^{-1}(w) - \frac{1}{\Phi_n^{-1}(w)}\right) \tag{11}$$

where $w = x + iy$ and $F_1^{(n)}$ is the first Laurent coefficient of Φ_n (see section 4.1 for details). From this expression we can compute the stress tensor everywhere in the material. In order to quasi-statically propagate the fracture we choose the position of the next bump on the unit circle (compare section 2.1) with the probability density

$$\rho_{linear}(\theta) = \frac{\Delta\sigma(\theta)\cdot\Theta(\Delta\sigma(\theta))\cdot|\Phi_n'(e^{i\theta}))|}{\int d\theta \Delta\sigma(\theta)\cdot\Theta(\Delta\sigma(\theta))\cdot|\Phi_n'(e^{i\theta}))|} \tag{12}$$

where $\Delta\sigma(\theta) = |\sigma_{zt}(\theta)| - \sigma_c$ and σ_c is a material dependent threshold for the cracking. This law is used in the literature on fracture propagation [57], but it is not derived from first principle and still subject to active research. Since the patterns that result from the presented method depend on this propagation rule (see section 4.2), it may be used to check microscopic theories.

The left panel of figure 9 shows a fracture constructed with the linear propagation rule (12). In the right panel one can see the backbone of the pattern. The backbone shows a self-affine structure with an averaged roughness exponent ζ which crosses over from a value of $\zeta = 0.5 \pm 0.05$ for small distances to $\zeta = 0.75 \pm 0.02$ for larger distances (left panel of figure 10). However the higher exponent changes with the distance from the point of initiation of the crack, as can be seen in the right panel of figure 10. This behavior reflects the increasing ramification of the structure due to the increase in stress on the boundary as the surface area increases due to the cracking events.

In addition to different probability laws, we investigated the effect of quenched noise in the material (see section 4.2 for details). We observed that the roughness exponents were invariant over a large range of noise and for different distributions. Only extreme randomness in the material changes the geometry of the fractures qualitatively.

The other two modes of fracturing are inherently two-dimensional, i.e. only displacements in the plane of loading occur. Mode I results from a tensile stress as infinity, for example $\lim_{y\to\infty} \sigma_{yy} = \sigma_\infty$, while mode II corresponds to an in-plane shear stress $\lim_{y\to\infty} \sigma_{xy} = \sigma_\infty$. In these purely two-dimensional cases equations (8) are solved by the Airy-potential χ which fulfills the bi-Laplace equation

$$\nabla^2 \nabla^2 \chi = 0 \tag{13}$$

and is related to the stress tensor by

$$\sigma_{xx} = \partial_{yy}\chi, \qquad \sigma_{yy} = \partial_{xx}\chi, \qquad \sigma_{xy} = \sigma_{yx} = -\partial_{xy}\chi. \tag{14}$$

The general solution of the bi-Laplace equation in two dimensions is given by

$$\chi(w) = \Re\left(\overline{w} f(w) + \tilde{g}(w)\right) \tag{15}$$

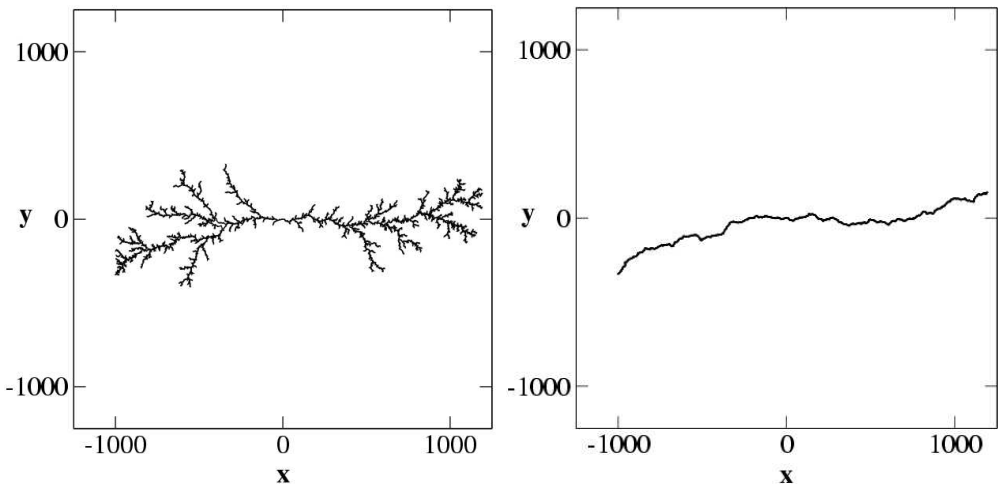

Figure 9: Left: mode III fracture obtained using the linear growth rule (12). The structure increasingly ramifies with the distance from the point of initiation in the origin. right: backbone of the fracture on the left.

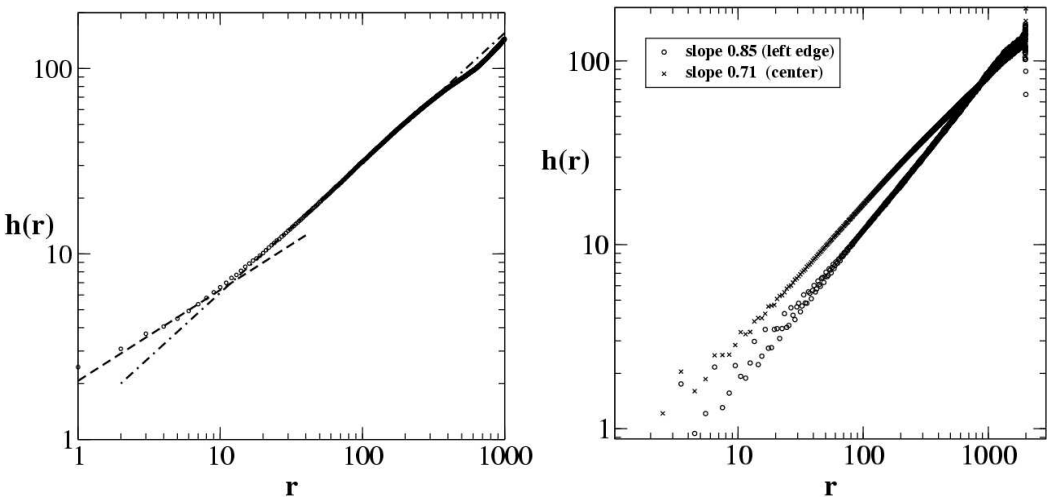

Figure 10: Left: averaged roughness of the backbone across the entire fracture. The maximal height $h(r)$ inside a window of size r scales with exponent $\zeta = 0.5 \pm 0.05$ for small scales and $\zeta = 0.75 \pm 0.02$ for large scales. right: roughness exponent for windows of size $r = 1000$ at the center of crack initiation (circles) and at the edge of the fracture (crosses). The roughness exponent increases with the distance from the origin, due to the increased ramification seen in figure 9. Thus the averaged exponent (left) does not reflect a time-independent property of the structure and care has to be taken in experiments.

where f and $\tilde{g}$ are complex analytic functions and $w = x + iy$. Thus in these cases we need to compute two functions in order to obtain the stress tensor everywhere in the material. Since the stress tensor can be expressed in terms of second derivatives of χ, we know that $f(w)$ and $g(w) \equiv \tilde{g}'(w)$ have to increase linearly at infinity. Thus the Laurent expansions of f and g start with the linear term and its coefficients are determined by the fracture mode and σ_∞ (see section 4.2 for details).

The remainder of the Laurent series of f and g are determined by the boundary conditions on the crack. After transformation onto the unit circle $\omega = e^{i\theta}$ through the map Φ_n, we get

$$f(\omega) + \frac{\Phi_n(\omega)}{\Phi_n'(\omega)} \overline{f'(\omega)} + \overline{g(\omega)} = 0 \qquad \text{for } \omega = e^{i\theta} \tag{16}$$

Note that in Fourier space the equations for f and g separate and both functions can be determined from equation (16).

After solving for the tangential tensile stress component σ_{tt} we propagate the fracture according to the probability density (12) where in this case $\Delta\sigma(\theta) = \sigma_{tt}(\theta) - \sigma_c$. The left panel of figure 11 shows a mode I fracture which was grown with the technique presented here. In contrast to the mode III case, only very little branching occurs and, as seen on the right in figure 11, the roughening is confined to small scales where it has the same exponent of $\zeta \approx 0.5$ as in mode III. This exponent might reflect the randomness in the technique rather than a physical process.

The result of no roughening at large scales is valid for any probability law that is monotonically increasing in $\Delta\sigma$ and carries over to the mode II case. Different from the mode III fracturing, the structures do not further ramify with increasing surface area. This can be understood from the distribution of the tangential tensile stress on the tip as shown in figure 12. In mode I the stress is much more concentrated onto the tip than in mode

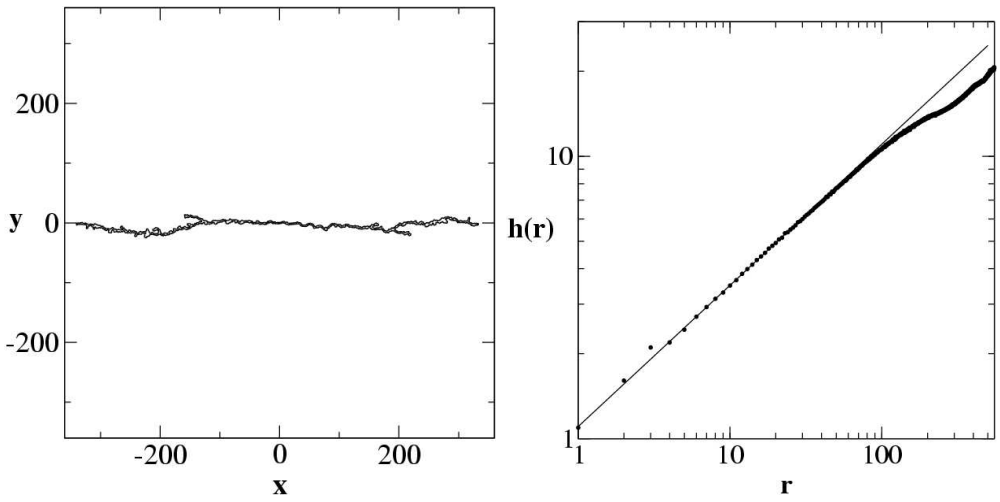

Figure 11: Left: mode I fracture with linear probability law. right: roughening is restricted to small scales and has the same exponent $\zeta \approx 0.5$ as for the small scales in mode III.

III. Furthermore random deviations from the symmetry line of the loading are counter-balanced by a stronger stress in direction toward this line. Thus for a monotonically increasing probability law the crack tends to stay close to the symmetry line. However, for probability densities which saturate for large $\Delta\sigma$, as for example

$$\rho_{saturation} \propto \frac{\Delta\sigma}{1+\Delta\sigma} \cdot \Theta\left(\Delta\sigma\right) \tag{17}$$

we observe increased branching. Figure 13 shows a fracture grown with the rule of equation (17). This dependence on the growth rule gives an indication that the presented method might help in checking microscopic theories for cracking [75].

2.2.2 Bi-Laplacian growth patterns

In analogy to the Laplacian growth patterns, the loading of an elastic media can also be given by a fluid that presses into a small hole in the center of the

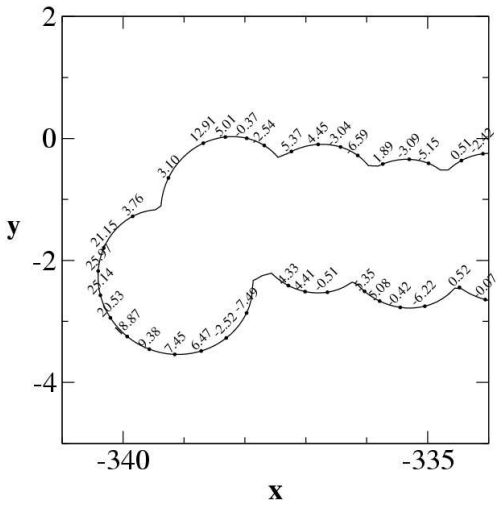

Figure 12: Distribution of the tangential tensile stress on the tip of a mode I fracture. Note the concentration on the tip and the tendency to correct for deviations from a straight line. Due to translational invariance in y-direction this does not happen in the mode III case which leads to branching of the structure in mode III but not in mode I.

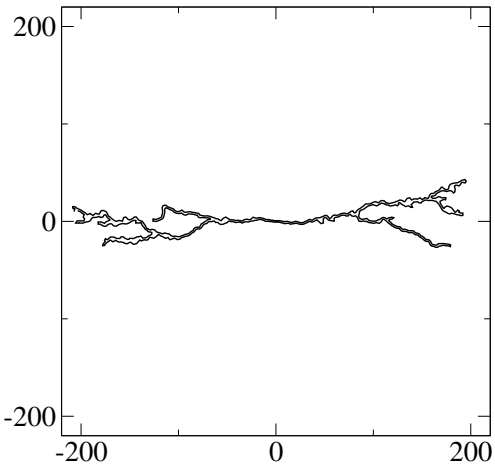

Figure 13: Mode I fracture with a saturating probability law (17). In contrast to the structure with a linear law (figure 11), in this case branching occurs. We propose to use these structural differences to verify microscopic theories for cracking.

material. In this case the solution for the stress tensor is still given by the Airy-function which fulfills the bi-Laplace equation. However the boundary conditions change. At infinity all stress components have to vanish since there is no loading there. On the fracture surface the normal stress component is given by the applied pressure p while the shear stresses are zero in the absence of fluid flow, i.e. in the quasi-static limit (compare for example [77, 78]).

With respect to the functions f and g the absence of any loading at infinity is reflected in the absence of the linear terms in their Laurent series. The boundary condition on the surface, equation (16), gets an additional term on the right-hand side

$$f(w) + \frac{\Phi_n(w)}{\Phi_n'(w)} \overline{f'(w)} + \overline{g(z)} = -p \cdot \Phi_n(w) \tag{18}$$

which reflects the loading with pressure p.

A typical structure that results from the solution for the stress field and a linear probability law as in equation (12) is shown in figure 14. Naturally the fractures are statistically isotropic as in Laplacian growth. However the bi-Laplacian growth shows much less ramification (compare with the DLA cluster in the left panel of figure 2). This is reflected in the scaling of the first Laurent coefficient $F_1^{(n)}$ of Φ_n which is a measure of the radius of the cluster (compare section 2.1). The left panel of figure 15 shows $F_1^{(n)}$ as a function of the number of fracture events n. The resulting dimension is $D = 1.4 \pm 0.1$. A further difference to Laplacian growth is the occurrence of large branching angles as can be observed in figure 14 in contrast to the DLA cluster in the right panel of figure 2.

The right panel of figure 15 shows the local tangential tensile stress component $\sigma_{tt}(n)$ at which the n^{th} fracture event took place. The values fluctuate according to the random choice of the position. However, they are bounded by the maximal stress on the tip of a linear fracture with the same loading

which is given by $\sigma_{tt,max}^{(line)} \approx p \cdot \sqrt{n}$ (dashed line).

The model of bi-Laplacian growth presented here serves as a limiting case for the displacement of visco-elastic media such as associated polymers, clays, foams etc. by a fluid, when the Deborah number of the process is sufficiently high, i.e. when elastic phenomena dominate the viscous effects (compare for example [79]).

Even though the viscous effects in most experiments [73, 74, 80] cannot be neglected, the influence of the elastic nature of the material can be observed in decreased ramification and an increase in the branching angles. These qualitative differences were previously pointed out for example in the experiments by Zhoa and Maher in [73] or the experiments by Lindner, Rica and Couder in [80] and can also be seen in figure 14.

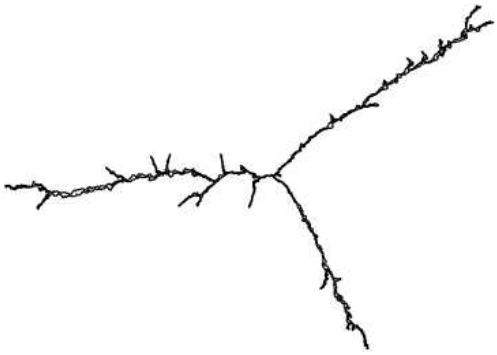

Figure 14: Bi-Laplacian growth pattern with $n = 7000$ fracture events.

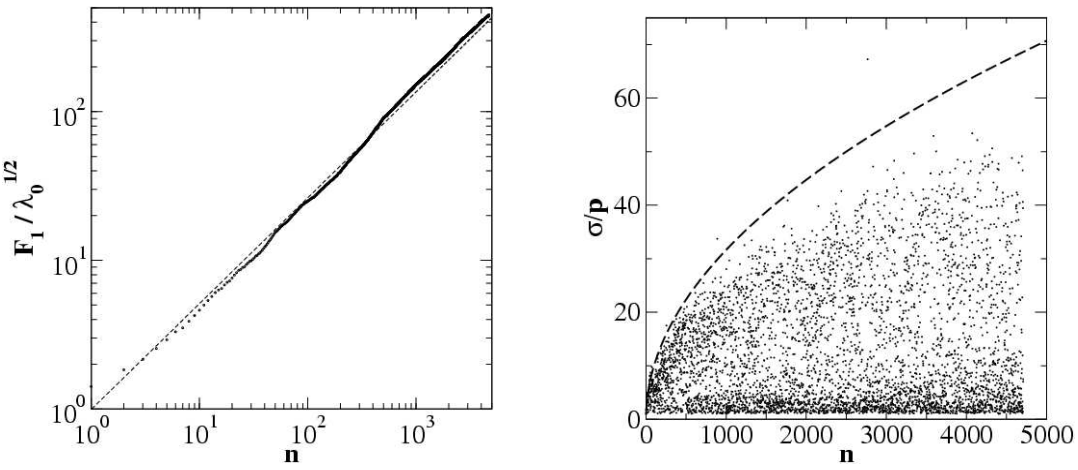

Figure 15: Left: scaling of the first Laurent coefficient $F_1^{(n)}$ of the map Φ_n, as a measure for the radius of the cluster in figure 14, gives a fractal dimension of $D = 1.4 \pm 0.1$. right: the tangential tensile stress component is bounded by its maximal value for a straight line crack $\sigma_{tt} \leq \sigma_{tt,max}^{(line)} \approx p \cdot \sqrt{n}$ (dashed line).

3 Laplacian growth processes

3.1 The multi-fractal spectrum of the harmonic measure of Diffusion Limited Aggregation

Physical Review Letters

Volume **87** (2001)

page 164101

VOLUME 87, NUMBER 16 PHYSICAL REVIEW LETTERS 15 OCTOBER 2001

Thermodynamic Formalism of the Harmonic Measure of Diffusion Limited Aggregates: Phase Transition

Benny Davidovitch,[1] Mogens H. Jensen,[2] Anders Levermann,[1] Joachim Mathiesen,[2] and Itamar Procaccia[1]
[1]*Department of Chemical Physics, The Weizmann Institute of Science, Rehovot 76100, Israel*
[2]*The Niels Bohr Institute, Blegdamsvej, Copenhagen, Denmark*
(Received 2 July 2001; published 2 October 2001)

We study the nature of the phase transition in the multifractal formalism of the harmonic measure of diffusion limited aggregates. Contrary to previous work that relied on random walk simulations or *ad hoc* models to estimate the low probability events of deep fjord penetration, we employ the method of iterated conformal maps to obtain an accurate computation of the probability of the rarest events. We resolve probabilities as small as 10^{-35}. We show that the generalized dimensions D_q are infinite for $q < q^*$, where $q^* = -0.18 \pm 0.04$. In the language of $f(\alpha)$ this means that $\alpha_{\max}$ is finite. We present a converged $f(\alpha)$ curve.

DOI: 10.1103/PhysRevLett.87.164101 PACS numbers: 47.27.Gs, 05.40.–a, 47.27.Jv

Since its introduction in 1981 [1] the model of diffusion limited aggregation (DLA) has posed a challenge to our understanding of fractal and multifractal phenomena. DLA is a paradigmatic example for the spontaneous generation of fractal objects by simple dynamical rules (being generated by random walkers); its harmonic measure, which is the probability for a random walker to hit the surface, had been one of the first studied examples of multifractal measures outside the realm of ergodic measures in dynamical systems [2]. The multifractal properties stem from the extreme contrast between the probability to hit the tips of the DLA compared with penetrating the fjords.

The multifractal properties of the harmonic measure of the DLA are conveniently studied in the context of the generalized dimensions D_q and the associated $f(\alpha)$ function [3,4]. The simplest definition of the generalized dimensions is in terms of a uniform covering of the boundary of a DLA cluster with boxes of size ℓ and measuring the probability for a random walker coming from infinity to hit a piece of boundary which belongs to the ith box. Denoting this probability by $P_i(\ell)$, one considers [3]

$$D_q \equiv \lim_{\ell \to 0} \frac{1}{q-1} \frac{\log \sum_i P_i^q(\ell)}{\log \ell}. \quad (1)$$

It is well known by now that the existence of an interesting spectrum of values D_q is related to the probabilities $P_i(\ell)$ having a spectrum of "singularities" in the sense that $P_i(\ell) \sim \ell^\alpha$ with α taking on values from a range $\alpha_{\min} \le \alpha \le \alpha_{\max}$. The frequency of observation of a particular value of α is determined by the function $f(\alpha)$ where [with $\tau(q) \equiv (q-1)D_q$]

$$f(\alpha) = \alpha q(\alpha) - \tau(q(\alpha)), \qquad \frac{\partial \tau(q)}{\partial q} = \alpha(q). \quad (2)$$

The understanding of the multifractal properties and the associated $f(\alpha)$ spectrum of DLA clusters have been a long-standing issue. Of particular interest are the values of the minimal and maximal values, $\alpha_{\min}$ and $\alpha_{\max}$, relating to the largest and smallest growth probabilities, respectively. As a DLA cluster grows the large branches screen the deep fjords more and more and the probability for a random walker to get into these fjords (say around the seed of the cluster) becomes smaller and smaller. A small growth probability corresponds to a large value of α. Previous literature hardly agrees about the actual value of $\alpha_{\max}$. Ensemble averages of the harmonic measure of DLA clusters indicated a rather large value of $\alpha_{\max} \sim 8$ [5]. In subsequent experiments on non-Newtonian fluids [6] and on viscous fingers [7], similar large values of $\alpha_{\max}$ were also observed. These numerical and experimental indications of a very large value of $\alpha_{\max}$ led to a conjecture that, in the limit of a large, self-similar cluster some fjords will be exponentially screened and thus causing $\alpha_{\max} \to \infty$ [8].

If indeed $\alpha_{\max} \to \infty$, this can be interpreted as a phase transition [9] (nonanalyticity) in the q dependence of D_q, at a value of q satisfying $q \ge 0$. If the transition takes place for a value $q < 0$, then $\alpha_{\max}$ is finite. Lee and Stanley [10] proposed that $\alpha_{\max}$ diverges like $R^2/\ln R$ with R being the radius of the cluster. Schwarzer *et al.* [11] proposed that $\alpha_{\max}$ diverges only logarithmically in the number of added particles. Blumenfeld and Aharony [12] proposed that channel-shaped fjords are important and proposed that $\alpha_{\max} \sim \frac{M^x}{\ln M}$, where M is the mass of the cluster; Harris and Cohen [13], on the other hand, argued that straight channels might be so rare that they do not make a noticeable contribution, and $\alpha_{\max}$ is finite, in agreement with Ball and Blumenfeld who proposed [14] that $\alpha_{\max}$ is bounded. Obviously, the issue was not quite settled. The difficulty is that it is very hard to estimate the smallest growth probabilities using models or direct numerical simulations.

In this Letter we use the method of iterated conformal maps to offer an accurate determination of the probability for the rarest events. We propose that using this method we can settle the issue in a conclusive way. Our result is that $\alpha_{\max}$ exists and the phase transition occurs at a q

 © 2001 The American Physical Society

VOLUME 87, NUMBER 16 PHYSICAL REVIEW LETTERS 15 OCTOBER 2001

value that is slightly negative. In this method one studies DLA by constructing $\Phi^{(n)}(w)$ which conformally maps the exterior of the unit circle $e^{i\theta}$ in the mathematical w plane onto the complement of the (simply connected) cluster of n particles in the physical z plane [15–17]. The unit circle is mapped onto the boundary of the cluster. The map $\Phi^{(n)}(w)$ is made from compositions of elementary maps $\phi_{\lambda,\theta}$,

$$\Phi^{(n)}(w) = \Phi^{(n-1)}[\phi_{\lambda_n,\theta_n}(w)], \tag{3}$$

where the elementary map $\phi_{\lambda,\theta}$ transforms the unit circle to a circle with a semicircular "bump" of linear size $\sqrt{\lambda}$ around the point $w = e^{i\theta}$. We use below the same map $\phi_{\lambda,\theta}$ that was employed in [15–19]. With this map $\Phi^{(n)}(w)$ adds on a semicircular new bump to the image of the unit circle under $\Phi^{(n-1)}(w)$. The bumps in the z plane simulate the accreted particles in the physical space formulation of the growth process. Since we want to have *fixed size* bumps in the physical space, say of fixed area λ_0, we choose in the nth step

$$\lambda_n = \frac{\lambda_0}{|\Phi^{(n-1)\prime}(e^{i\theta_n})|^2}. \tag{4}$$

The recursive dynamics can be represented as iterations of the map $\phi_{\lambda_n,\theta_n}(w)$,

$$\Phi^{(n)}(w) = \phi_{\lambda_1,\theta_1} \circ \phi_{\lambda_2,\theta_2} \circ \cdots \circ \phi_{\lambda_n,\theta_n}(\omega). \tag{5}$$

It had been demonstrated before that this method represents DLA accurately, providing many analytic insights that are not available otherwise [18,19]. For our purposes here we quote a result established in [16], which is

$$\langle \lambda_n^q \rangle \equiv (1/2\pi) \int_0^{2\pi} \lambda_n^q(\theta)\, d\theta \sim n^{-2qD_{2q+1}/D}. \tag{6}$$

To compute $\tau(q)$ we rewrite this average as

$$\langle \lambda_n^q \rangle = \int ds \left| \frac{d\theta}{ds} \right| \lambda_n^q(s) = \int ds\, \frac{\lambda^{q+1/2}(s)}{\sqrt{\lambda_0}}, \tag{7}$$

where s is the arclength of the physical boundary of the cluster. In the last equality we used the fact that $|d\theta/ds| = \sqrt{\lambda_n/\lambda_0}$. We stress at this point that in order to measure these moments for $q \leq 0$ we *must* go into arclength representation.

To make this crucial point clear we discuss briefly what happens if one attempts to compute the moments from the definition (6). Having at hand the conformal map $\Phi^{(n)}(e^{i\theta})$, one can choose randomly as many points on the unit circle $[0, 2\pi]$ as one wishes, obtain as many (accurate) values of λ_n, and try to compute the integral as a finite sum. The problem is of course that using such an approach *the fjords are not resolved*. To see this we show in Fig. 1(a) the region of a typical cluster of 50 000 particles that is being visited by a random search on the unit circle. As in direct simulations using random walks, the rarest events are not probed, and no serious conclusion regarding the phase transition is possible.

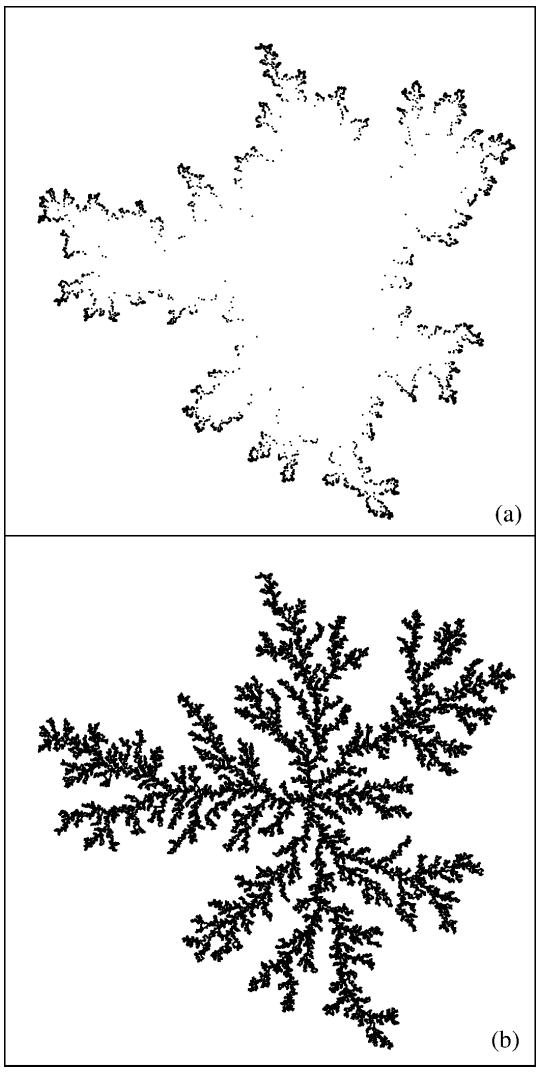

FIG. 1. (a) The boundary of the cluster probed by a random search with respect to the harmonic measure. (b) The boundary of the cluster probed by the present method.

Another method that cannot work is to try to compute by sampling on the arclength in a naive way. The reason is that the inverse map $[\Phi^{(n)}]^{-1}(s)$ cannot resolve θ values that belong to deep fjords. As the growth proceeds, reparametrization squeezes the θ values that map to fjords into minute intervals, below the computer numerical resolution. To compute the values of $\lambda_n(s)$ effectively we must use the full power of our iterated conformal dynamics, carrying the history with us, to iterate forward and backward at will to resolve accurately the θ, λ values of any given particle on the fully grown cluster.

To do this we recognize that every time we grow a semicircular bump we generate two new branch cuts in the map $\Phi^{(n)}$. We find the position on the boundary between every two branch cuts and there compute the value of λ_n. The first step in our algorithm is to generate the location of these points intermediate to the branch cuts [20]. Each

branch cut has a preimage on the unit circle which will be indexed with three indices, $w_{j,\ell}^{k(\ell)} \equiv \exp[i\theta_{j,\ell}^{k(\ell)}]$. The index j represents the generation when the branch cut was created (i.e., when the jth particle was grown). The index ℓ stands for the generation at which the analysis is being done (i.e., when the cluster has ℓ particles). The index k represents the position of the branch cut along the arclength, and it is a function of the generation ℓ. Note that since bumps may overlap during growth, branch cuts are then covered, and therefore the maximal k, $k_{\max} \leq 2\ell$. After each iteration the preimage of each branch cut moves on the unit circle, but its physical position remains. This leads to the equation that relates the indices of a still exposed branch cut that was created at generation j to a later generation n:

$$\Phi^{(n)}(w_{j,n}^{k(n)}) \equiv \Phi^{(n)}[\phi_{\lambda_n,\theta_n}^{-1} \circ \cdots \circ \phi_{\lambda_{j+1},\theta_{j+1}}^{-1}(w_{j,j}^{\tilde{k}(j)})] = \Phi^{(j)}(w_{j,j}^{\tilde{k}(j)}). \quad (8)$$

Note that the sorting indices $\tilde{k}(j)$ are not simply related to $k(n)$ and need to be tracked as follows. Suppose that the list $w_{j,n-1}^{k(n-1)}$ is available. In the nth generation we choose randomly a new θ_n and find two new branch cuts which on the unit circle are at angles $\theta_n^{\pm}$. If one (or very rarely more) branch cut of the updated list $\phi_{\lambda_n,\theta_n}^{-1}(w_{j,n-1}^{k(n-1)})$ is covered, it is eliminated from the list, and together with the sorted new pair we make the list $w_{j,n}^{k(n)}$. Having a cluster of n particles we now consider all neighboring pairs of preimages $w_{j,n}^{k(n)}$ and $w_{J,n}^{k(n)+1}$, that very well may have been created at two different generations j and J. The larger of these indices (J without loss of generality) determines the generation of the intermediate position at which we want to compute the field. We want to find the preimage $u_{J,J}^{k(n)}$ of this midpoint on the unit circle to compute $\lambda_{k(n)}$ there accurately. Using definition (8) we find the preimage

$$\arg(u_{J,J}^{k(n)}) = [\arg(w_{j,J}^{\tilde{k}(J)}) + \arg(w_{J,J}^{\tilde{k}(J)+1})]/2. \quad (9)$$

In Fig. 1(b) we show, for the same cluster of 50 000, the map $\Phi^{(J)}(u_{J,J}^{k(n)})$ with $k(n)$ running between 1 and $k_{\max}$, with J being the corresponding generation of creation of the midpoint. We see that now all the particles are probed, and every single value of $\lambda_{k(n)}$ can be computed. However, to compute these $\lambda_{k(n)}$ accurately, we define [in analogy to Eq. (8)] for every $J < m \leq n$,

$$u_{J,m}^{k(n)} \equiv \phi_{\lambda_m,\theta_m}^{-1} \circ \cdots \circ \phi_{\lambda_{J+1},\theta_{J+1}}^{-1}(u_{J,J}^{k(n)}). \quad (10)$$

Finally $\lambda_{k(n)}$ is computed from the definition (4) with

$$\Phi^{(n)\prime}(u_{J,n}^{k(n)}) = \phi'_{\lambda_n,\theta_n}(u_{J,n}^{k(n)}) \cdots \phi'_{\lambda_{J+1},\theta_{J+1}}(u_{J,J+1}^{k(n)}) \times \Phi^{(J)\prime}(u_{J,J}^{k(n)}). \quad (11)$$

This calculation is optimally accurate since we avoid as much as possible the effects of the rapid shrinking of low probability regions on the unit circle. Each derivative in (11) is computed using information from a generation in which points on the unit circle are optimally resolved.

The integral (7) is then estimated as the finite sum $\sqrt{\lambda_0}\sum_{k(n)} \lambda_{k(n)}^q$. We should stress that for clusters of the order of 30 000 particles we already compute, using this algorithm, $\lambda_{k(n)}$ values of the order of 10^{-70}. To find the equivalent small probabilities using random walks would require about 10^{35} attempts to see them just once. This is of course impossible, explaining the lasting confusion about the issue of the phase transition in this problem. This also means that all the $f(\alpha)$ curves that were computed before [5,21] did not converge. Note that in our calculation the small values of $\lambda_{k(n)}$ are obtained from multiplications rather than additions and therefore can be trusted.

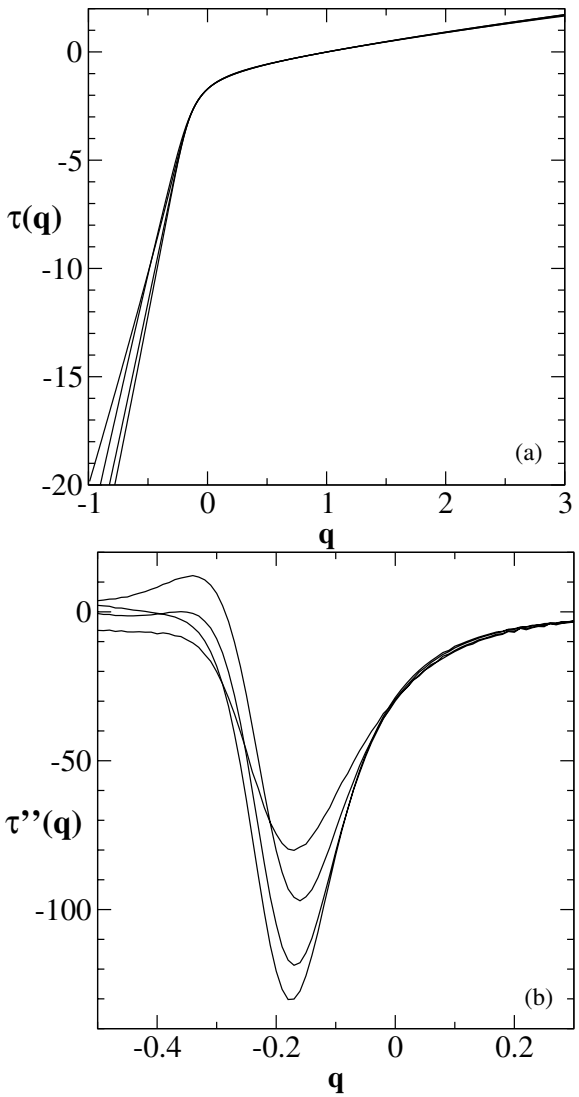

FIG. 2. (a) The calculated function $\tau(q)$ for clusters of n particles, with $n = 10\,000$, 15 000, 25 000, and 30 000. (b) The second derivative of $\tau(q)$ with respect to q.

VOLUME 87, NUMBER 16 PHYSICAL REVIEW LETTERS 15 OCTOBER 2001

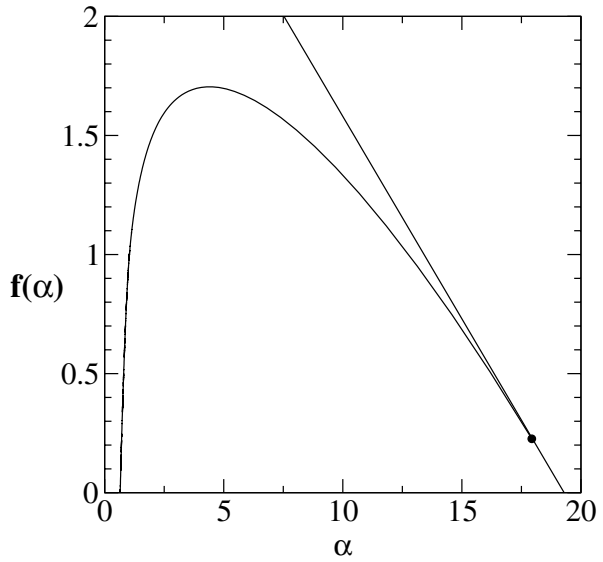

FIG. 3. The calculated function $f(\alpha)$ using $\tau(q)$ calculated from a cluster with $n = 30\,000$ particles. This $f(\alpha)$ is almost indistinguishable from the one computed with $n = 25\,000$ particles. We propose that this function is well converged. The black dot denotes where the curve ends, being tangent to the line with slope -0.18.

Having the accurate values $\lambda_{k(n)}$ we can now compute the moments (6). Since the scaling form on the right-hand side includes unknown coefficients, we compute the values of $\tau(q)$ by dividing $\langle\lambda_n^q\rangle$ by $\langle\lambda_{\bar{n}}^q\rangle$, estimating

$$\tau(q) \approx -D\,\frac{\log\langle\lambda_n^q\rangle - \log\langle\lambda_{\bar{n}}^q\rangle}{\log n - \log\bar{n}}. \qquad (12)$$

Results for $\tau(q)$ for increasing values of n and $\bar{n}$ are shown in Fig. 2(a). It is seen that the value of $\tau(q)$ appears to grow without bound for q negative. The existence of a phase transition is, however, best indicated by measuring the derivatives of $\tau(q)$ with respect to q. In Fig. 2(b) we show the second derivative, indicating a phase transition at a value of q that recedes *away* from $q = 0$ when n increases. Because of the great accuracy of our measurement of λ we can estimate already with clusters as small as 20–30 000 the q value of the phase transition to $q = -0.18 \pm 0.04$. The fact that this value is very close to the converged value can be seen from the $f(\alpha)$ curve which is plotted in Fig. 3. A test of convergence is that the slope of this function where it becomes essentially linear must agree with the q value of the phase transition. The straight line shown in Fig. 3 has the slope of -0.18, and it indeed approximates very accurately the slope of the $f(\alpha)$ curve where it ends and stops being analytic. The reader should also note that the peak of the curve agrees with $D \approx 1.71$, as well as the fact that $\tau(3)$ is also D as expected in this problem. The value of $\alpha_{\max}$ is close to 20, which is higher than anything predicted before. It is nevertheless finite. We believe that this function is well converged, in contradistinction with past calculations.

This work has been supported in part by the Petroleum Research Fund, The European Commission under the TMR program, and the Naftali and Anna Backenroth-Bronicki Fund for Research in Chaos and Complexity.

[1] T. A. Witten and L. Sander, Phys. Rev. Lett. **47**, 1400 (1981).
[2] T. C. Halsey, P. Meakin, and I. Procaccia, Phys. Rev. Lett. **56**, 854 (1986).
[3] H. G. E. Hentschel and I. Procaccia, Physica (Amsterdam) **8D**, 435 (1983).
[4] T. C. Halsey, M. H. Jensen, L. P. Kadanoff, I. Procaccia, and B. Shraiman, Phys. Rev. A **33**, 1141 (1986).
[5] C. Amitrano, A. Coniglio, and F. di Liberto, Phys. Rev. Lett. **57**, 1098 (1986).
[6] J. Nittmann, H. E. Stanley, E. Touboul, and G. Daccord, Phys. Rev. Lett. **58**, 619 (1987).
[7] K. J. Måløy, F. Boger, J. Feder, and T. Jøssang, in *Time-Dependent Effects in Disordered Materials,* edited by R. Pynn and T. Riste (Plenum, New York, 1987), p. 111.
[8] T. Bohr, P. Cvitanović, and M. H. Jensen, Europhys. Lett. **6**, 445 (1988).
[9] P. Cvitanović, in *Proceedings of the XIV Colloquium on Group Theoretical Methods in Physics,* edited by R. Gilmore (World Scientific, Singapore, 1987); in *Non-Linear Evolution and Chaotic Phenomena,* edited by P. Zweifel, G. Gallavotti, and M. Anile (Plenum, New York, 1988).
[10] J. Lee and H. E. Stanley, Phys. Rev. Lett. **61**, 2945 (1988).
[11] S. Schwarzer, J. Lee, A. Bunde, S. Havlin, H. E. Roman, and H. E. Stanley, Phys. Rev. Lett. **65**, 603 (1990).
[12] R. Blumenfeld and A. Aharony, Phys. Rev. Lett. **62**, 2977 (1989).
[13] A. B. Harris and M. Cohen, Phys. Rev. A **41**, 971 (1990).
[14] R. C. Ball and R. Blumenfeld, Phys. Rev. A **44**, R828 (1991).
[15] M. B. Hastings and L. S. Levitov, Physica (Amsterdam) **116D**, 244 (1998).
[16] B. Davidovitch, H. G. E. Hentschel, Z. Olami, I. Procaccia, L. M. Sander, and E. Somfai, Phys. Rev. E **59**, 1368 (1999).
[17] B. Davidovitch, M. J. Feigenbaum, H. G. E. Hentschel, and I. Procaccia, Phys. Rev. E **62**, 1706 (2000).
[18] B. Davidovitch and I. Procaccia, Phys. Rev. Lett. **85**, 3608 (2000).
[19] B. Davidovitch, A. Levermann, and I. Procaccia, Phys. Rev. E **62**, R5919 (2000).
[20] F. Barra, B. Davidovitch, and I. Procaccia, cond-mat/0105608.
[21] Y. Hayakawa, S. Sato, and M. Matushita, Phys. Rev. A **36**, 1963 (1987).

3.2 The phase transition in the multi-fractal spectrum of the harmonic measure of Diffusion Limited Aggregation

Physical Review E

Volume **65** (2002)

page 046109

PHYSICAL REVIEW E, VOLUME 65, 046109

Multifractal structure of the harmonic measure of diffusion-limited aggregates

Mogens H. Jensen,[1] Anders Levermann,[2] Joachim Mathiesen,[1] and Itamar Procaccia[2]
[1]*The Niels Bohr Institute, 17 Blegdamsvej, Copenhagen, Denmark*
[2]*Department of Chemical Physics, The Weizmann Institute of Science, Rehovot 76100, Israel*
(Received 10 October 2001; published 25 March 2002)

The method of iterated conformal maps allows one to study the harmonic measure of diffusion-limited aggregates with unprecedented accuracy. We employ this method to explore the multifractal properties of the measure, including the scaling of the measure in the deepest fjords that were hitherto screened away from any numerical probing. We resolve probabilities as small as 10^{-35}, and present an accurate determination of the generalized dimensions and the spectrum of singularities. We show that the generalized dimensions D_q are infinite for $q<q^*$, where q^* is of the order of -0.2. In the language of $f(\alpha)$ this means that α_{max} is finite. The $f(\alpha)$ curve loses analyticity (the phenomenon of "phase transition") at α_{max} and a finite value of $f(\alpha_{max})$. We consider the geometric structure of the regions that support the lowest parts of the harmonic measure, and thus offer an explanation for the phase transition, rationalizing the value of q^* and $f(\alpha_{max})$. We thus offer a satisfactory physical picture of the scaling properties of this multifractal measure.

DOI: 10.1103/PhysRevE.65.046109 PACS number(s): 02.50.−r, 05.40.−a, 47.27.Gs, 47.27.Jv

I. INTRODUCTION

Multifractal measures are normalized distributions lying upon fractal sets. Such measures appear naturally in a variety of nonlinear physics context, the most well studied being natural measures of chaotic dynamical systems [1–3]. Other well-studied examples are the voltage distribution of random resistor networks [4,5]. In this paper, we address the harmonic measure of diffusion-limited aggregates (DLA) [6], which is the probability measure for a random walker coming from infinity to hit the boundary of the fractal cluster. This was one of the earliest multifractal measures to be studied in the physics literature [7], but the elucidation of its properties was made difficult by the extreme variation of the probability to hit the tips of a DLA versus hitting the deep fjords. With usual numerical techniques it is quite impossible to estimate accurately the extremely small probabilities to penetrate the fjords. Contrary to harmonic measures of conformally invariant fractals such as random walks and percolation clusters whose multifractal properties can be solved exactly [8,9], the present multifractal measure posed stubborn barriers to mathematical progress.

The multifractal properties of fractal measures in general, and of the harmonic measure of DLA, in particular, are conveniently studied in the context of the generalized dimensions D_q, and the associated $f(\alpha)$ function [10,11]. The simplest definition of the generalized dimensions is in terms of a uniform covering of the boundary of a DLA cluster with boxes of size ℓ, and measuring the probability for a random walker coming from infinity to hit a piece of boundary that belongs to the i'th box. Denoting this probability by $P_i(\ell)$, one considers [10]

$$D_q \equiv \lim_{\ell \to 0} \frac{1}{q-1} \frac{\ln \sum_i P_i^q(\ell)}{\ln \ell}, \tag{1}$$

where the index i runs over all the boxes that contain a piece of the boundary. The limit $D_0 \equiv \lim_{q \to 0^+} D_q$ is the fractal, or box dimension of the cluster. $D_1 \equiv \lim_{q \to 1^+} D_q$ and D_2 are the well-known information and correlation dimensions, respectively [2,12,13]. It is well established by now [11] that the existence of an interesting spectrum of values D_q is related to the probabilities $P_i(\ell)$ having a spectrum of "singularities" in the sense that $P_i(\ell) \sim \ell^\alpha$ with α taking on values from a range $\alpha_{\min} \leqslant \alpha \leqslant \alpha_{\max}$. The frequency of observation of a particular value of α is determined by the function $f(\alpha)$, where [with $\tau(q) \equiv (q-1)D_q$]

$$f(\alpha) = \alpha q(\alpha) - \tau[q(\alpha)], \quad \frac{\partial \tau(q)}{\partial q} = \alpha(q). \tag{2}$$

The understanding of the multifractal properties and the associated $f(\alpha)$ spectrum of DLA clusters have been a long standing issue. Of particular interest are the minimal and maximal values α_{min} and α_{max} relating to the largest and smallest growth probabilities, respectively.

The minimal value of α is relatively easy to estimate, since it is related to the scaling of the harmonic measure near the most probable tip. While the often cited Turkevich-Scher conjecture [14] that α_{min} satisfies the scaling relation $D_0 = 1 + \alpha_{min}$ is probably not exact, it comes rather close to the mark. On the other hand, the maximal value of α is a much more subtle issue. As a DLA cluster grows the large branches screen the deep fjords more and more and the probability for a random walker to get into these fjords (say around the seed of the cluster) becomes smaller and smaller. A small growth probability corresponds to a large value of α. Previous literature hardly agrees about the actual value of α_{max}. Ensemble averages of the harmonic measure of DLA clusters indicated a rather large value of $\alpha_{max} \sim 8$ [15]. In subsequent experiments on non-Newtonian fluids [16] and on viscous fingers [17], similar large values of α_{max} were also observed. These numerical and experimental indications of a very large value of α_{max} led to a conjecture that, in the limit of a large, self-similar cluster some fjords will be exponentially screened and thus causing $\alpha_{max} \to \infty$ [18].

 ©2002 The American Physical Society

If indeed $\alpha_{max}\to\infty$, this can be interpreted as a phase transition [19] (nonanalyticity) in the q dependence of D_q, at a value of q^* satisfying $q^*\geqslant 0$. If the transition takes place for a value $q^*<0$ then α_{max} is finite. Lee and Stanley [20] proposed that α_{max} diverges as $R^2/\ln R$ with R being the radius of the cluster. Schwarzer *et al.* [21] proposed that α_{max} diverges only logarithmically in the number of added particles. Blumenfeld and Aharony [22] proposed that channel-shaped fjords are important and proposed that $\alpha_{max}\sim M^x/\ln M$, where M is the mass of the cluster; Harris and Cohen [23], on the other hand, argued that straight channels might be so rare that they do not make a noticeable contribution, and α_{max} is finite, in agreement with Ball and Blumenfeld who proposed [24] that α_{max} is bounded. Obviously, the issue was not quite settled. The difficulty is that it is very hard to estimate the smallest growth probabilities using models or direct numerical simulations.

In a recent paper [25], we used the method of iterated conformal maps to offer an accurate determination of the probability for the rarest events. The main result that was announced was that α_{max} exists and the phase transition occurs at a q value that is slightly negative. In the present paper, we discuss the results in greater detail, and offer additional insights to the geometric interpretation of the phase transition. In Sec. II, we summarize briefly the method of iterated conformal maps and explain how it is employed to compute the harmonic measure of DLA with unprecedented accuracy. In Sec. III, we perform the multifractal analysis and present the calculation of the $f(\alpha)$ curve. In Sec. IV, we discuss a complementary point of view of the scaling properties of the rarest regions of the measure, to achieve in Sec. V a geometric interpretation of the phase transition. Section VI offers a short discussion.

II. ACCURATE CALCULATION OF THE HARMONIC MEASURE

A. DLA via iterated conformal maps

Consider a DLA of n particles and denote the boundary of the cluster by $z(s)$, where s is an arc-length parametrization. Invoke now a conformal map $\Phi^{(n)}(\omega)$ that maps the exterior of the unit circle in the mathematical plane ω onto the complement of the cluster of n particle in the z plane. On the unit circle $e^{i\theta}$ the harmonic measure is uniform, $P(\theta)d\theta = d\theta/2\pi$. The harmonic measure of an element ds on the cluster in the physical space is then determined as

$$P(s)ds\sim\frac{ds}{|\Phi'^{(n)}(e^{i\theta})|}, \tag{3}$$

where $\Phi^{(n)}(e^{i\theta})=z(s)$. Note that in electrostatic parlance $1/|\Phi'^{(n)}(\omega)|$ is the electric field at the position $z=\Phi^{(n)}(\omega)$. Thus, in principle, if we can have an accurate value of the conformal map $\Phi^{(n)}(\omega)$ for all values $\omega=e^{i\theta}$ we can compute the harmonic measure with desired precision. We will see that this is easier said than done, but nevertheless this is the basic principle of our approach.

We thus need to find the conformal map $\Phi^{(n)}(\omega)$. A method for this purpose was developed in a recent series of papers [26–28]. The map $\Phi^{(n)}(w)$ is made from compositions of elementary maps $\phi_{\lambda,\theta}$,

$$\Phi^{(n)}(w)=\Phi^{(n-1)}(\phi_{\lambda_n,\theta_n}(w)), \tag{4}$$

where the elementary map $\phi_{\lambda,\theta}$ transforms the unit circle to a circle with a semicircular "bump" of linear size $\sqrt{\lambda}$ around the point $w=e^{i\theta}$. We use below the same map $\phi_{\lambda,\theta}$ that was employed in Refs. [26–30]. With this map $\Phi^{(n)}(w)$ adds on a semicircular new bump to the image of the unit circle under $\Phi^{(n-1)}(w)$. The bumps in the z plane simulate the accreted particles in the physical space formulation of the growth process. Since we want to have *fixed size* bumps in the physical space, say of fixed area λ_0, we choose in the nth step

$$\lambda_n=\frac{\lambda_0}{|\Phi^{(n-1)'}(e^{i\theta_n})|^2}. \tag{5}$$

The recursive dynamics can be represented as iterations of the map $\phi_{\lambda_n,\theta_n}(w)$,

$$\Phi^{(n)}(w)=\phi_{\lambda_1,\theta_1}\circ\phi_{\lambda_2,\theta_2}\circ\ldots\circ\phi_{\lambda_n,\theta_n}(\omega). \tag{6}$$

It had been demonstrated before that this method represents DLA accurately, providing many analytic insights that are not available otherwise [29,30].

B. Computing the harmonic measure

In terms of computing the harmonic measure we note the close relationship between Eqs. (3) and (5). Clearly, moments of the harmonic measure can be computed from moments of λ_n. For our purpose here we quote a result established in Ref. [27], which is

$$\langle\lambda_n^q\rangle\equiv(1/2\pi)\int_0^{2\pi}\lambda_n^q(\theta)d\theta\sim n^{-2qD_{2q+1}/D}. \tag{7}$$

To compute $\tau(q)$ we rewrite this average as

$$\langle\lambda_n^q\rangle=\int ds\left|\frac{d\theta}{ds}\right|\lambda_n^q(s)=\int ds\,\frac{\lambda^{q+1/2}(s)}{\sqrt{\lambda_0}}, \tag{8}$$

where s is the arc length of the physical boundary of the cluster. In the last equality we used the fact that $|d\theta/ds| = \sqrt{\lambda_n/\lambda_0}$. We stress at this point that in order to measure these moments for $q\leqslant 0$ we *must* go into arc-length representation.

To make this crucial point clear we discuss briefly what happens if one attempts to compute the moments from the definition (7). Having at hand the conformal map $\Phi^{(n)}(e^{i\theta})$, one can choose randomly as many points on the unit circle $[0,2\pi]$ as one wishes, obtain as many (accurate) values of λ_n, and try to compute the integral as a finite sum. The problem is of course that using such an approach *the fjords are not resolved*. To see this we show in Fig. 1, left panel, the

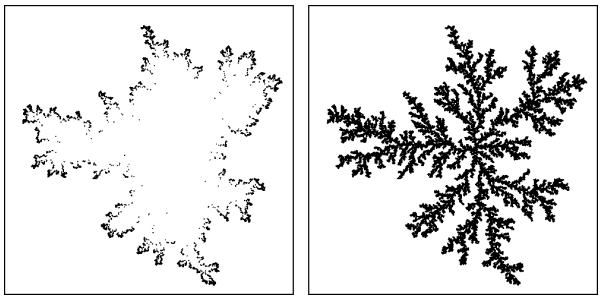

FIG. 1. Left panel, the boundary of the cluster probed by a random search with respect to the harmonic measure. Right panel, the boundary of the cluster probed by the present method.

region of a typical cluster of 50 000 particles that is being visited by a random search on the unit circle, with 50 000 samples. Like in direct simulations using random walks, the rarest events are not probed, and no serious conclusion regarding the phase transition is possible. Another method that cannot work is to try to compute $\langle \lambda_n^q \rangle$ by sampling on the arc length in a naive way. The reason is that the inverse map $[\Phi^{(n)}]^{-1}(s)$ cannot resolve θ values that belong to deep fjords. As the growth proceeds, reparametrization squeezes the θ values that map fjords into minute intervals, below the computer numerical resolution. To see this, consider the following estimate of the resolution we can achieve in the physical space:

$$\Delta\theta = \frac{\Delta s}{|\Phi^{(n)\prime}|} = \sqrt{\lambda_n}\frac{\Delta s}{\sqrt{\lambda_0}}, \tag{9}$$

or equivalently

$$\frac{\Delta s}{\sqrt{\lambda_0}} = \frac{\Delta\theta}{\sqrt{\lambda_n}}. \tag{10}$$

On the left hand side, we have the resolution in the physical space relative to the fixed linear size of the particles. With double precision numerics we can resolve values of $\Delta\theta \sim 10^{-16}$ and since we know that the values of $\lambda_{30\,000}$ can be as small as 10^{-70} inside the deepest fjords (and see below), we see that

$$\frac{\Delta s}{\sqrt{\lambda_0}} \sim \frac{10^{-16}}{10^{-35}} = 10^{19}. \tag{11}$$

Therefore, the resolution in the physcial space that is necessary to achieve a meaningful probe of the deep fjord is highly inappropriate.

The bottom line is that to compute the values of $\lambda_n(s)$ effectively we must use the full power of our iterated conformal dynamics, carrying the history with us, to iterate forward and backward at will to resolve accurately the θ and λ_n values associated with any given particle on the fully grown cluster.

To do this we recognize that every time we grow a semicircular bump we generate two new branch cuts in the map

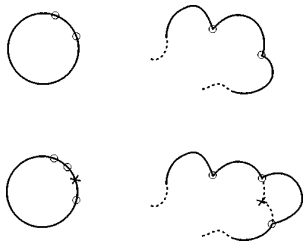

FIG. 2. A typical growth process in which an existing branch cut is "buried" under the new bump. Such events reduce the number of branch cuts below $2n$, with n being the number of particles.

$\Phi^{(n)}$. We find the position on the boundary between every two branch cuts, and there compute the value of λ_n. The first step in our algorithm is to generate the location of these points intermediate to the branch cuts [31]. Each branch cut has a preimage on the unit circle that will be indexed with three indices, $w_{j,\ell}^{k(\ell)} \equiv \exp[i\theta_{j,\ell}^{k(\ell)}]$. The index j represents the generation when the branch cut was created (i.e., when the jth particle was grown). The index ℓ stands for the generation at which the analysis is being done (i.e., when the cluster has ℓ particles). The index k represents the position of the branch cut along the arc length, and it is a function of the generation ℓ. Note that if two branch cuts belonging to the same bump are exposed, they get two consecutive indices. Since bumps may overlap during growth, branch cuts are then covered, cf. Fig. 2. Therefore, the maximal $k, k_{max} \leqslant 2\ell$. After each iteration the preimage of each branch cut moves on the unit circle, but its physical position remains. This leads to the equation that relates the indices of a still exposed branch cut that was created at generation j to a later generation n,

$$\begin{aligned}\Phi^{(n)}(w_{j,n}^{k(n)}) &\equiv \Phi^{(n)}(\phi^{-1}_{\lambda_n,\theta_n} \circ \ldots \circ \phi^{-1}_{\lambda_{j+1},\theta_{j+1}}(w_{j,j}^{\tilde{k}(j)})) \\ &= \Phi^{(j)}(w_{j,j}^{\tilde{k}(j)}).\end{aligned} \tag{12}$$

Note that the sorting indices $\tilde{k}(j)$ are not simply related to $k(n)$, and need to be tracked as follows. Suppose that the list $w_{j,n-1}^{k(n-1)}$ is available. In the nth generation we choose randomly a new θ_n, and find two new branch cuts that on the unit circle are at angles $\theta_n^{\pm}$. If one (or very rarely more) branch cut of the updated list $\phi^{-1}_{\lambda_n,\theta_n}(w_{j,n-1}^{k(n-1)})$ is covered, it is eliminated from the list, and together with the sorted new pair we make the list $w_{j,n}^{k(n)}$.

Next, let us find the midpositions at which we want to compute the value of λ_n. Having a cluster of n particles we now consider all neighboring pairs of preimages $w_{j,n}^{k(n)}$ and $w_{J,n}^{k(n)+1}$ that very well may have been created at two different generations j and J. The larger of these indices (J without loss of generality) determines the generation of the intermediate position at which we want to compute the field. We want to find the preimage $u_{J,J}^{k(n)}$ of this midpoint on the unit circle, to compute $\lambda_{k(n)}$ there accurately. Using definition (12) we find the preimage

$$\arg(u_{J,J}^{k(n)}) = [\arg(w_{j,J}^{\tilde{k}(J)}) + \arg(w_{J,J}^{\tilde{k}(J)+1})]/2. \quad (13)$$

In Fig. 1, right panel, we show, for the same cluster of 50 000, the map $\Phi^{(J)}(u_{J,J}^{k(n)})$ with $k(n)$ running between 1 and k_{max}, with J being the corresponding generation of creation of the midpoint. We see that now all the particles are probed, and every single value of $\lambda_{k(n)}$ can be computed.

To compute these $\lambda_{k(n)}$ accurately, we define [in analogy to Eq. (12)] for every $J<m\leqslant n$,

$$u_{J,m}^{k(n)} \equiv \phi^{-1}_{\lambda_m,\theta_m} \circ \ldots \circ \phi^{-1}_{\lambda_{j+1},\theta_{j+1}}(u_{J,J}^{k(n)}). \quad (14)$$

Finally, $\lambda_{k(n)}$ is computed from the definition (5) with

$$\Phi^{(n)\prime}(u_{J,n}^{k(n)}) = \phi'_{\lambda_n,\theta_n}(u_{J,n}^{k(n)}) \cdots \phi'_{\lambda_{J+1},\theta_{J+1}}(u_{J,J+1}^{k(n)}) \times \Phi^{(J)\prime}(u_{J,J}^{k(n)}). \quad (15)$$

We wish to emphasize the relevance of this equation: the problem with the coarse resolution that was exposed by Eq. (11) occurs only inside the deepest fjords. We note, however, that the particles inside the deep fjords were deposited when the clusters were still very small. For small clusters the resolution of the fjords does not pose a difficult problem. Therefore, when we evaluate the derivative $\Phi^{(n)}$ inside the deepest fjord at a point $u_{J,n}^{k(n)}$, we make use of the fact that $J\ll n$ and write the derivative in the form

$$\Phi^{(n)\prime}(u_{J,n}^{k(n)}) = \Phi^{(J)\prime}(u_{J,J}^{k(n)}) \cdot \delta, \quad (16)$$

where δ refers to correcting terms. On the left hand side of Eq. (15) we see that within our limited numerical resolution $u_{J,n}^{k(n)}$, $u_{J,n}^{k(n)+1}$ and the correponding values of λ_n are almost identical whereas for the right hand side (RHS) this is not the case. By keeping track of the branch cuts we improve the precision inside the fjords dramatically. In other words, the large screening inside the fjords is simultaneously the problem and the solution. The problem is that we cannot use the standard approach in evaluating $\Phi^{(n)\prime}$. The solution is that for a point $u_{J,n}^{k(n)}$ inside the deepest fjords we always have that $J\ll n$ and therefore the evaluation (15) helps to improve the resolution.

In summary, the calculation is optimally accurate since we avoid as much as possible the effects of the rapid shrinking of low probability regions on the unit circle. Each derivative in Eq. (15) is computed using information from a generation in which points on the unit circle are optimally resolved.

The integral (8) is then estimated as the finite sum $\sqrt{\lambda_0}\Sigma_{k(n)}\lambda_{k(n)}^q$. We should stress that for clusters of the order of 30 000 particles we already compute, using this algorithm, $\lambda_{k(n)}$ values of the order of 10^{-70}. To find the equivalent small probabilities using random walks would require about 10^{35} attempts to see them just once. This is of course impossible, explaining the lasting confusion about the issue of the phase transition in this problem. This also means that all the $f(\alpha)$ curves that were computed before [15,32] did not converge. Note that in our calculation the small values of $\lambda_{k(n)}$ are obtained from multiplication rather than addition, and therefore can be trusted.

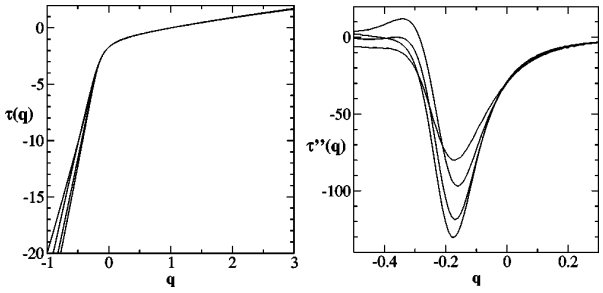

FIG. 3. Left panel, the calculated function $\tau(q)$ using clusters of n and $\bar{n}$ particles, with $n=5000$, 10 000, 15 000, and 25 000 and $\bar{n}=10\,000$, 15 000, 25 000, and 30 000, respectively. Right panel, the second derivative of $\tau(q)$ with respect to q. The minima of the curves get deeper when n is increased.

III. MULTIFRACAL ANALYSIS OF THE HARMONINC MEASURE

Having the accurate values $\lambda_{k(n)}$ we can now compute the moments (7). Since the scaling form on the RHS includes unknown coefficients, we compute the values of $\tau(q)$ by dividing $\langle\lambda_n^q\rangle$ by $\langle\lambda_{\bar{n}}^q\rangle$, estimating

$$\tau(q) \approx -D\frac{\ln\langle\lambda_n^q\rangle - \ln\langle\lambda_{\bar{n}}^q\rangle}{\ln n - \ln\bar{n}}. \quad (17)$$

Results for $\tau(q)$ for increasing values of n and $\bar{n}$ are shown in Fig. 3, left panel. It is seen that the value of $\tau(q)$ appears to grow without bound for q negative. The existence of a phase transition is however best indicated by measuring the derivatives of $\tau(q)$ with respect to q. In Fig. 3 right panel, we show the second derivative, indicating a phase transition at a value of q that recedes *away* from $q=0$ when n increases. Due to the high accuracy of our measurement of λ we can estimate already with clusters as small as 20–30 000 the q value of the phase transition as $q^*=-0.18\pm0.04$. It is quite possible that larger clusters would have indicated slighly more negative values of q^* (and see below the results of different methods of estimates), but we believe that this value is close to convergence. The fact that this is so can be seen from the $f(\alpha)$ curve that is plotted in Fig. 4. A test of convergence is that the slope of this function where it becomes essentially linear must agree with the q value of the phase transition. The straight line shown in Fig. 3 has the slope of -0.18, and it indeed approximates very accurately the slope of the $f(\alpha)$ curve where it stops being analytic. The reader should also note that the peak of the curve agrees with $D\approx1.71$, as well as the fact that $\tau(3)$ is also D as expected in this problem. The value of α_{max} is close to 20, which is higher than anything predicted before. It is nevertheless finite. We believe that this function is well converged, in contradistinction with past calculations.

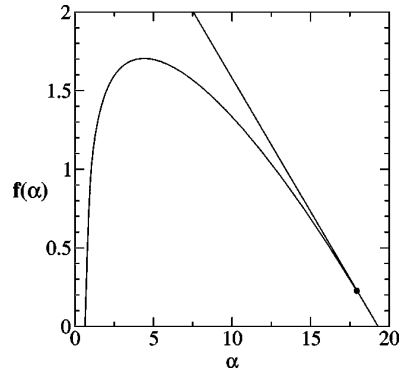

FIG. 4. Calculated function $f(\alpha)$ using $\tau(q)$ calculated from a cluster with $n=30\,000$ particles. This $f(\alpha)$ is almost indistinguishable from the one computed with $n=25\,000$ particles. We propose that this function is well converged. The black dot denotes where the curve ends, being tangent to the line with slope -0.18.

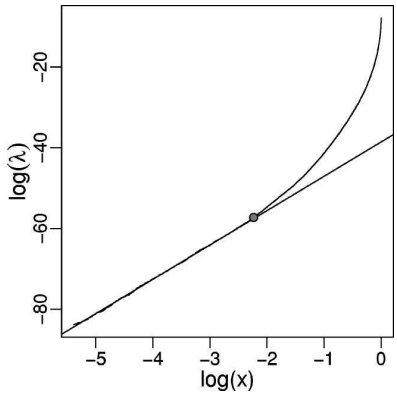

FIG. 5. Values of λ_n sorted in ascending order with respect to the variable $x=i/N$. This function is a pure power law for values of $\ln x$ smaller than the position of the circle. The power law is characterized by an exponent $\beta\approx 8.55$. This is consistent with a phase transition for $q^*\approx -0.23$.

IV. ALTERNATIVE WAY TO APPROACH THE PHASE TRANSITION

An alternative way to the multifractal analysis is obtained by first reordering all the computed values of $\lambda_{k(n)}$ in ascending order. In other words, we write them as a sequence $\{\lambda_n(i)\}_{i\in I}$, where I is an ordering of the indices such that $\lambda_n(i)\leqslant\lambda_n(j)$ if $i<j$. The number of samples we consider is usually large and therefore the discrete index i/N might be treated as a continuous index $0\leqslant x\leqslant 1$ and λ_n as a nondecreasing function of x,

$$\lambda_n\equiv g(x). \tag{18}$$

We next consider the distribution of $p(\lambda_n)$, which is calculated by the usual transformation formula

$$p(\lambda_n)\sim\int\delta[\lambda_n-g(x)]dx=\frac{1}{|g'[x(\lambda_n)]|}. \tag{19}$$

Using the distribution of λ_n, we now do the following rewritings:

$$\int_0^{2\pi}\lambda_n^q d\theta=\int_0^L\lambda_n^q\frac{d\theta}{ds}ds\sim\int_0^L\lambda_n^{q+1/2}ds \tag{20}$$

$$\sim\int_0^\infty\lambda_n^{q+1/2}p(\lambda_n)d\lambda_n. \tag{21}$$

In Fig. 5, we will show that our function $g(x)$ obeys a power law for low values of x,

$$g(x)\sim x^\beta \quad \text{for } x\ll 1. \tag{22}$$

This in turn implies a power-law dependence of $p(\lambda_n)$ on λ_n

$$p(\lambda_n)\sim\frac{1}{[x(\lambda_n)]^{\beta-1}}\sim\lambda_n^{(1-\beta)/\beta} \quad \text{for } \lambda_n\ll 1. \tag{23}$$

This power-law tail means that the moment integral (21) diverges for values of q below a critical value q_c given by

$$q_c+\frac{1}{2}+\frac{1-\beta}{\beta}=-1. \tag{24}$$

Thus, $q_c=-1/2-1/\beta$. From Eq. (7) we see that the value of q^* satisfied the relation

$$q^*=2q_c+1=-2/\beta. \tag{25}$$

In Fig. 5, we show how the values of λ_n depend on x for small values of x. The data are taken from a cluster with $n=20\,000$. Denoting the value of λ_n that is marked as a full circle by λ_c, the figure supports the existence of the power law (22) for values of λ_n smaller than λ_c. Needless to say this also implies that $p(\lambda_n)$ scales according to Eq. (23). By averaging over 16 clusters of size $n=20\,000$, we estimate the slope in Fig. 5 to be $\beta\approx 8.55$ or

$$q^*=-0.23\pm 0.05. \tag{26}$$

Obviously, this result is in agreement with our direct calculation in Sec. III.

V. GEOMETRICAL INTERPRETATION OF THE PHASE TRANSITION

At this point we would like to interpret the origin of the phase transition, which in light of the last section stems from the power-law behavior of $p(\lambda_n)$ for small values of λ_n. We first identify the region on the cluster that supports the low values of λ_n that belong to the power-law tail of $p(\lambda_n)$.

Consider again Fig. 5. The point denoted above as λ_c defines the maximum value for which we see a power law in λ_n vs x. Therefore, the set responsible for the phase transition is the union of bumps with a value of λ_n for which $\lambda_n<\lambda_c$. This set is referred to below as the "critical set," and is shown in Fig. 6, both on the background of the rest of the cluster, and as an isolated set. This figure suggests a geomet-

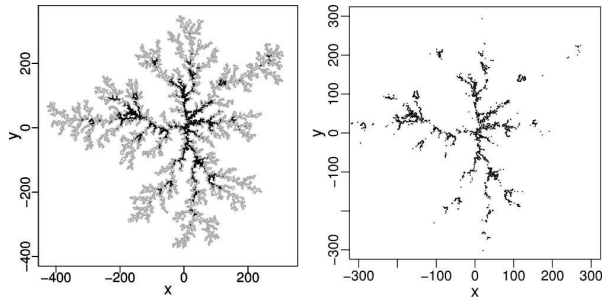

FIG. 6. Set of all particles that are associated with values of λ_n belonging to the power-law region shown in Fig. 5. In the left panel, we show the set on the background of the cluster in gray; and in the right panel, the set isolated from the rest of the cluster.

ric interpretation: the fjords in the figure all seem to have a characteristic angle. We will try first to confirm this impression using careful numerics.

Clearly, the set has several fjords; we consider them individually. Figure 7 shows an example of such a fjord. For each fjord we find the point with the minimum probability and use this for defining the bottom (or deepest point). Second, from the inside, we move to the two adjacent points which together with the deepest point define an angle. This angle is recorded, and we move to the next pair of points, and so on until the value of λ_n exceeds λ_c. Figure 7, right panel shows how the angle varies with the number of steps k. For most of the fjords considered the angle is quite large for a small number of steps (up to 3 to 4 steps). As more steps are taken the angle settles on a characteristic value around which it fluctuates. For a larger number of steps we reach the outer parts of the fjord and the angle does no longer reflect the geometry inside the fjord. The dependence of the angle on k as shown in Fig. 7 is typical for all the fjords of the set causing the phase transition and therefore we see a peak in the distribution of all the measured angles. This peak identifies an angle that is characteristic to the fjords. Figure 8 is the distribution of such typical angles over one cluster. We determine the characteristic angle, say γ_c by locating the maximum of the distribution. Finally, we calculated the average of the charateristic angle γ_c over 15 clusters of size n $=20\,000$. On the basis of that we determine the angle to be

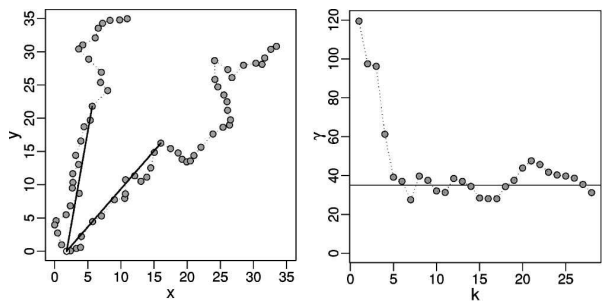

FIG. 7. Left panel, a typical deep fjord resolved on the scale of the particles. From the deepest particle the angle is computed as explained in the text. Right panel, the change of the measured angle γ as a function of the number of steps k away from the deepest particle. The angle settles on a value that depends only weakly on k.

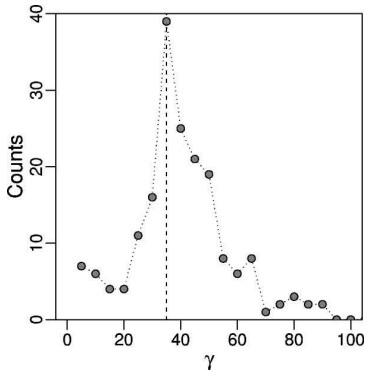

FIG. 8. Distribution of angles γ as determined by the procedure exemplified in Fig. 7 over the set shown in Fig. 6.

$$\gamma_c = 35^\circ \pm 6^\circ. \tag{27}$$

Finally, we can offer a geometrical model to interpret the phase transition. The results presented in this section indicate that to a reasonable approximation the least accessible fjords can be modeled as a wedge of included angle γ_c. In the Appendix, we compute the power law expected for $p(\lambda_n)$ for a wedge. The final result is

$$p(\lambda_n) \sim \lambda_n^{-(2\eta-3)/2(\eta-1)}, \tag{28}$$

where $\gamma_c = \pi/\eta$. Using our numerical result for γ_c and Eq. (25) we predict finally $q^* = -0.24 \pm 0.05$. Obviously, this is in agreement with the previous findings.

In addition, we should comment on the interpretation of $f(\alpha_{max})$ that is the value of the $f(\alpha)$ curve at the point of loss of analyticity. Within the wedge model offered here, this must be the fractal dimension of the set of wedges that support the scaling law (28). We have attempted to determine this dimension numerically by counting the number of fjords in the critical set shown in Fig. 7 as a function of the number of paricles n in the cluster. While the result of such a calculation is consistent with the proposition, the available statistics is not sufficient to establish it firmly. We thus conclude with the proposition as a conjecture, i.e., that $f(\alpha_{max})$ can be interpreted as the dimension of the set of fjords that belong to the critical set.

VI. CONCLUDING REMARKS

In conclusion, we have used the method of iterated conformal maps to compute accurately the harmonic measure of DLA clusters of moderate size. We have explained that we must use the full power of the method in order to overcome the strong contraction of the regions on the unit circle that belong to the deep fjords. By iterating back and forth, using the fact that we own the history of the iteration scheme, we could resolve probabilities as small as 10^{-35}. Using this data we could establish beyond doubt that the generalized dimensions [or, equivlently, the $f(\alpha)$ function] lose analyticity at a negative value of q, implying the existence of α_{max}. In order to understand the loss of analyticity, we offer a geometric

picture. We identified the critical set on the cluster as having harmonic probabilities that belong to the power-law tail of $p(\lambda_n)$. Considering this set we identified fjords that can be modeled as wedges of characteristic angle. Taking such wedges as a model for the fjords of the critical set, we found a value of q^* that is very close to the one computed using other methods. We thus propose that the point of nonanalyticity can be interpreted as resulting from the power-law dependence of the harmonic measure in the fjords belonging to the critical set.

ACKNOWLEDGMENTS

This work has been supported in part by the Petroleum Research Fund, The European Commission under the TMR program, and the Naftali and Anna Backenroth-Bronicki Fund for Research in Chaos and Complexity. A. L. is supported by of the Minerva Foundation, Munich, Germany.

APPENDIX: WEDGE MODEL FOR THE FJORDS OF THE CRITICAL SET

1. The conformal map and the electric field

The conformal function

$$\chi(w)=\left(i\frac{w+1}{w-1}\right)^{1/\eta} \tag{A1}$$

maps the outside of the unit circle to the inside of a wedge with opening angle $\gamma_c=\pi/\eta$, where $\eta\geqslant 1$ allows γ_c be vary between 0 and π. To calculate the electric field E, we need the inverse of χ:

$$\chi^{-1}(z)=\frac{z^{\eta}+i}{z^{\eta}-i}. \tag{A2}$$

From here we see that $\chi^{-1}(0)=-1$ and

$$\Phi^{-1}(\rho\exp[i\pi(1\pm 1)/2\eta])\to 1 \quad \text{as} \quad \rho\to\infty. \tag{A3}$$

Thus, the unit circle is unfolded onto the wedge; shifting the point $w=-1$ to the origin $z=0$; and rotating and stretching the upper half circle onto the real axis and the lower half circle to the other ray of the wedge $\rho e^{i\pi/\eta}$. The electric field follows from its definition

$$E(z)=\left|\frac{d}{dz}\ln[\chi^{-1}(z)]\right|=\frac{2\eta}{|z|}\frac{1}{|z^{\eta}+z^{-\eta}|}. \tag{A4}$$

On the real axis close to the center $z=0$, i.e., for $z=\rho\ll 1$ it becomes

$$E(\rho)=\frac{2\eta}{\rho}\frac{1}{\rho^{\eta}+\rho^{-\eta}}\approx 2\eta\rho^{\eta-1} \quad \text{for} \quad \rho\ll 1, \tag{A5}$$

while for large ρ is goes like

$$E(\rho)=\frac{2\eta}{\rho}\frac{1}{\rho^{\eta}+\rho^{-\eta}}\approx 2\eta\rho^{-(\eta+1)} \quad \text{for} \quad \rho\gg 1. \tag{A6}$$

Exactly the same relations hold for the upper ray.

2. The probability measure for λ_n

The linear size of the particles in mathematical space $\sqrt{\lambda_n}$ is proportional to the electric field,

$$\sqrt{\lambda_n}(\theta)=\sqrt{\lambda_0}E(\Phi(e^{i\theta})). \tag{A7}$$

Thus, the probability measure of the λ_n is directly related to the probability measure of the electric field. Since E is the same for the two rays of the wedge, it is sufficient to consider it only on the real axis. Starting from the uniform distribution of the θ values in mathematical space, it follows:

$$\begin{aligned}1&=\frac{dP(\theta)}{d\theta}=\frac{dP(E)}{dE}\left|\frac{dE}{d\rho}\right|\left|\frac{d\rho}{d\theta}\right|\\&=\frac{dP}{dE}\left|\frac{dE}{d\rho}\right|\left|-i\frac{d}{d\rho}\ln[\Phi^{-1}(\rho)]\right|^{-1}\\&=\frac{dP}{dE}\left|\frac{dE}{d\rho}\right|E^{-1}\end{aligned} \tag{A8}$$

or

$$dP(E)\sim\left|\frac{dE}{d\rho}(\rho)\right|^{-1}E\,dE. \tag{A9}$$

The derivative of the electric field follows from (A5) or (A6),

$$\left|\frac{dE}{d\rho}(\rho)\right|=\frac{2\eta}{\rho^2}\frac{|(\eta+1)\rho^{\eta}-(\eta-1)\rho^{-\eta}|}{(\rho^{\eta}+\rho^{-\eta})^2}, \tag{A10}$$

yielding

$$dP(E)\sim\frac{\rho(\rho^{\eta}+\rho^{-\eta})}{|(\eta+1)\rho^{\eta}-(\eta-1)\rho^{-\eta}|}dE. \tag{A11}$$

For small ρ corresponding to a small field and thus small $\sqrt{\lambda_n}$ we get

$$dP(E)\sim\rho dE\sim E^{1/(\eta-1)} \tag{A12}$$

or

$$dP(\sqrt{\lambda_n})\sim\sqrt{\lambda_n}^{-1/(\eta-1)}d\sqrt{\lambda_n}. \tag{A13}$$

For the probability density of λ_n this means

$$dP(\lambda_n)=\frac{dP(\sqrt{\lambda_n})}{d\sqrt{\lambda_n}}\frac{d\lambda_n}{2\sqrt{\lambda_n}} \tag{A14}$$

$$\sim\lambda_n^{-(2\eta-3)/2(\eta-1)}d\lambda_n. \tag{A15}$$

[1] D. Ruelle, *Statistical Mechanics, Thermodynamic Formalism* (Addison- Wesley, Reading, MA, 1978).
[2] P. Grassberger and I. Procaccia, Phys. Rev. Lett. **50**, 346 (1983).
[3] J.-P. Eckmann and D. Ruelle, Rev. Mod. Phys. **57**, 617 (1985).
[4] R. Rammal, C. Tannous, P. Breton, and A.-M.S. Tremblay, Phys. Rev. Lett. **54**, 1718 (1985).
[5] L. de Arcangelis, S. Redner, and A. Coniglio, Phys. Rev. B **31**, 4725 (1985).
[6] T.A. Witten and L.M. Sander, Phys. Rev. Lett. **47**, 1400 (1981).
[7] T.C. Halsey, P. Meakin, and I. Procaccia, Phys. Rev. Lett. **56**, 854 (1986).
[8] B. Duplantier, Phys. Rev. Lett. **84**, 1363 (2000).
[9] M. Hastings, Phys. Rev. Lett. **88**, 055506 (2002); e-print cond-mat/0109304.
[10] H.G.E. Hentschel and I. Procaccia, Physica D **8**, 435 (1983).
[11] T.C. Halsey, M.H. Jensen, L.P. Kadanoff, I. Procaccia, and B.I. Shraiman, Phys. Rev. A **33**, 1141 (1986).
[12] J. Balatoni and A. Renyi, Publ. Math. (Debrecen) **1**, 9 (1956).
[13] J.D. Farmer, Physica (Utrecht) **4D**, 366 (1982).
[14] L.A. Turkevich and H. Scher, Phys. Rev. Lett. **55**, 1026 (1985).
[15] C. Amitrano, A. Coniglio, and F. di Liberto, Phys. Rev. Lett. **57**, 1016 (1986).
[16] J. Nittmann, H.E. Stanley, E. Touboul, and G. Daccord, Phys. Rev. Lett. **58**, 619 (1987). In this paper, the viscous fingering pattern was digitized and the harmonic measure was then calculated. There was no direct measurement of the harmonic measure.
[17] K.J. Måløy, F. Boger, J. Feder, and T. Jøssang, in *Time-Dependent Effects in Disordered Materials*, edited by R. Pynn and T. Riste (Plenum, New York, 1987), p. 111.
[18] T. Bohr, P. Cvitanović, and M.H. Jensen, Europhys. Lett. **6**, 445 (1988).
[19] P. Cvitanović, in *Proceedings of the XIV Colloquium on Group Theoretical Methods in Physics*, edited by R. Gilmore (World Scientific, Singapore, 1987); in *Non-Linear Evolution and Chaotic Phenomena*, edited by P. Zweifel, G. Gallavotti, and M. Anile (Plenum, New York, 1988).
[20] J. Lee and H.E. Stanley, Phys. Rev. Lett. **61**, 2945 (1988).
[21] S. Schwarzer, J. Lee, A. Bunde, S. Havlin, H.E. Roman, and H.E. Stanley, Phys. Rev. Lett. **65**, 603 (1990).
[22] R. Blumenfeld and A. Aharony, Phys. Rev. Lett. **62**, 2977 (1989).
[23] A.B. Harris and M. Cohen, Phys. Rev. A **41**, 971 (1990).
[24] R.C. Ball and R. Blumenfeld, Phys. Rev. A **44**, 828 (1991).
[25] B. Davidovitch, M.H. Jensen, A. Levermann, J. Mathiesen, and I. Procaccia, Phys. Rev. Lett. **87**, 164101 (2001).
[26] M.B. Hastings and L.S. Levitov, Physica D **116**, 244 (1998).
[27] B. Davidovitch, H.G.E. Hentschel, Z. Olami, I. Procaccia, L.M. Sander, and E. Somfai, Phys. Rev. E **59**, 1368 (1999).
[28] B. Davidovitch, M.J. Feigenbaum, H.G.E. Hentschel, and I. Procaccia, Phys. Rev. E **62**, 1706 (2000).
[29] B. Davidovitch and I. Procaccia, Phys. Rev. Lett., **85**, 3608 (2000).
[30] B. Davidovitch, A. Levermann, and I. Procaccia, Phys. Rev. E **62**, R5919 (2000).
[31] F. Barra, B. Davidovitch, and I. Procaccia (unpublished); e-print cond-mat/0105608.
[32] Y. Hayakawa, S. Sato, and M. Matsushita, Phys. Rev. A **36**, 1963 (1987).

3.3 Serial versus parallel Laplacian growth

Physical Review Letters

Volume **87** (2001)

page 134501

VOLUME 87, NUMBER 13 PHYSICAL REVIEW LETTERS 24 SEPTEMBER 2001

Laplacian Growth and Diffusion Limited Aggregation: Different Universality Classes

Felipe Barra, Benny Davidovitch, Anders Levermann, and Itamar Procaccia
Department of Chemical Physics, The Weizmann Institute of Science, Rehovot 76100, Israel
(Received 5 March 2001; published 7 September 2001)

It had been conjectured that diffusion limited aggregates and Laplacian growth patterns (with small surface tension) are in the same universality class. Using iterated conformal maps we construct a one-parameter family of fractal growth patterns with a continuously varying fractal dimension. This family can be used to bound the dimension of Laplacian growth patterns from below. The bound value is higher than the dimension of diffusion limited aggregates, showing that the two problems belong to two different universality classes.

DOI: 10.1103/PhysRevLett.87.134501 PACS numbers: 47.27.Gs, 05.40.–a, 47.27.Jv

Laplacian growth patterns are obtained when the boundary Γ of a two-dimensional domain is grown at a rate proportional to the gradient of a Laplacian field P. Outside the domain $\nabla^2 P = 0$, and each point of Γ is advanced at a rate proportional to $\mathbf{\nabla} P$ [1]. It is well known that without ultraviolet regularization such growth results in finite time singularities [2]. In correspondence with experiments on viscous fingering one usually adds surface tension, or in other words solves the above problem with the boundary condition $P = \sigma\kappa$ where σ is the surface tension and κ the local curvature of Γ [3]. The other boundary condition is that as $r \to \infty$ the flux is $\mathbf{\nabla} P = \text{const} \times \hat{r}/r$. Figure 1 (left) shows a typical Laplacian growth pattern.

Diffusion limited aggregation (DLA) [4] begins with fixing one particle at the center of coordinates in 2 dimensions, and follows the creation of a cluster by releasing fixed size random walkers from infinity, allowing them to walk around until they hit any particle belonging to the cluster. Since the particles are released one by one and may take an arbitrarily long time to hit the cluster, the probability field is quasistationary and in the complement of the cluster we have again $\nabla^2 P = 0$. In this case the boundary condition on the cluster is $P = 0$, but finite time singularities are avoided by having finite size particles. The boundary condition at infinity is exactly as above. A typical DLA is shown in Fig. 1 (right).

In spite of the different ultraviolet regularizations of Laplacian growth and DLA, it was speculated by many authors [5] that the two problems belong to the same "universality class," and it was expected that the resulting fractal patterns will have the same dimension. In this Letter, we argue that this is not the case: there are deep differences between the two problems, and in particular Laplacian growth patterns have a dimension considerably higher than DLA. In one sentence, the differences between the problems stem from the fact that Laplacian patterns are grown layer by layer, whereas DLA is grown particle by particle. Unfortunately, traditional techniques used to grow Laplacian growth patterns, either numerical [6] or experimental [7], fail to achieve patterns large enough to extract reliable dimensions (see Fig. 9 in [6], for example). The numerical algorithms are extremely time consuming due to the stiffness of the equations involved; experimentally it is difficult to construct large quasi-two-dimensional (Hele-Shaw) cells without introducing serious deformations.

The aim of this Letter is to provide a scheme to simulate the zero surface tension Laplacian growth that has a finite size regularization and thus does not suffer from finite time singularities. We introduce a 1-parameter family of growth processes based on iterated conformal maps [8,9]. Contrary to DLA which grows particle by particle, we will construct the family of growth processes to mimic Laplacian growth, in which a layer is added to the boundary Γ at each growth step, with a width proportional to the gradient of the field. Consider then $\Phi^{(n)}(\omega)$ which conformally maps the exterior of the unit circle $e^{i\theta}$ in the mathematical ω plane onto the complement of the (simply connected) cluster of n particles in the physical z plane. The unit circle is mapped onto the boundary of the cluster. The map $\Phi^{(n)}(\omega)$ is made from compositions of elementary maps $\phi_{\lambda,\theta}$, $\Phi^{(n)}(\omega) = \Phi^{(n-1)}(\phi_{\lambda_n,\theta_n}(\omega))$, where the elementary map $\phi_{\lambda,\theta}$ transforms the unit circle to a circle with a "bump" of linear size $\sqrt{\lambda}$ around the point $\omega = e^{i\theta}$. In this Letter, we employ the elementary map [8]

$$\phi_{\lambda,0}(\omega) = \sqrt{\omega}\left\{\frac{(1+\lambda)}{2\omega}(1+\omega)\left[1+\omega+\omega\left(1+\frac{1}{\omega^2}-\frac{2}{\omega}\frac{1-\lambda}{1+\lambda}\right)^{1/2}\right]-1\right\}^{1/2} \quad (1)$$

$$\phi_{\lambda,\theta}(\omega) = e^{i\theta}\phi_{\lambda,0}(e^{-i\theta}\omega). \quad (2)$$

With this choice the map $\Phi^{(n)}(\omega)$ adds on a new semicircular bump to the image of the unit circle under $\Phi^{(n-1)}(\omega)$. The bumps in the z plane simulate the accreted particles in the physical space formulation of the growth process. The recursive dynamics can be represented as iterations of the map $\phi_{\lambda_n,\theta_n}(\omega)$,

$$\Phi^{(n)}(\omega) = \phi_{\lambda_1,\theta_1} \circ \phi_{\lambda_2,\theta_2} \circ \ldots \circ \phi_{\lambda_n,\theta_n}(\omega). \quad (3)$$

With the present technique it is also straightforward to determine the dimension. The conformal map $\Phi^{(n)}(\omega)$

 © 2001 The American Physical Society

VOLUME 87, NUMBER 13 PHYSICAL REVIEW LETTERS 24 SEPTEMBER 2001

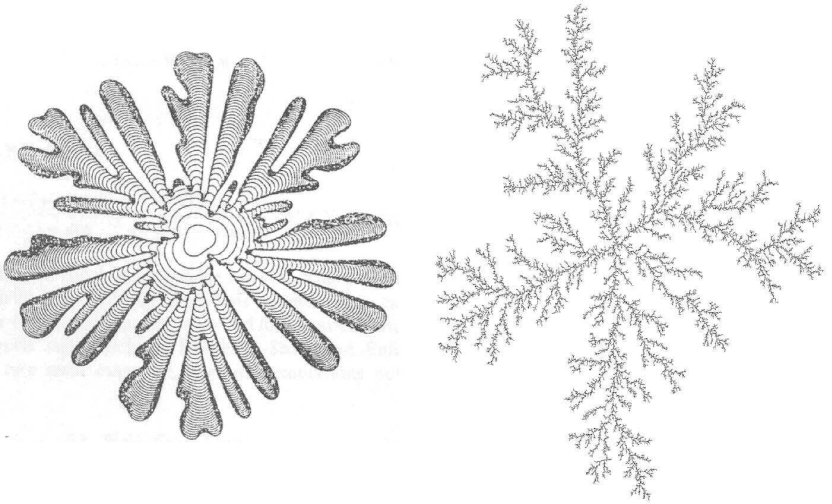

FIG. 1. Left: Typical Laplacian growth pattern with surface tension; cf. Ref. [6]. Right: Typical DLA cluster of 100 000 particles.

admits a Laurent expansion

$$\Phi^{(n)}(\omega) = F_1^{(n)}\omega + F_0^{(n)} + \frac{F_{-1}^{(n)}}{\omega} + \cdots . \tag{4}$$

The coefficient of the linear term is the Laplace radius, and was shown to scale as

$$F_1^{(n)} \sim S^{1/D}, \tag{5}$$

where S is the area of the cluster (the sum of the actual areas of the bumps in the physical space). On the other hand, $F_1^{(n)}$ is given analytically by

$$F_1^{(n)} = \prod_{k=1}^{n} \sqrt{(1 + \lambda_k)}, \tag{6}$$

and therefore can be determined very accurately.

Different growth processes can be constructed by proper choices of the itineraries $\{\theta_i\}_{i=1}^n$ [10], and rules for determining the areas of the bumps $\{\lambda_i\}_{i=1}^n$. In DLA growth [8,9]one wants to have *fixed size* bumps in the physical space, say of fixed area λ_0. Then one chooses in the nth step

$$\lambda_n = \frac{\lambda_0}{|\Phi^{(n-1)'}(e^{i\theta_n})|^2}, \qquad \text{DLA growth.} \tag{7}$$

The probability to add a particle to the boundary of the DLA cluster is the harmonic measure, which is uniform on the circle. Thus in DLA the itinerary $\{\theta_i\}_{i=1}^n$ is random, with uniform probability for θ_i in the interval $[0, 2\pi]$.

For our present purposes we want to grow a *layer* of particles of varying sizes, proportional to the gradient of the field, rather than *one* particle of fixed size. This entails three major changes. First, if we want to grow *one* particle of size proportional to the gradient of the field (i.e., area proportional to $|\Phi^{(n-1)'}(e^{i\theta_n})|^{-2}$) we need to choose

$$\lambda_n = \frac{\lambda_0}{|\Phi^{(n-1)'}(e^{i\theta_n})|^4}, \qquad \text{present models.} \tag{8}$$

Second, to grow a layer, we need to accrete many particles without updating the conformal map. In other words, to add a new layer of p particles when the cluster contains m particles, we need to choose p angles on the unit circle $\{\tilde{\theta}_{m+k}\}_{k=1}^p$. At these angles we grow bumps which in the physical space are proportional in size to the gradient of the field around the m-particle cluster:

$$\lambda_{m+k} = \frac{\lambda_0}{|\Phi^{(m)'}(e^{i\tilde{\theta}_{m+k}})|^4}, \qquad k = 1, 2 \ldots, p . \tag{9}$$

Last, and very importantly, we need to choose the itinerary $\{\tilde{\theta}_{m+k}\}_{k=1}^p$ which defines the layer. This itinerary is chosen to achieve a uniform coverage of the unit circle *before* any growth takes place. The parameter that will distinguish one growth model from another, giving us a 1-parameter control, is the *degree of coverage*. In other words, we introduce the parameter

$$C = \frac{1}{\pi} \sum_{k+1}^{p} \sqrt{\lambda_{m+k}} . \tag{10}$$

This parameter is the fraction of the unit circle which is covered in each layer, with the limit of Laplacian growth obtained with $C = 1$. It turns out to be rather time consuming to grow fractal patterns with C close to unity. But we will show below that this is hardly necessary; already for C of the order of $1/2$ we will find patterns whose fractal dimension significantly exceeds that of DLA, offering a clear lower bound on the dimension of Laplacian growth patterns.

Once a layer with coverage C had been grown, the field is updated. To do this, we define a series $\{\theta_k\}_{k=1}^p$ according to

$$\Phi^{(m)}(e^{i\tilde{\theta}_{m+k}}) \equiv \Phi^{(m+k-1)}(e^{i\theta_{m+k}}) . \tag{11}$$

Next we define the conformal map used in the next layer growth according to

$$\Phi^{(m+p)}(\omega) \equiv \Phi^{(m)} \circ \phi_{\theta_{m+1},\lambda_{m+1}} \circ \ldots \circ \phi_{\theta_{m+p},\lambda_{m+p}}(\omega) . \tag{12}$$

It is important to notice that on the face of it this conformal map appears very similar to the one obtained in DLA,

VOLUME 87, NUMBER 13 PHYSICAL REVIEW LETTERS 24 SEPTEMBER 2001

Eq. (3). But this is deceptive; the distribution of θ values is different, we do not update the map after each particle, and the growth rule is different.

We can achieve a uniform coverage C using various itineraries. One way is to construct the "golden mean trajectory" $\tilde{\theta}_{m+k+1} = \tilde{\theta}_{m+k} + 2\pi\rho$ where $\rho = (\sqrt{5} - 1)/2$. At each step we check whether the newly grown bump may overlap a previous one in the layer. If it does, this growth step is skipped and the orbit continues until a fraction C is covered. Another method is random choices of $\tilde{\theta}_{m+k}$ with the same rule of skipping overlaps. We have tried several other itineraries. Of course, to be an acceptable model of Laplacian growth the resulting cluster should be invariant to the itinerary. This invariance is demonstrated below. The central thesis of this work is that the dimension of the resulting growth patterns is dependent on C only, and not on the itinerary chosen to achieve it. Numerically it is more efficient to use the golden mean itinerary since it avoids as much as possible previously visited regions. In order to achieve comparable growth rates for different layers we inflated λ_0 in Eq. (9) according to $\lambda_0 \to m\lambda_0$ in the layer composed of p particles $\{m + k\}_{k=1}^{p}$. In Fig. 2 we show F_1 of clusters grown by choosing 3 different itineraries to produce the layers and for two values of C.

We conclude that the dimension (determined by the asymptotic behavior of F_1 vs S) does not depend on the itinerary used to form the layers but on C only.

In Fig. 3 we show three fractal patterns grown with this method, with three different values of C. Even a cursory observation should convince the reader that the dimension of these patterns grows upon increasing C.

In order to calculate the dimension we averaged F_1 of many clusters produced by the golden mean itinerary, each with another random initial angle in each layer. Plots of the averages $\langle F_1 \rangle$ for 3 values of C are presented in Fig. 4.

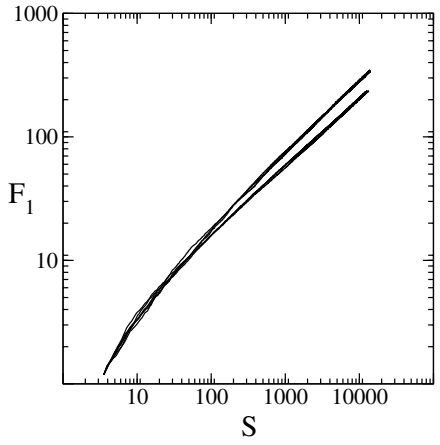

FIG. 2. Log-log plots of F_1 vs S of six individual clusters, using three different itineraries for layer construction, with two values of C. $C = 0.3$ (upper group) and $C = 0.5$ (lower group). Here we use the golden-mean, random, and period doubling itineraries (see Ref. [10]).

We conclude that the dimension of the growth pattern increases monotonically with C, with $D \approx 1.85$ when $C = 0.6$.

The main point of this analysis is that the dimension of Laplacian growth patterns is bounded from below by the supremum on the dimensions obtained in this family of models. First, Laplacian growth calls for $C = 1$.

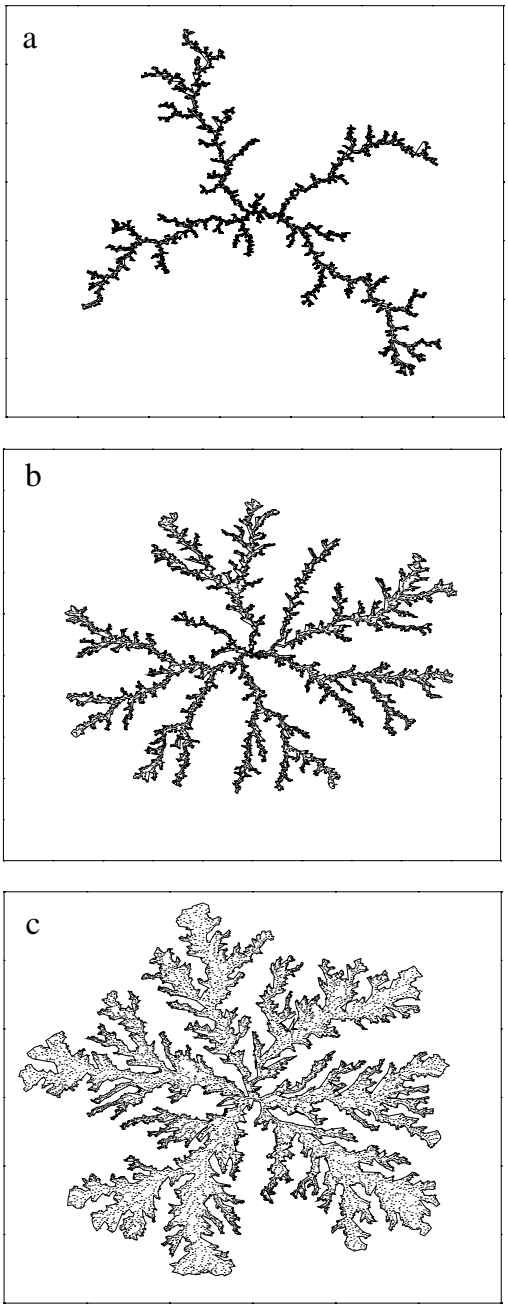

FIG. 3. Patterns grown with three different values of C by using the golden-mean itinerary: (a) $C = 0.1$; (b) $C = 0.3$; (c) $C = 0.5$.

VOLUME 87, NUMBER 13 PHYSICAL REVIEW LETTERS 24 SEPTEMBER 2001

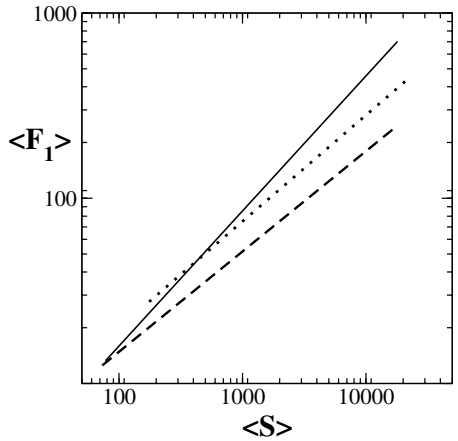

FIG. 4. Linear regressions of log-log plots of $\langle F_1 \rangle$ vs S for three values of C: 0.1 (solid line); 0.3 (dotted line); and 0.6 (dashed line). The slopes of the curves imply dimensions $D = 1.37$, $D = 1.75$, and $D = 1.85$, respectively. The averages are taken over at least 20 clusters.

Second, in Laplacian growth the boundary condition is $P = \sigma\kappa$, suppressing growth at the tips (and relatively favoring growth in the fjords) compared to growth with the boundary condition $P = 0$. Accordingly, on the basis of the results shown in Fig. 4, we propose that the dimension of Laplacian growth patterns exceeds 1.85, putting it distinctively away from the dimension of DLA, which is about 1.71 [11]. We stress that there may be slow crossovers in the dimension estimates, but if these exist they tend to *underestimate* the dimension, leaving our bound intact.

In hindsight, it is difficult to understand how the consensus formed in favor of DLA and Laplacian growth being in the same universality class. Superficially, one could say that in DLA the update of the harmonic measure after each particle is not so crucial, since the effect of such an update is relatively *local* [12]. Thus it may just work that a full layer of particles would be added to the cluster before major interaction between different growth events takes place. However, this view is completely wrong. An incoming random walker lands on top of a previously attached one *very often.* To see this, consider how many angles $\{\theta_j\}$ can be chosen *randomly* on the unit circle before the first overlap between bumps [of linear sizes $\epsilon_j = \sqrt{\lambda_n(e^{i\theta_j})}$]. To get the order of magnitude take $\epsilon_j = \epsilon = \langle\sqrt{\lambda_n}\rangle$. The average number of times that we can choose randomly an angle before the first overlap is $\mathcal{N}(\epsilon) \sim \frac{1}{\sqrt{\epsilon}}$. The length of the unit circle that is covered at that time by the already chosen bumps is $\mathcal{L}(\epsilon) = \epsilon\mathcal{N}(\epsilon) \sim \sqrt{\epsilon}$. It was shown in [9] that for DLA $\langle\lambda_n\rangle \sim \frac{1}{n}$, so that $\epsilon \sim \frac{1}{\sqrt{n}}$, implying $\mathcal{N}(n) \sim n^{1/4}$. Notice that this result means in particular that for a DLA cluster of 1 million particles only less than 50 random walkers can be attached before two of them will arrive at the same site. Moreover, $\mathcal{L}(n) \sim \frac{1}{n^{1/4}} \to 0$ for $n \to \infty$, which means that as the DLA cluster grows, our coverage parameter C goes to zero, rather than to unity where Laplacian growth is. Taking spatial fluctuations of λ_n into account may change the exact exponents, but not the qualitative result. This argument clarifies the profound difference between growing a whole layer simultaneously and particle by particle. Note, however, that DLA is *not* the $C \to 0$ limit of our 1-parameter family due to the difference between Eqs. (7) and (8).

The results of this study underline once more the delicacy of the issues involved. Fractal patterns depend sensitively on the details of the growth rules. Even though the analytic presentation seems very similar, to the degree that many researchers were led to believe in wide universality classes, we showed here that one must be much more cautious. By lifting the models into *families* of growth patterns depending on a parameter we could demonstrate strong variability of the fractal dimension. Here we constructed the family to bound from below Laplacian growth patterns. A similar family can be constructed to bound DLA from above. This and other aspects of this method will be reported elsewhere.

This work has been supported in part by the Petroleum Research Fund, the European Commission under the TMR program, and the Naftali and Anna Backenroth-Bronicki Fund for Research in Chaos and Complexity.

[1] P. G. Saffman and G. I. Taylor, Proc. R. Soc. London A **245**, 312 (1958).
[2] B. Shraiman and D. Bensimon, Phys. Rev. A **30**, 2840 (1984); S. D. Howison, J. Fluid Mech. **167**, 439 (1986).
[3] D. Bensimon, L. P. Kadanoff, S. Liang, B. I. Shraiman, and C. Tang, Rev. Mod. Phys. **58**, 977 (1986); S. Tanveer, Philos. Trans. R. Soc. London A **343**, 155 (1993), and references therein.
[4] T. A. Witten and L. M. Sander, Phys. Rev. Lett. **47**, 1400 (1981).
[5] L. Paterson, Phys. Rev. Lett. **52**, 1621 (1984); L. M. Sander, Nature (London) **322**, 789 (1986); J. Nittmann and H. E. Stanley, Nature (London) **321**, 663 (1986); H. E. Stanley, in *Fractals and Disordered Systems*, edited by A. Bunde and S. Havlin (Springer-Verlag, Berlin, 1991).
[6] T. Y. Hou, J. S. Lowengrub, and M. J. Shelley, J. Comput. Phys. **114**, 312 (1994).
[7] E. Ben-Jacob, R. Godbey, N. D. Goldenfeld, J. Koplik, H. Levine, T. Mueller, and L. M. Sander, Phys. Rev. Lett. **55**, 1315 (1985); J. D. Chen, Exp. Fluids **5**, 363 (1987); A. Arneódo, Y. Couder, G. Grasseau, V. Hakim, and M. Rabaud, Phys. Rev. Lett. **63**, 984 (1989).
[8] M. B. Hastings and L. S. Levitov, Physica (Amsterdam) **116D**, 244 (1998).
[9] B. Davidovitch, H. G. E. Hentschel, Z. Olami, I. Procaccia, L. M. Sander, and E. Somfai, Phys. Rev. E **59**, 1368 (1999).
[10] B. Davidovitch, M. J. Feigenbaum, H. G. E. Hentschel, and I. Procaccia, Phys. Rev. E **62**, 1706 (2000).
[11] P. Meakin, Phys. Rev. A **26**, 1495–1507 (1983); B. Davidovitch, A. Levermann, and I. Procaccia, Phys. Rev. E **62**, R5919 (2000).
[12] T. C. Halsey, Phys. Rev. Lett. **72**, 1228 (1994).

3.4 Two-dimensionality of parallel Laplacian growth

Physical Review E

Volume **66** (2002)

page 016308

PHYSICAL REVIEW E **66**, 016308 (2002)

Transition in the fractal properties from diffusion-limited aggregation to Laplacian growth via their generalization

H. George E. Hentschel,* Anders Levermann, and Itamar Procaccia
Department of Chemical Physics, The Weizmann Institute of Science, Rehovot 76100, Israel
(Received 29 November 2001; published 29 July 2002)

We study the fractal and multifractal properties (i.e., the generalized dimensions of the harmonic measure) of a two-parameter family of growth patterns that result from a growth model that interpolates between diffusion-limited aggregation (DLA) and Laplacian growth patterns in two dimensions. The two parameters are β that determines the size of particles accreted to the interface, and $\mathcal{C}$ that measures the degree of coverage of the interface by each layer accreted to the growth pattern at every growth step. DLA and Laplacian growth are obtained at $\beta=0$, $\mathcal{C}=0$ and $\beta=2$, $\mathcal{C}=1$, respectively. The main purpose of this paper is to show that there exists a line in the β-$\mathcal{C}$ phase diagram that separates fractal ($D<2$) from nonfractal ($D=2$) growth patterns. Moreover, Laplacian growth is argued to lie in the nonfractal part of the phase diagram. Some of our arguments are not rigorous, but together with the numerics they indicate this result rather strongly. We first consider the family of models obtained for $\beta=0$, $\mathcal{C}>0$, and derive for them a scaling relation $D=2D_3$. We then propose that this family has growth patterns for which $D=2$ for some $\mathcal{C}>C_{\rm cr}$, where $C_{\rm cr}$ may be zero. Next we consider the whole β-$\mathcal{C}$ phase diagram and define a line that separates two-dimensional growth patterns from fractal patterns with $D<2$. We explain that Laplacian growth lies in the region belonging to two-dimensional growth patterns, motivating the main conjecture of this paper, i.e., that Laplacian growth patterns are two dimensional. The meaning of this result is that the branches of Laplacian growth patterns have finite (and growing) area on scales much larger than any ultraviolet cutoff length.

DOI: 10.1103/PhysRevE.66.016308 PACS number(s): 47.27.Gs, 47.27.Jv, 05.40.−a

I. INTRODUCTION

In recent work [1,2] we have introduced a model of fractal growth processes that interpolates between diffusion-limited aggregation (DLA) [3] and Laplacian growth patterns [4,5], and employed this model to show that these processes are not in the same universality class. The aim of this paper is to study the fractal properties of the resulting clusters. In particular, we will be led to conjecture that Laplacian growth is asymptotically of dimension 2, and in this sense is not a fractal at all. This is in contradistinction to DLA for which the dimension had been computed to be 1.713 . . . [6].

Laplacian growth patterns are obtained when the boundary Γ of a two-dimensional domain is grown at a rate proportional to the gradient of a Laplacian field P. Outside the domain $\nabla^2 P=0$, and each point of Γ is advanced at a rate proportional to ∇P [4,5]. In DLA [3] a two-dimensional cluster is grown by releasing fixed size random walkers from infinity, allowing them to walk around until they hit any particle belonging to the cluster. Since the particles are released one by one and may take arbitrarily long time to hit the cluster, the probability field is quasistationary and in the complement of the cluster we have again $\nabla^2 P=0$. The boundary condition at infinity is the same for the two problems; in radial geometry as $r\to\infty$ the flux is $\nabla P=\text{const}\times\hat{r}/r$. Since the probability for a random walker to hit the boundary is again proportional to $|\nabla P|$, one could think that in the asymptotic limit when the size of the particle is much smaller than the radius of the cluster, repeated growth events lead to a growth process that is similar to Laplacian growth. Of course, the ultraviolet regularizations in the two processes were taken different; in studying Laplacian growth one usually solves the problem with the boundary condition $P=\sigma\kappa$ where σ is the surface tension and κ the local curvature of Γ [7]. Without this (or some other) ultraviolet regularization Laplacian growth reaches a singularity (cusps) in finite time [5]. In DLA the ultraviolet regularization is provided by the finite size of the random walkers. However, many researchers believed [8] that this difference, which for very large clusters controls only the smallest scales of the fractal patterns, were not relevant, expecting the two models to lead to the clusters with the same asymptotic dimensions. While we argued recently that the difference in ultraviolet regularization is indeed not crucial [2], the two problems are, nevertheless, in two different universality classes. To establish this we have constructed a family of growth processes that includes DLA and a discrete version of Laplacian growth as extreme members, using the same ultraviolet regularization (and see Sec. II for a further discussion of the regularization). We thus exposed the essential difference between DLA and Laplacian growth. DLA is grown serially, with the field being updated after each particle growth. On the other hand, all boundary points of a Laplacian pattern are advanced in parallel at once (proportional to ∇P). We showed that this difference is fundamental to the asymptotic dimension, putting the two problems in different universality classes [1]. Here we wish to go further and suggest that Laplacian growth patterns are two-dimensional.

In Sec. II we review briefly the two-parameter model that had been introduced to establish these results. We discuss

*Permanent address: Department of Physics, Emory University, Atlanta, GA.

 ©2002 The American Physical Society

there the two parameters β and $\mathcal{C}$ that are used to interpolate between DLA and Laplacian growth. In Sec. III we analyze the generalized dimensions D_q and relate them to the scaling of moments of objects which are natural to the theory. In Sec. IV we discuss first a family of growth models which is a one-parameter generalization of DLA ($\beta=0$, $0\leqslant\mathcal{C}\leqslant 1$), and show that the fractality of DLA is lost for some $\mathcal{C}>\mathcal{C}_{\rm cr}$ in favor of two-dimensional growth patterns. It is not impossible that $\mathcal{C}_{\rm cr}=0$. For growth patterns in this family we derive a scaling relation $D=2D_3$. Under some plausible assumptions we propose that for $\mathcal{C}>\mathcal{C}_{cr}$ there exists another scaling relation, i.e., $D=1+D_2$, which implies immediatly that $D=2$. Second, we discuss the one-parameter family of models that generalizes Laplacian growth ($\beta=2$, $0\leqslant\mathcal{C}\leqslant 1$) and show that the above relation is not obtained here, leading to the existence of fractal patterns also for high values of $\mathcal{C}$. Finally, in Sec. V we reach the main conjecture of this paper, i.e., that Laplacian growth patterns are two-dimensional. In Sec. VI we offer a discussion and some open questions that are left for future research.

II. ITERATED CONFORMAL MAPS FOR PARALLEL GROWTH PROCESSES

The method of iterated conformal maps for DLA was introduced in Ref. [9]. In Refs. [1,2] we have presented a generalization to parallel growth processes. We were interested in $\Phi^{(n)}(w)$ that conformally maps the exterior of the unit circle $e^{i\theta}$ in the mathematical w plane onto the complement of the (simply connected) cluster of n particles in the physical z plane. The unit circle is mapped onto the boundary of the cluster. In what follows we use the fact that the gradient of the Laplacian field $P[z(s)]$ is

$$|P[z(s)]|=\frac{1}{|\Phi^{(n)'}(e^{i\theta})|},\quad z(s)=\Phi^{(n)}(e^{i\theta}). \tag{1}$$

Here s is an arc-length parametrization of the boundary. The map $\Phi^{(n)}(w)$ is constructed recursively. Suppose that we have already $\Phi^{(n)}(w)$ that maps to the exterior of a cluster of n particles in the physical plane and we want to find the map $\Phi^{(n+p)}(w)$ after p additional particles were added to its boundary *at once*, each proportional in size to the local value of $|P|^{\beta/2}$. To grow *one* such particle we employ the elementary map $\phi_{\lambda,\theta}$ that transforms the unit circle to a circle with a semispherical "bump" of linear size $\sqrt{\lambda}$ around the point $w=e^{i\theta}$,

$$\phi_{\lambda,0}(w)=\sqrt{w}\left\{\frac{(1+\lambda)}{2w}(1+w)\left[1+w+w\left(1+\frac{1}{w^2}-\frac{2}{w}\frac{1-\lambda}{1+\lambda}\right)^{1/2}\right]-1\right\}^{1/2}, \tag{2}$$

$$\phi_{\lambda,\theta}(w)=e^{i\theta}\phi_{\lambda,0}(e^{-i\theta}w). \tag{3}$$

If we update the field after the addition of this single particle, then

$$\Phi^{(n+1)}(w)=\Phi^{(n)}(\phi_{\lambda_{n+1},\theta_{n+1}}(w)), \tag{4}$$

where $\Phi^{(n)}(e^{i\theta_{n+1}})$ is the point on which the $(n+1)$th particle is grown and $\sqrt{\lambda_n}$ is the size of the grown particle divided by the Jacobian of the map, $\Phi'^{(n)}(e^{i\theta_{n+1}})$, at that point.

The map $\Phi^{(n+1)}(w)$ adds on a new semicircular bump to the image of the unit circle under $\Phi^{(n)}(w)$. The bumps in the z plane simulate the accreted particles in the physical space formulation of the growth process. For the height of the bump to be proportional to $|\nabla P(z(s))|^{\beta/2}$ we need to choose its area proportional to $|\Phi^{(n)'}(e^{i\theta_{n+1}})|^{-\beta}$ [see Eq. (1)], or

$$\lambda_{n+1}=\frac{\lambda_0}{|\Phi^{(n)'}(e^{i\theta_{n+1}})|^{\beta+2}}\ . \tag{5}$$

Here $\lambda_0\equiv\tilde{\lambda}_0^{(\beta+2)/2}$ and $\tilde{\lambda}_0$ is a fixed typical area. With this choice λ_n is dimensionless. With $\beta=0$ these rules produce a DLA cluster, for which the particles are of constant area. With $\beta=2$ we grow bumps in the physical space whose linear scale is proportional to the gradient of the field $|\nabla P[z(s)]|$, as is appropriate for Laplacian growth. Next, to grow p (nonoverlapping) particles in parallel, we accrete them without updating the conformal map. In other words, to add a new layer of p particles when the cluster contains m particles, we need to choose p angles on the unit circle $\{\tilde{\theta}_{m+k}\}_{k=1}^{p}$. At these angles we grow bumps that in the physical space have the wanted linear scale (ranging from constant to proportional to the gradient of the field),

$$\lambda_{m+k}=\frac{\lambda_0}{|\Phi^{(m)'}(e^{i\tilde{\theta}_{m+k}})|^{\beta}|\Phi^{(m+k-1)'}(e^{i\theta_{m+k}})|^2},\qquad k=1,2\ldots,p. \tag{6}$$

At this moment the θ_{m+k} are not defined; only the $\tilde{\theta}_{m+k}$. This is due to the reparametrization that needs to be taken into account as explained next.

Of course, every composition effects a reparametrization of the unit circle, which has to be taken into account. To do this, we define a series $\{\theta_{m+k}\}_{k=1}^{p}$ according to

$$\Phi^{(m)}(e^{i\tilde{\theta}_{m+k}})\equiv\Phi^{(m+k-1)}(e^{i\theta_{m+k}}). \tag{7}$$

After the p particles were added, the conformal map and thus the field should be updated. In updating, we will use p compositions of the elementary map $\phi_{\lambda,\theta}(w)$. Next we define the conformal map used in the next layer growth according to

$$\Phi^{(m+p)}(\omega)\equiv\Phi^{(m)}\circ\phi_{\theta_{m+1},\lambda_{m+1}}\circ\cdots\circ\phi_{\theta_{m+p},\lambda_{m+p}}(\omega). \tag{8}$$

In this way we achieve the growth at the images under $\Phi^{(m)}$ of the points $\{\tilde{\theta}_{m+k}\}_{k=1}^{p}$. To compute the θ series from a given $\tilde{\theta}$ series we use Eq. (8) to rewrite Eq. (7) in the form

$$e^{i\theta_{m+k}}=\phi^{-1}_{\theta_{m+k-1},\lambda_{m+k-1}}\circ\cdots\circ\phi^{-1}_{\theta_{m+1},\lambda_{m+1}}(e^{i\tilde{\theta}_{m+k}}). \tag{9}$$

The inverse map $\phi_{\theta,\lambda}^{-1}$ is given by $\phi_{\theta,\lambda}^{-1}(\omega) = e^{i\theta}\phi_{0,\lambda}^{-1}(e^{-i\theta}\omega)$ with

$$\phi_{0,\lambda}^{-1} = \frac{\lambda\omega^2 \pm \sqrt{\lambda^2\omega^4 - \omega^2[1-(1+\lambda)\omega^2][\omega^2-(1+\lambda)]}}{1-(1+\lambda)\omega^2}, \tag{10}$$

where the positive root is taken for Re $\omega > 0$ and the negative root for Re $\omega < 0$.

Evidently, Laplacian growth calls for choosing the series $\{\tilde{\theta}_{m+k}\}_{k=1}^{p}$ such as to have full coverage of the unit circle (implying the same for the boundary Γ). On the other hand, DLA calls for growing a single particle before updating the field. Since it was shown [10] that in DLA growth λ_n decreases on the average when n increases, in the limit of large clusters DLA is consistent with vanishingly small coverage of the unit circle. To interpolate between these two cases we introduce a parameter that serves to distinguish one growth model from the other, giving us a two-parameter control (the other parameter is β). This parameter is the *degree of coverage*. Since the area covered by the preimage of the nth particle on the unit circle is approximately $2\sqrt{\lambda_n}$, we introduce the parameter

$$\mathcal{C} = \frac{1}{\pi}\sum_{k=1}^{p}\sqrt{\lambda_{m+k}}. \tag{11}$$

(In Ref. [2] we showed how to measure the coverage exactly.) Since this is the fraction of the unit circle which is covered in each layer, the limit of Laplacian Growth is obtained with $\mathcal{C}=1$. DLA is asymptotically consistent with $\mathcal{C}=0$. Of course, the two models differ also in the size of the growing bumps, with DLA having fixed size particles [$\beta=0$ in Eq. (5)], and Laplacian growth having particles proportional to ∇P [$\beta=2$ in Eq. (6)]. Together with $\mathcal{C}$ we have a two parameter control on the parallel growth dynamics, with DLA and Laplacian growth occupying two corners of the $\beta,\mathcal{C}$ plane, at the points (0,0) and (2,1), respectively.

Obviously, the partially serial growth within the layer introduces an additional freedom that is the *order* of placement of the bumps on the unit circle. In Refs. [1,2] we have shown that the order is in fact immaterial as far as the asymptotic fractal properties of the clusters are concerned. Accordingly, we will take random choices of $\tilde{\theta}_{m+k}$ with a rule of skipping overlaps.

We should note that in our approach the regularization of putative singularities is not achieved with surface tension, but by having a minimal size bump, similarly to the regularization of DLA. Our rules of growth with $\beta=2$ and λ_0 chosen once and for all, guarantee that every layer of growth has exactly the same area. This in the continuous time Laplacian growth model translates to a particular choice of the time step dt. Clearly, one has freedom in choosing dt, or of the size λ_0 in each layer, as long as this does not affect the nature of the growth. In particular, we can have λ_0 chosen such that the maximal physical bump is of constant area. Once λ_0 is chosen, the sharpest feature that can be achieved is a bump of size λ_0, and the worst possible "singularity" is a line of such bumps, exactly as in DLA. Thus the putative cusp singularity of Laplacian growth is avoided in a manner that is identical for all the growth models in our two-parameter family.

The conformal map $\Phi^{(n)}(\omega)$ admits a Laurent expansion

$$\Phi^{(n)}(\omega) = F_1^{(n)}\omega + F_0^{(n)} + \frac{F_{-1}^{(n)}}{\omega} + \cdots. \tag{12}$$

The coefficient of the linear term is the Laplace radius, and was shown to scale like

$$F_1^{(n)} \sim S^{1/D}, \tag{13}$$

where S is the area of the cluster

$$S = \sum_{j=1}^{n}\lambda_j|\Phi'^{(j-1)}(e^{i\theta_j})|^2. \tag{14}$$

Note that for $\beta=0$ this and Eq. (5) imply that $S=n\lambda_0$. Indeed for $\beta=0$ this estimate had been carefully analyzed and substantiated (up to a factor) in Ref. [11]. On the other hand, $F_1^{(n)}$ is given analytically by

$$F_1^{(n)} = \prod_{k=1}^{n}\sqrt{(1+\lambda_k)}, \tag{15}$$

and therefore can be determined very accurately.

The conclusion from the calculations presented in Refs. [1,2] is that for $\mathcal{C}>0$ the fractal dimension of the growth patterns depends continuously on the parameters, growing monotonically upon decreasing β or increasing $\mathcal{C}$. It is quite obvious why increasing $\mathcal{C}$ should increase the dimension. By forbidding particles to overlap we simply force them into the fjords, not allowing them to hit the tips only (as is highly probable). Also decreasing β increases the dimension, since we grow larger particles into the fjords, whereas increasing β reduces the size of particles added to fjords and increases the size of particles that accrete onto tips. In particular, we argued that DLA and our discretized Laplacian growth cannot have the same dimensions, putting them in different universality classes. In the rest of this paper we make these observations more quantitative and precise.

III. MULTIFRACTAL PROPERTIES

A. Generalized dimensions

The fractal dimension in the β-$\mathcal{C}$ family of models, $D(\beta,C)$, is introduced as the exponent relating the area of the cluster S_n to its linear scale [which is measured by the (dimensionless) Laplace radius $F_1^{(n)}$],:

$$S_n \sim (F_1^{(n)})^{D(\beta,C)}\tilde{\lambda}_0. \tag{16}$$

In this equation $\tilde{\lambda}_0 \equiv \lambda_0^{2/(2+\beta)}$. The multifractal exponents [12] are defined in analogy to those for DLA in terms of the moments of the (dimensionless) electric field $E(s)$ on the boundary of the cluster [13],

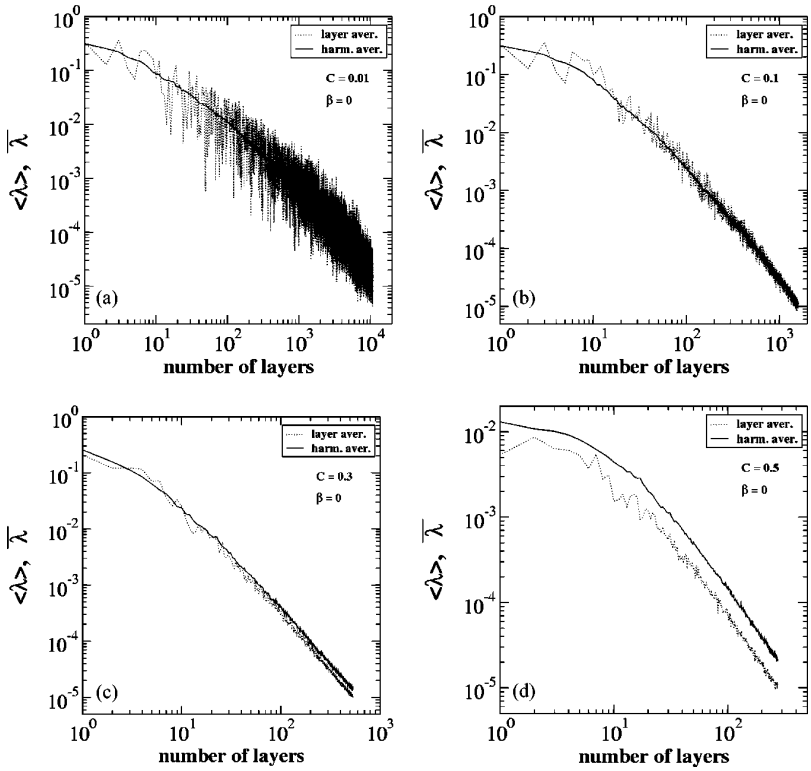

FIG. 1. Layer and harmonic averages of λ_n as a function of the number of layers, for $\beta=0$. Panels (a)–(d), $\mathcal{C}=0.01$, 0.1, 0.3, and 0.5, respectively.

$$\langle E^{(q-1)}\rangle \sim (F_1^{(n)})^{-(q-1)D_q(\beta,C)} \sim (S_n/\tilde{\lambda}_0)^{-(q-1)D_q(\beta,C)/D(\beta,C)}, \tag{17}$$

where $\langle\cdots\rangle$ represents the harmonic average for the (β,C) clusters in question. Note that these exponents are for a fixed size partition with boxes of length $\sqrt{\tilde{\lambda}_0}$, with asymptotics for an infinitely large cluster. A supremum over arbitrary partitions may lead to different exponents, cf. Ref. [14].

This result translates immediately [10] to the multifractal fluctuations of the bump areas λ_n added in the mathematical plane. As $\lambda_n^q \sim E_n^{(2+\beta)q}$, where E_n is the field computed at $z(s)=\Phi^{(n)}(e^{i\theta_n})$. We therefore write

$$\langle \lambda_n^q\rangle \sim (S_n/\tilde{\lambda}_0)^{-(2+\beta)qD_{(2+\beta)q+1}(\beta,C)/D(\beta,C)}. \tag{18}$$

Specifically, we can derive the following important moments:

$$\langle \sqrt{\lambda_n}\rangle \sim (S_n/\tilde{\lambda}_0)^{-(1+\beta/2)D_{(2+\beta/2)}/D},$$
$$\langle \lambda_n\rangle \sim (S_n/\tilde{\lambda}_0)^{-(2+\beta)D_{3+\beta}/D}, \tag{19}$$
$$\langle \lambda_n^{\beta/(2+\beta)}\rangle \sim (S_n/\tilde{\lambda}_0)^{-\beta D_{1+\beta}/D},$$

where naturally all the dimensions are functions of (β,C). We can also estimate the way in which the maximal bump areas scale

$$\lambda_{n,max} \equiv \lim_{q\to\infty}\langle \lambda_n^q\rangle^{1/q} \sim (S/\tilde{\lambda}_0)^{-(2+\beta)D_\infty(\beta,C)/D(\beta,C)}. \tag{20}$$

Consider now the addition of one layer of p particles to the growing cluster. We can rewrite Eq. (11) as

$$C=(1/\pi)p\overline{\sqrt{\lambda_n}}, \tag{21}$$

where we have introduced the notation $\overline{\lambda_n^q}$ to represent the average over a layer of p particles,

$$\overline{f(\lambda_n)} \equiv \frac{1}{p}\sum_{k=1}^{p} f(\lambda_{n+k}). \tag{22}$$

For our considerations below it is important to relate the layer averages $\overline{\lambda_n^q}$ to harmonic averages $\langle\lambda_n^q\rangle$. This relationship may very well depend on the value of β. The two cases that are of highest interest to us are $\beta=0$ and $\beta=2$, and we will examine them separately.

IV. SCALING RELATIONS FOR THE FRACTAL DIMENSION *D*

A. The case $\beta=0$ and $\mathcal{C}>0$

We examine the relationship between layer and harmonic averages numerically. In Fig. 1 we show the two averages vs the number of layers for the case $q=1$, $\beta=0$ and four values of $\mathcal{C}$. In Fig. 2 we show the same for the case $q=0.5$, $\beta=0$ and the same four values of $\mathcal{C}$.

Examining the results it appears that for the higher values of $\mathcal{C}$ we can assume that in the scaling sense

$$\overline{\lambda_n^q} \sim \langle\lambda_n^q\rangle, \quad \beta=0. \tag{23}$$

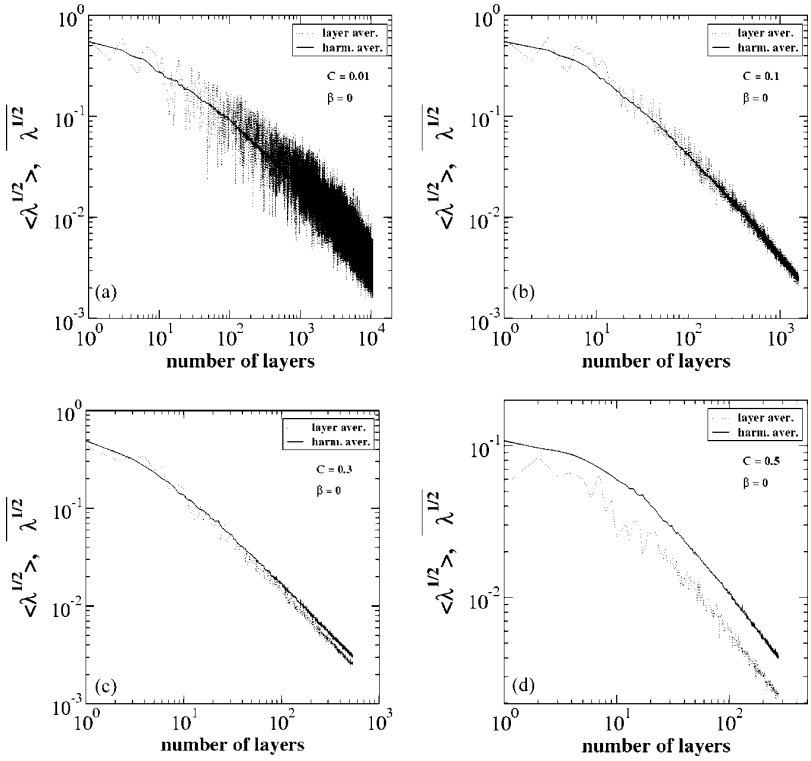

FIG. 2. Layer and harmonic averages of $\lambda_n^{0.5}$ as a function of the number of layers, for $\beta=0$. Panels (a)–(d), $\mathcal{C}=0.01$, 0.1, 0.3, and 0.5, respectively.

Note that for smaller values of $\mathcal{C}$ the evidence is not as clear cut as for higher values. The number of points p in each layer is relatively small and the layer average is highly fluctuating. Nevertheless, even for the case $\mathcal{C}=0.01$, if we perform a running average on the layer average data, we converge very well onto the harmonic average. We therefore propose to proceed with the conjecture that Eq. (23) is correct for all the values of $\mathcal{C}$ and $\beta=0$, and investigate the implications of this scaling relation for the cases for which it is correct. An immediate consequence of Eqs. (21) and (23) is that

$$p\sim\mathcal{C}/\langle\sqrt{\lambda_n}\rangle\sim\mathcal{C}(S/\tilde{\lambda}_0)^{D_2/D}. \tag{24}$$

We note that this means that $p\to\infty$ asymptotically for every value of $\mathcal{C}$, while $p/n\to 0$.

Next observe that by definition

$$F_1^{(n+p)}/F_1^{(n)}=\Pi_{k=1}^{p}(1+\lambda_{n+k})^a\approx 1+ap\overline{\lambda_n}. \tag{25}$$

In light of Eq. (16) we write

$$\frac{S_{n+p}}{S_n}=\left(\frac{F_1^{(n+p)}}{F_1^{(n)}}\right)^D\approx 1+aDp\overline{\lambda_n}. \tag{26}$$

On the other hand, we estimate

$$\frac{S_{n+p}}{S_n}\approx 1+\frac{p\tilde{\lambda}_0}{S_n}, \tag{27}$$

and comparing with Eq. (26) we find

$$S_n\approx\frac{\tilde{\lambda}_0}{aD\overline{\lambda_n}}. \tag{28}$$

If Eq. (23) is used, we find finally

$$S_n\approx\tilde{\lambda}_0\left(\frac{S_n}{\tilde{\lambda}_0}\right)^{2D_3/D}, \tag{29}$$

from which we derive the well known ''electrostatic relation,''

$$D=2D_3. \tag{30}$$

This result was known for $\mathcal{C}=0$ [15], and is generalized here, under the conjecture (23) to all values of $\mathcal{C}$.

Let us consider now the probability to hit at the point of maximal radius. We propose that for any finite $\mathcal{C}$ the probability for this event is finite. We stress that this ''point'' is actually a region on the interface of size $\sqrt{\tilde{\lambda}_0}$ in every layer. In particular, we expect that the growth process will hit the point of maximal radius every finite number of layers, where this number is of the order of $1/\mathcal{C}$. We also know for sure that we have at most one hit per layer since particles cannot overlap in the dynamics.

Consider now the scaling of the size of the growth pattern, which is measured by $F_1^{(n)}$. First we know that $F_1^{(n)}\sim(S/\tilde{\lambda}_0)^{1/D}$, and therefore

$$dF_1^{(n)}/dS\sim(S/\tilde{\lambda}_0)^{1/D-1}/\tilde{\lambda}_0. \tag{31}$$

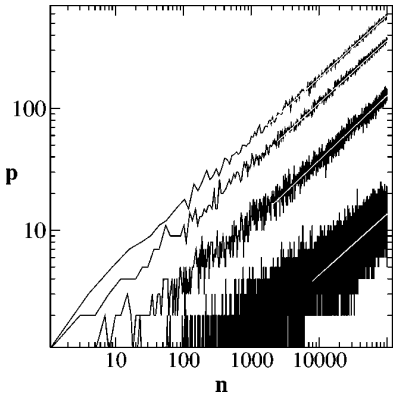

FIG. 3. The number p of bumps in a layer vs the number n of bumps in the growth pattern, in a log-log plot. From top to bottom that is shown for $\mathcal{C}=0.5$, 0.3, 0.1, and 0.01, respectively. In white lines we show the scaling laws $p\sim n^{1/2}$; this law fits the data for $\mathcal{C}\geqslant 0.1$ and is not in contradiction with the (noisy) data even for $\mathcal{C}=0.01$.

On the other hand, we estimate the same object using the following argument: the maximal radius $R^{(n)}$ increases by $\sqrt{\tilde{\lambda}_0}$ every time that it is hit. This occurs every $1/\mathcal{C}$ layers in which p particles were added. Therefore

$$\frac{dR^{(n)}}{dS}\sim\frac{\sqrt{\tilde{\lambda}_0}}{p\tilde{\lambda}_0/\mathcal{C}}. \tag{32}$$

Comparing Eqs. (31) and (32), using Eq. (24) we obtain the scaling relation

$$D=1+D_2. \tag{33}$$

Using the inequalities between the generalized dimensions and Eq. (31) we write

$$D-1=D_2\geqslant D_3=D/2 \quad \text{for all } \mathcal{C}>\mathcal{C}_{\mathrm{cr}}, \tag{34}$$

which is equivalent to

$$D=2 \quad \text{for all } \mathcal{C}>\mathcal{C}_{\mathrm{cr}}. \tag{35}$$

In other words, we conclude that along the line $\beta=0$ in the phase diagram β-$\mathcal{C}$, there exists a transition to growth patterns of dimension 2.

Since our arguments are not rigorous and the result quite surprising, we will examine the assumptions using an additional consideration. From Eqs. (33) and (34) it follows that $D_2=1$, and from Eq. (24) it then follows that p scales like

$$p\sim S^{1/2}, \quad \mathcal{C}>\mathcal{C}_{\mathrm{cr}}. \tag{36}$$

This prediction is examined directly in Fig. 3. We see that it is obeyed extremely well for all the values of $\mathcal{C}\geqslant 0.1$, and it is not in contradiction with the data even for $\mathcal{C}=0.01$. We therefore cannot exclude the possibility that $\mathcal{C}_{\mathrm{cr}}=0$.

To gain intuition to the meaning of this result we show in Fig. 4 the actual growth patterns for $\beta=0$ and $\mathcal{C}=0.01$, 0.1, 0.3, and 0.5, respectively. To plot these figures we find *all* the exposed branch cuts on the unit circles which are associated

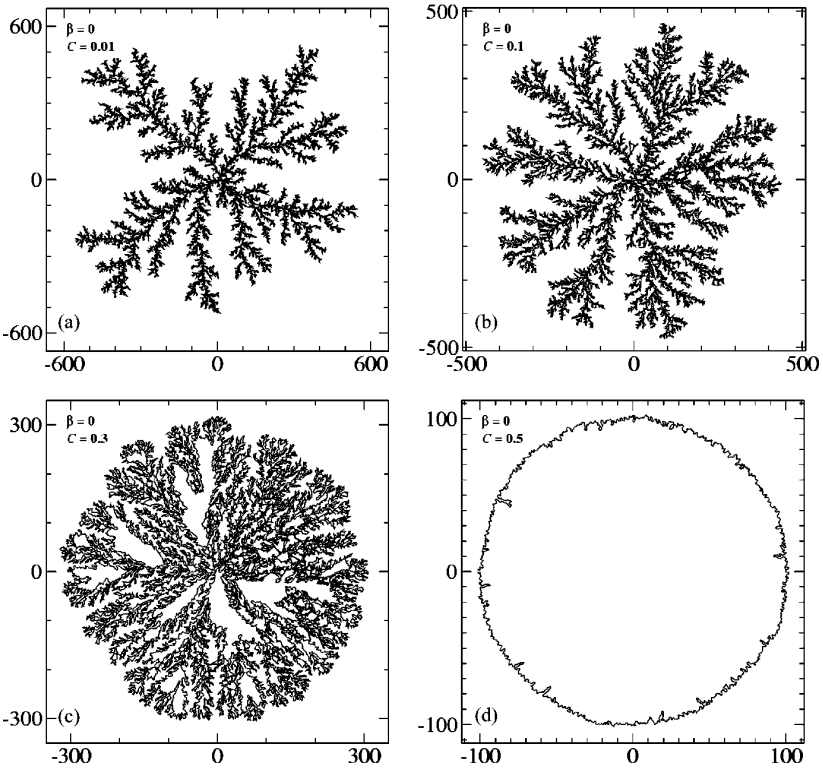

FIG. 4. Clusters for $\beta=0$. Panels (a)–(d), $\mathcal{C}=0.01$, 0.1, 0.3, and 0.5, respectively. Note the areas significantly larger than the UV cutoff λ_0, which appear already for $\mathcal{C}=0.01$.

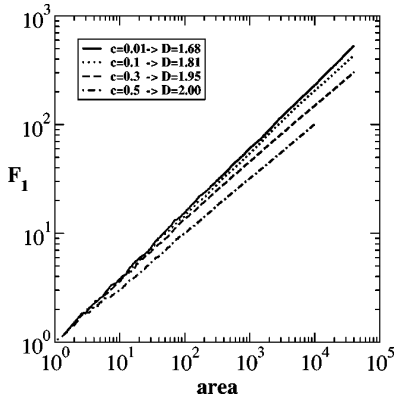

FIG. 5. The first Laurent coefficient $F_1^{(n)}$ as a function of the area for $\beta=0$ and $\mathcal{C}=0.01$, 0.1, 0.3, and 0.5. The fractal dimension D is obtained for the slope via $F_1^{(n)} \sim \sqrt{\lambda_0}(S/\lambda_0)^{1/D}$.

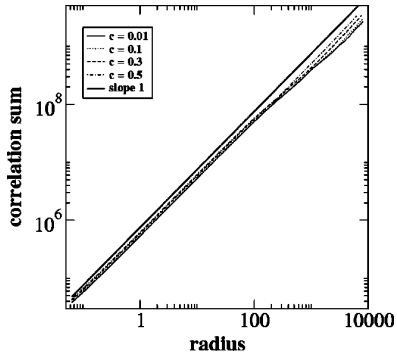

FIG. 6. The correlation dimension D_2 for $\beta=0$ and $\mathcal{C}=0.01$, 0.1, 0.3, and 0.5. The thick line has slope 1, indicating that $D_2=1$ and therefore $D=2$ for all shown $\mathcal{C}$.

with the bumps added in the growth process (see Ref. [2] for details). Then we plot the image of all these points under the conformal map and connect them by lines. Thus we are guaranteed that what is plotted is the actual contour of the growth pattern, of the image of the unit circle in the mathematical domain, with all the fjords fully resolved. We see that even with the lowest value of $\mathcal{C}$ the branches appear to gain substance as they grow, having a width that is larger than $\sqrt{\lambda_0}$ (the typical corrugation of the interface). Consequently it is not impossible that $D=2$ even for the lowest values of $\mathcal{C}>0$. If this is so, it is not due to the existence of an ultraviolet cutoff, but due to the finiteness of $\mathcal{C}$. With $\mathcal{C}=0$ (the DLA limit) the serial algorithm favors strongly truly fractal patterns. The parallel growth algorithm with finite $\mathcal{C}$ squeezes more substance into the fjords, reducing that tendency. For higher values of $\mathcal{C}$ it becomes obvious that the growth patterns are two dimensional, and for $\mathcal{C}=0.5$ the pattern grows like a roughened disk. The main conclusion of this analysis is that we certainly cross somewhere along the line $\beta=0$ into growth patterns that are two-dimensional. Whether or not the critical value of $\mathcal{C}$ is finite or zero cannot be determined by numerics alone.

If we accept the possibility that even the lowest values of $\mathcal{C}$ are associated with growth patterns that are two dimensional, then we should stress that standard ways of estimating the dimension of these clusters, especially for the lowest value of $\mathcal{C}$, may fail to discover this fact. For example, we can compute $F_1^{(n)}$ and then, using Eq. (13), attempt to extract the dimension from log-log plots or $F_1^{(n)}$ against S. This method works very well for the fractal case, but it does not appear to do so well for the cases at hand. In Fig. 5 we show such log-log plots for all the clusters of Fig. 4. We see that even with 100 000 particles the dimension estimate is way below the suspected $D=2$, except for $\mathcal{C}=0.5$. In fact, any practitioner in the fractal field would be happy to interpret the scaling obtained for $\mathcal{C}=0.01$ as an indication that it is in the same universality class as DLA, with dimension very close to $D=1.71$. While we cannot state confidently that for $\mathcal{C}=0.01$ the growth pattern is two-dimensional, we stress that the dimension estimates obtained from log-log plots can be only taken as lower bounds on the true dimension, and these may not be very sharp.

A possibly better way to measure the dimension would be through the result (33) when it holds. We have very good methods to determine the correlation dimension D_2, going back to the Grassberger-Procaccia algorithm [16]. To this aim we choose randomly $m=100\,000$ points $\{\theta_i\}_{i=1}^m$, and compute their positions on the interface of the cluster $z_i=\Phi^{(n)}(e^{i\theta_i})$. Next we compute the correlation integral

$$C^{(2)}(r)=\sum_{i\neq j}\Theta(|z_i-z_j|-r), \tag{37}$$

where $\Theta(x)$ is the step function, being 1 for $x\leqslant 0$ and 0 for $x>0$. The correlation integral is known to scale according to

$$C^{(2)}(r)\sim r^{D_2}. \tag{38}$$

In Fig. 6 we display this object in a log-log plot as a function of r. All the values of $\mathcal{C}$ agree with a correlation dimension of $D_2=1$, as can be seen from the plots at small scales. For those values of $\mathcal{C}$ for which Eq. (33) is correct this leads to the aforementioned result $D=2$.

B. The case $\beta=2$ and $\mathcal{C}>0$

The next interesting family of growth patterns that we focus on is obtained for $\beta=2$ and $\mathcal{C}>0$, with Laplacian growth expected to be realized for $\mathcal{C}=1$. We find that for $\beta>0$ the numerics do not support the scaling relation (23). In Figs. 7 and 8 we show the layer and harmonic averages for $\beta=2$, and it is obvious that in this case

$$\overline{\lambda_n^q}\leqslant\langle\lambda_n^q\rangle \tag{39}$$

in the scaling sense.

Once we have lost the scaling relation (23) we cannot argue that $D=2$ for any value of $\mathcal{C}>0$. We will find numerically that along the line $\beta=2$ we indeed find fractal patterns, (and cf. the following section); nevertheless, even along this line there exists a transition to two-dimensional patterns, albeit at a finite and rather high value of $\mathcal{C}$. Next we want to estimate this value.

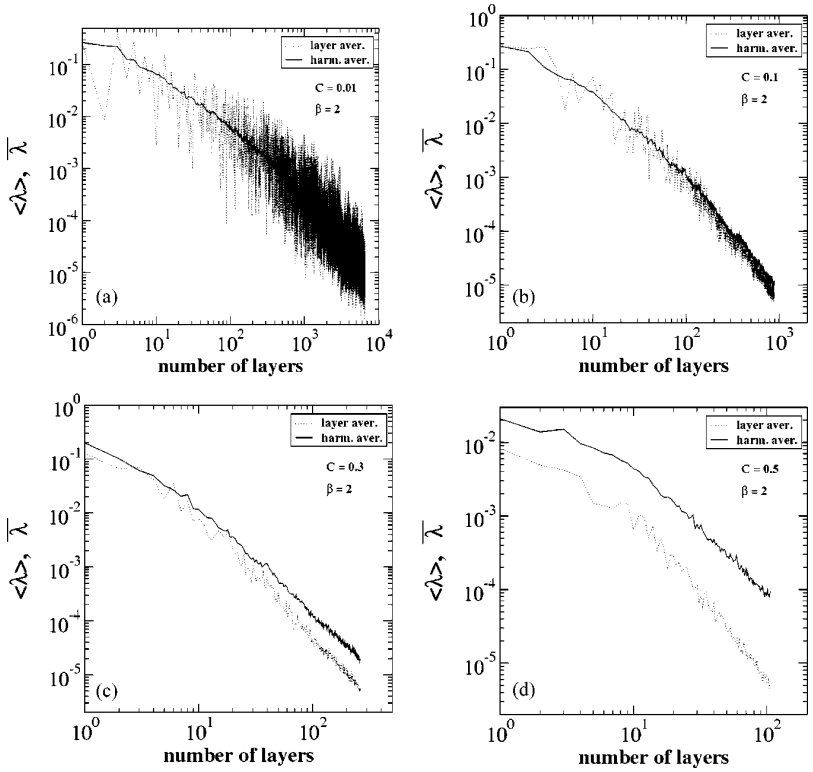

FIG. 7. Layer and harmonic averages of λ_n as a function of the number of layers, for $\beta=2$. Panels (a)–(d), $C=0.01$, 0.1, 0.3, and 0.5, respectively.

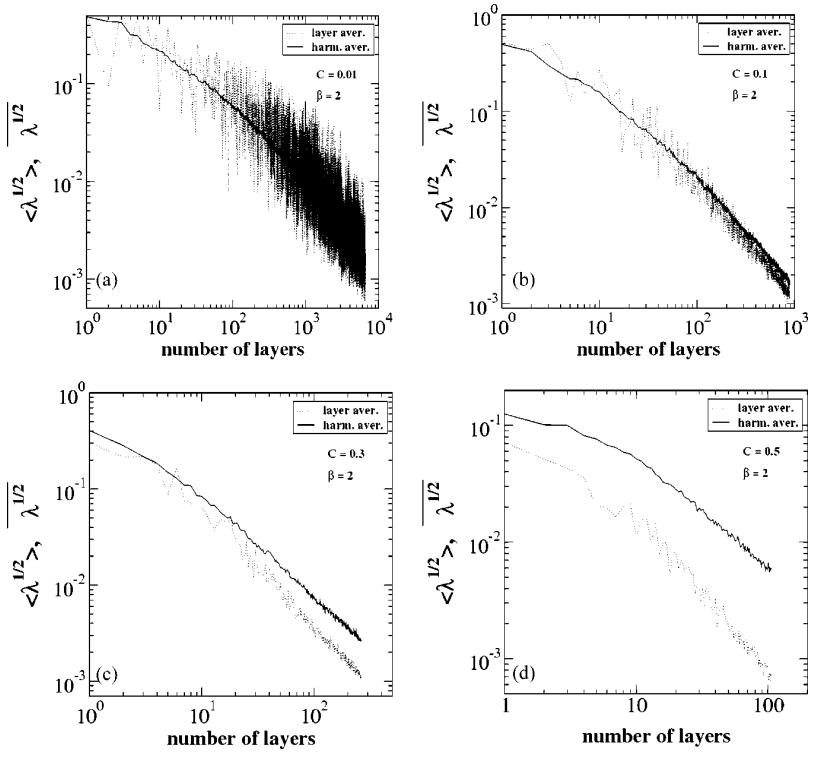

FIG. 8. Layer and harmonic averages of $\lambda_n^{0.5}$ as a function of the number of layers, for $\beta=2$. Panels (a)–(d), $C=0.01$, 0.1, 0.3, and 0.5, respectively.

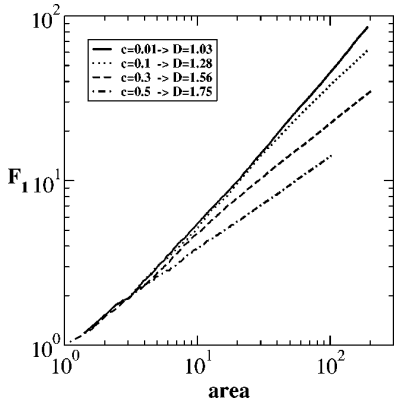

FIG. 9. The first Laurent coefficient $F_1^{(n)}$ as a function of the area for $\beta=2$ and $\mathcal{C}=0.01$, 0.1, 0.3, and 0.5. The fractal dimension D is obtained for the slope via $F_1^{(n)}\sim\sqrt{\tilde{\lambda}_0}(S/\tilde{\lambda}_0)^{1/D}$.

V. CONJECTURE: LAPLACIAN GROWTH IS TWO-DIMENSIONAL

In this section we motivate our conjecture that Laplacian growth patterns are not fractal patterns at all, but rather patterns of dimension 2. We have to be a bit circumvent, since as explained in Ref. [2], we cannot directly run our algorithm for the β-$\mathcal{C}$ model for values of $\mathcal{C}$ higher than about 0.65. The reason is that it becomes impossible to fill up, by random selection of points on the unit circle, a full layer of bumps on the physical interface. Therefore our aim is to find a line in the β-$\mathcal{C}$ phase diagram that separates fractal $D<2$ from two-dimensional growth patterns. That such a line must exist we can convince ourselves by examining the family of growth models that are seen for $\beta=-1$, see Fig. 10. Obviously these are two dimensional. The family of growth patterns obtained for $\beta=0$ were shown in Fig. 4, and as we said above, there must be a cross over two-dimensional patterns in this family. Going up to $\beta=1$ we show the growth patterns in Fig. 11. In this case the images indicate that for the lower values of $\mathcal{C}$ the growth patterns are fractal, whereas for higher values of $\mathcal{C}$ they become two dimensional. Thus the line of separation that we seek in the β-$\mathcal{C}$ phase diagram appears to cut the $\beta=1$ line. Finally, in Fig. 12 we present the family of growth patterns obtained for $\beta=2$. It appears that the transition line intersects also the $\beta=2$ line.

All the patterns exhibited in Figs. 4, 10–12 are grown with a fixed size λ_0. Consequently, for $\beta>0$ the actual mean size of the bumps in the physical space decreases as the cluster grows, while it increases for $\beta<0$. This may lead to worries, i.e., that for $\beta>0$ the growth arrests and that for $\beta<0$ the increase in the size of the bumps leads to coverage of fjords, such that the two-dimensional patterns shown in Fig. 10 would be an artifact. To disperse these worries we have considered alternative growth algorithms with varying the size of λ_0. The first such algorithm is obtained by requiring that the total area covered in each layer of growth is constant, i.e.,

$$\sum_{k=1}^{p}\lambda_{n+k}|\Phi'^{(n+k)}(e^{i\theta_{n+k}})|^2 = \lambda_0(n)\sum_{k=1}^{p}|\Phi'^{(n)}(e^{i\tilde{\theta}_{n+k}})|^{-\beta}=\text{const.} \quad (40)$$

Note that for constant coverage $\mathcal{C}$ this rule coincides with fixed values of λ_0 for $\beta=2$ [cf. Eq. (11)]. In the second

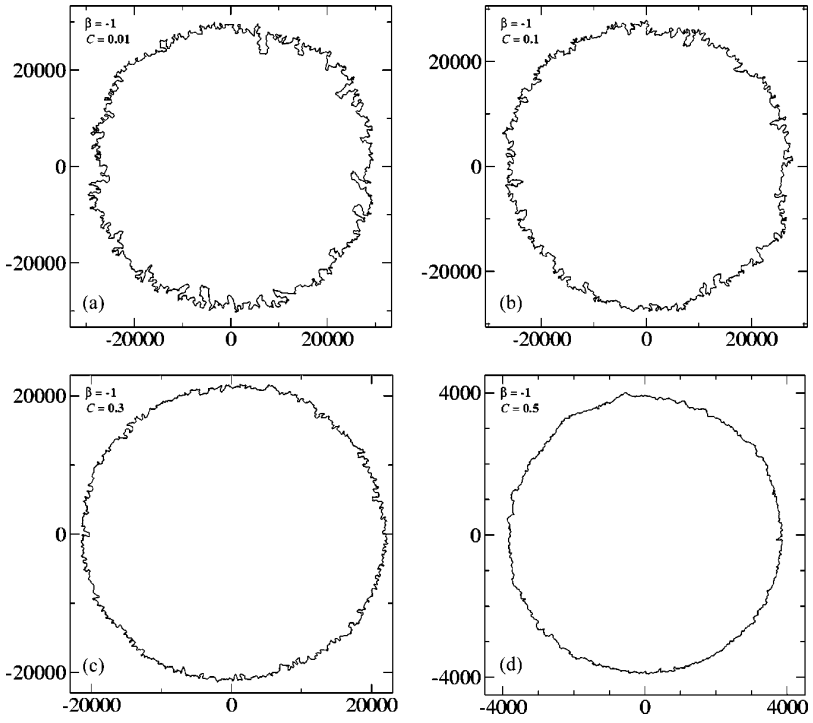

FIG. 10. Growth patterns for $\beta=-1$. Panels (a)–(d), $\mathcal{C}=0.01$, 0.1, 0.3, and 0.5, respectively.

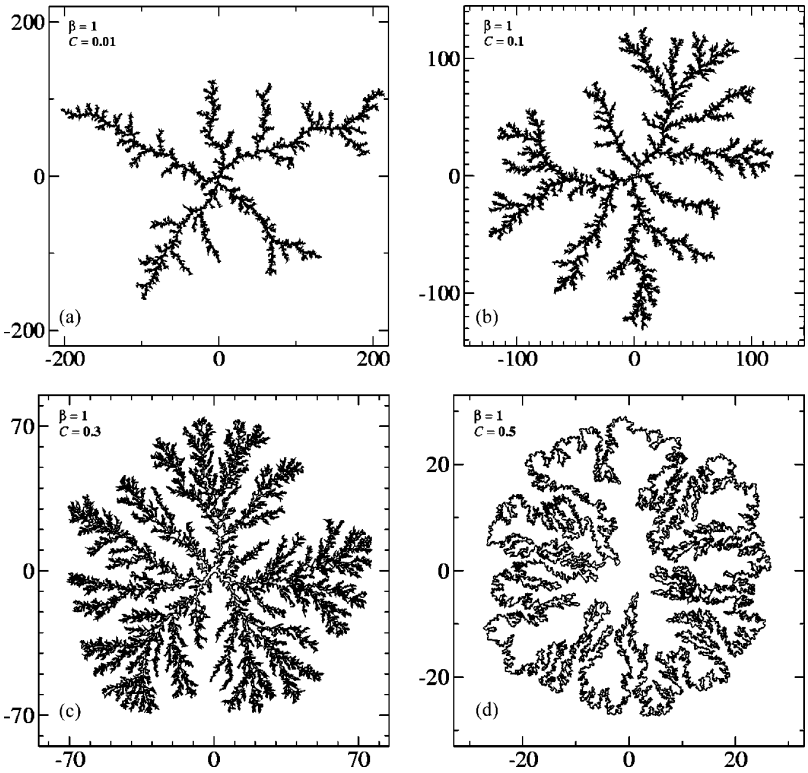

FIG. 11. Growth patterns for $\beta=1$. Panels (a)–(d), $C=0.01$, 0.1, 0.3, and 0.5, respectively.

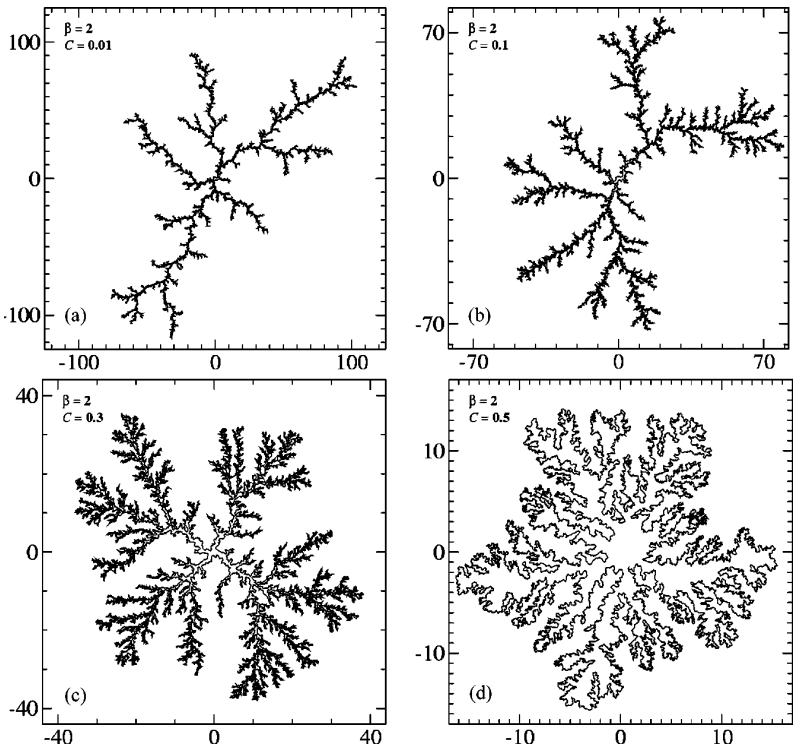

FIG. 12. Growth patterns for $\beta=2$. Panels (a)–(d), $C=0.01$, 0.1, 0.3, and 0.5, respectively.

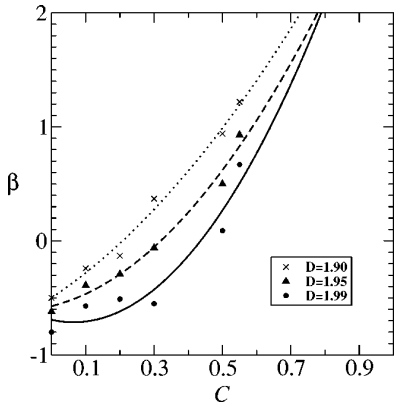

FIG. 13. The phase diagram in the β-$\mathcal{C}$ plane. The data points in crosses, triangles, and circles represent values of β and $\mathcal{C}$ for which the radius-area relationship predicts $D=1.90$, $D=1.95$, and $D=1.99$, respectively. The lines are quadratic fits. We propose that the region below the lines represents two-dimensional growth patterns, see text for details.

algorithm we choose the maximal size of the bump in the physical plane to be constant from layer to layer,

$$\lambda_0(n)\max_{k=1}^{p}\{|\Phi'^{(n)}(e^{i\theta_{n+k}})|^{-\beta}\}=\text{const.} \tag{41}$$

This rule coincides with fixed values of λ_0 for $\beta=0$. We found that in all cases the patterns shown above remain invariant to the change of the algorithms. Thus we submit that the figures shown can be fully trusted.

To find the line that separates fractal from two-dimensional patterns we estimate the dimensions directly from log-log plots of $F^{(n)}$ vs S. We have seen above that such estimates are *lower* bounds to the actual asymptotic dimension. As these logarithmic plots are invariably concave, we can use the slope at the largest values of area available as a measure for the lower bound on the dimension (see, e.g., Fig. 9). In Fig. 13 we show the three lines obtained by searching, for a given value of $\mathcal{C}$, the value of β for which for the first time the dimension estimated from $F^{(n)}$ vs S crosses the value $D=1.90$ (upper curve), $D=1.95$ (middle line), and $D=1.99$ (lower curve). We propose that the last two lines may very well be already beyond the true line that separates fractal from $D=2$ asymptotic dimension. From the discussion of Sec. IV A we cannot even exclude the possibility that the transition line obfuscates the $\beta=0$ line. All the region below the lower line is almost surely representing patterns of $D=2$, but we strongly believe that this is the case also for the middle line. The lines were obtained by finding, as explained, the values of β yielding $D=1.90$, 1.95, and 1.99, respectively, and then fitting to the points a quadratic function. Next we extrapolated the three fits to values of $\mathcal{C}$ that are not readily available in our algorithm. The three fit lines intersect the $\beta=2$ line at $\mathcal{C}=0.73$, 0.78, and 0.79, respectively. We thus propose that the value $\mathcal{C}=1$ for $\beta=2$ is comfortably within the region of two-dimensional patterns in this phase diagram.

VI. CONCLUSIONS

We have presented a careful numerical study of a two-parameter model of growth patterns that generalizes and interpolates between diffusion-limited aggregation and Laplacian growth patterns. The model gives rise to a rich plethora of growth patterns, with fractal dimensions that depend on the values of the parameters β and $\mathcal{C}$. For $\beta=0$ and $\mathcal{C}=0$ we obtain DLA. Laplacian growth patterns have $\beta=2$ and $\mathcal{C}=1$, but we cannot probe the value $\mathcal{C}=1$ within our algorithm. Since our aim, in part, is to demonstrate that Laplacian growth patterns are not fractal, we resorted to examining the phase diagram β-$\mathcal{C}$. We established, on the basis of scaling arguments, simulations, and visual observations that this phase diagram contains a line of transition between fractal and two-dimensional growth patterns. We have estimated the position of this line, and demonstrated that Laplacian growth patterns belong safely in the region of two-dimensional growth patterns.

One should point out that the statement that Laplacian growth are two-dimensional does not mean that it is a growing disk. To the eye the patterns can look fractal, and in fact radius-area log-log plots might initially even indicate that the dimension is low, and may be of the order of the dimension of DLA. Deep fjords may exist in the structure. The relevant question is whether the growing branches of the structure contain substance (area) and whether this area is growing relatively with the growth of the pattern. The growth pattern shown in Fig. 11(d) is a case in point. It looks fractal to the naked eye, but careful examination shows that the branches have area. Thus one needs to decide whether this area is due to some ultraviolet cutoff length, or does it grow systematically beyond what is expected on the basis of the existence of such a cutoff.

Before closing we reiterate that our demonstration that Laplacian growth patterns are two-dimensional is not direct. We cannot, within our algorithm, grow $\mathcal{C}=1$ patterns. We therefore leave this at the moment as a conjecture. It remains a theoretical challenge to show that this conjecture is indeed provable by direct mathematical analysis. We also leave for future work the question whether the $\beta=0$ line represents two-dimensional growth patterns for all $\mathcal{C}>0$. Finally, we propose that future work may make use of the fractal patterns along the line $\mathcal{C}=0$, $\beta>0$ for further fundamental studies of DLA and related phenomena.

ACKNOWLEDGMENTS

We thank Benny Davidovitch for a critical reading of the manuscript, and for a number of useful comments. This work has been supported in part by the European Commission under the TMR program, The Petroleum Research Fund, and the Naftali and Anna Backenroth-Bronicki Fund for Research in Chaos and Complexity. A.L. thanks the Minerva Foundation, Munich, Germany for financial support.

[1] F. Barra, B. Davidovitch, A. Leverman, and I. Procaccia, Phys. Rev. Lett. **87**, 134501 (2001).
[2] F. Barra, B. Davidovitch, and I. Procaccia, Phys. Rev. E **65**, 045101 (2002).
[3] T. A. Witten and L. M. Sander, Phys. Rev. Lett. **47**, 1400 (1981).
[4] P. G. Saffman and G. I. Taylor, Proc. R. Soc. London, Ser. A **245**, 312 (1958).
[5] B. Shraiman and D. Bensimon, Phys. Rev. A **30**, 2840 (1984); S. D. Howison, J. Fluid Mech. **167**, 439 (1986).
[6] B. Davidovitch, A. Levermann, and I. Procaccia, Phys. Rev. E **62**, R5919 (2000).
[7] D. Bensimon, L. P. Kadanoff, S. Liang, B. I. Shraiman, and C. Tang, Rev. Mod. Phys. **58**, 977 (1986); S. Tanveer, Philos. Trans. R. Soc. London, Ser. A **343**, 155 (1993), and references therein.
[8] L. Paterson, Phys. Rev. Lett. **52**, 1621 (1984); L. M. Sander, Nature (London) **322**, 789 (1986); J. Nittmann and H. E. Stanley, *ibid.* **321**, 663 (1986); H. E. Stanley, in *Fractals and Disordered Systems*, edited by A. Bunde and S. Havlin (Springer-Verlag, Berlin, 1991).
[9] M. B. Hastings and L. S. Levitov, Physica D **116**, 244 (1998).
[10] B. Davidovitch, H. G. E. Hentschel, Z. Olami, I. Procaccia, L. M. Sander, and E. Somfai, Phys. Rev. E **59**, 1368 (1999).
[11] M. G. Stepanov and L. S. Levitov, e-print cond-mat/0005456.
[12] H. G. E. Hentschel and I. Procaccia, Physica D **8**, 435 (1983).
[13] T. C. Halsey, P. Meakin, and I. Procaccia, Phys. Rev. Lett. **56**, 854 (1986).
[14] T. C. Halsey, M. H. Jensen, I. Procaccia, L. P. Kadanoff, and B. I. Shraiman, Phys. Rev. A **33**, 1141 (1986).
[15] T. C. Halsey, Phys. Rev. Lett. **72**, 1228 (1994).
[16] P. Grassberger and I. Procaccia, Phys. Rev. Lett. **50**, 346 (1983).

4 Quasi-static fracture propagation

4.1 Quasi-static fractures of mode III

Physical Review E

(Rapid Communication)

Volume **65** (2002)

page R045101

RAPID COMMUNICATIONS

PHYSICAL REVIEW E, VOLUME 65, 045101(R)

Quasistatic fractures in brittle media and iterated conformal maps

Felipe Barra, H. George E. Hentschel,* Anders Levermann, and Itamar Procaccia
Department of Chemical Physics, The Weizmann Institute of Science, Rehovot, 76100, Israel
(Received 4 October 2001; published 25 March 2002)

We study the geometrical characteristic of quasistatic fractures in brittle media, using iterated conformal maps to determine the evolution of the fracture pattern. This method allows an efficient and accurate solution of the Lamé equations without resorting to lattice models. Typical fracture patterns exhibit increased ramification due to the increase of the stress at the tips. We find the roughness exponent of the experimentally relevant backbone of the fracture pattern, it crosses over from about 0.5 for small scales to about 0.75 for large scales. We propose that this crossover reflects the increased ramification of the fracture pattern.

DOI: 10.1103/PhysRevE.65.045101 PACS number(s): 62.20.Mk

A considerable amount of theoretical work [1–3] on fracture in brittle media is based on attempts to solve the equation of motion for an isotropic elastic body in the continuum limit

$$\rho \frac{\partial^2 \mathbf{u}}{dt^2} = (\lambda + \mu)\nabla(\nabla \cdot \mathbf{u}) + \mu \nabla^2 \mathbf{u}. \tag{1}$$

Here $\mathbf{u}$ is the field describing the displacement of each mass point from its location in an unstrained body and ρ is the density. The constants μ and λ are the Lamé constants. In terms of the displacement field the elastic strain tensor is defined as

$$\epsilon_{ij} \equiv \frac{1}{2}\left(\frac{\partial u_i}{\partial x_j} + \frac{\partial u_j}{\partial x_i} \right). \tag{2}$$

For the development of a crack the important object is the stress tensor, which in linear elasticity is written as

$$\sigma_{ij} \equiv \lambda \delta_{ij} \sum_k \epsilon_{kk} + 2\mu \epsilon_{ij}. \tag{3}$$

When the stress component, which is transverse to the interface of a crack, exceeds a threshold value σ_c, the crack can develop. When the external load is such that the transverse stress exceeds only slightly the threshold value, the crack develops slowly, and one can neglect the second time derivative in Eq. (1). This is the quasistatic limit, in which after each growth event one needs to recalculate the strain field by solving the Lamé equation

$$(\lambda + \mu)\nabla(\nabla \cdot \mathbf{u}) + \mu \nabla^2 \mathbf{u} = 0. \tag{4}$$

In many previous works the problem was approached by discretizing Eqs. (1) and (4) on a lattice [4–7]. In this paper we offer a different approach based on iterated conformal maps, this method turned out to be very useful in the context of fractal growth patterns [8–11] and it appears advantageous also for the present problem.

Although we can develop the approach in the full generality of Eq. (4), for the sake of clarity in this paper we will consider mode III fracturing for which a three-dimensional elastic medium is subjected to a finite shear stress $\sigma_{zy} \to \sigma_\infty$ as $y \to \pm\infty$. Such an applied stress will create a displacement field $u_z(x,y)$, $u_x = 0$, $u_y = 0$ in the medium. Despite the medium being three dimensional, therefore, the calculation of the strain and stress tensors are two dimensional.

We can describe a crack of arbitrary shape by its interface $\mathbf{x}(s)$, where s is the arc length, which is used to parametrize the contour. We wish to develop a quasistatic model [12,13] for the time development of this fracture in which discrete events advance the interface with a normal velocity

$$v_n(s) = \alpha(|\sigma_{zt}(s)| - \sigma_c), \tag{5}$$

if the transverse component of the stress tensor σ_{zt} is greater than a critical yield value σ_c for fracturing, otherwise no fracture propagation occurs. We will use the notation (t,n) to describe, respectively, the transverse and normal directions at any point on the two-dimensional crack interface. Whenever the interface has more than one position s for which $v_n(s)$ does not vanish, we choose the next growth position randomly with a probability proportional to $v_n(s)$ [13,14]. There we extend the crack by a fixed area of the size of the "process zone" (and see below for details). This is similar to diffusion limited aggregation (DLA) in which a particle is grown with a probability proportional to the gradient of the field. One should note that another model could be derived in which all eligible fracture sites are grown simultaneously, growing a whole layer whose local width is $v_n(s)$. This would be more akin to Laplacian growth algorithms, which in general give rise to clusters in a different universality class than DLA [15]. Without much extra work we can introduce other effects of disorder, including quenched disorder in the value of σ_c, and other rules for the normal velocity instead of Eq. (5). Such variants of the model will be presented elsewhere [16].

In mode III fracture $\nabla \cdot \mathbf{u} = 0$, and the Lamé equation reduces to Laplace's equation

$$\partial^2 u_z / \partial x^2 + \partial^2 u_z / \partial y^2 = 0, \tag{6}$$

and, therefore, u_z is the real part of an analytic function

*Also at Department of Physics, Emory University, Atlanta, GA.

 ©2002 The American Physical Society

RAPID COMMUNICATIONS

$$\chi(z)=u_z(x,y)+i\xi_z(x,y), \tag{7}$$

where $z=x+iy$. The boundary conditions far from the crack and on the crack interface can be used to find this analytic function. It should be stated here that mode I and mode II fractures can be reduced to a bi-Laplacian equation, then one needs to determine *two* rather than one analytic functions. How to accomplish a growth model using iterated conformal maps for those cases will be shown in a forthcoming publication [16].

Far from the crack as $y\to\pm\infty$ we know $\sigma_{zy}\to\sigma_\infty$ or using the stress/strain relationships Eq. (3) we find that $u_z \approx[\sigma_\infty/\mu]y$. Thus, the analytic function must have the form [17]

$$\chi(z)\to -i[\sigma_\infty/\mu]z \quad \text{as} \quad |z|\to\infty. \tag{8}$$

Now on the boundary of the crack the normal stress vanishes, i.e.,

$$0=\sigma_{zn}(s)=\partial_n u_z=-\partial_t\xi_z. \tag{9}$$

Since ξ_z is constant on the boundary, we choose $\xi_z=0$, which in turn is a boundary condition making the analytic function $\chi(z)$ real on the boundary of the crack,

$$\chi(z(s))=\chi(z(s))^*. \tag{10}$$

The direct determination of the strain tensor for an arbitrary shaped (and evolving) crack is still difficult. We, therefore, proceed by turning to a mathematical complex plane ω, in which the crack is forever circular and of unit radius. The strain field for such a crack is well known, being the real part of the function $\chi^{(0)}(\omega)$ where

$$\chi^{(0)}(\omega)=-i[\sigma_\infty/\mu](\omega-1/\omega). \tag{11}$$

This is the unique analytic function obeying the boundary conditions $\chi^{(0)}(\omega)\to -i[\sigma_\infty/\mu]\omega$ as $|\omega|\to\infty$, while on the unit circle $\chi^{(0)}(\exp(i\theta))=\chi^{(0)}(\exp(i\theta))^*$.

Now invoke a conformal map $z=\Phi^{(n)}(\omega)$ that maps the exterior of unit circle in the mathematical plane ω to the exterior of the crack in the physical plane z, after n growth steps. This conformal map is univalent by construction, and, therefore, admits a Laurent expansion

$$\Phi^{(n)}(\omega)=F_1^{(n)}\omega+F_0^{(n)}+F_{-1}^{(n)}/\omega+F_{-2}^{(n)}/\omega^2+\cdots. \tag{12}$$

Then the required analytic function $\chi^{(n)}(z)$ is given by the expression

$$\chi^{(n)}(z)=-i[F_1^{(n)}\sigma_\infty/\mu][\Phi^{(n)-1}(z)-1/\Phi^{(n)-1}(z)]. \tag{13}$$

From this we should compute now the transverse stress tensor,

$$\begin{aligned}\sigma_{zt}(s)=\mu\partial_t u_z=\mu\,\mathrm{Re}\frac{\partial\chi^{(n)}(z)}{\partial s}&=\mu\,\mathrm{Re}\left[\frac{\partial\chi^{(n)}(\Phi^{(n)}(e^{i\theta}))}{\partial\theta}\frac{\partial\theta}{\partial s}\right]\\&=-\mathrm{Re}\left[\frac{iF_1^{(n)}\sigma_\infty\dfrac{\partial}{\partial\theta}(e^{i\theta}-e^{-i\theta})}{|\Phi'^{(n)}(e^{i\theta})|}\right]\\&=2\sigma_\infty F_1^{(n)}\frac{\cos\theta}{|\Phi'^{(n)}(e^{i\theta})|},\end{aligned} \tag{14}$$

on the boundary.

Finally we describe how $\Phi^{(n)}(\omega)$ is obtained. Suppose that $\Phi^{(n-1)}(\omega)$ is known, with $\Phi^{(0)}(\omega)$ being the identity, $\Phi^{(0)}(\omega)=\omega$. We first compute the transverse strain tensor $\sigma_{zt}(\theta)=2\sigma_\infty F_1^{(n-1)}(\cos\theta)/|\Phi'^{(n-1)}(e^{-i\theta})|$. In order to grow according to the requirement (5), we should choose growth sites more often when $\Delta\sigma(\theta)\equiv\sigma_{zt}(\theta)-\sigma_c$ is larger. We, therefore, construct a probability density $P(\theta)$ on the unit circle $e^{i\theta}$, which satisfies

$$P(\theta)=\frac{|\Phi'^{(n-1)}(e^{i\theta})|\Delta\sigma(\theta)\Theta(\Delta\sigma(\theta))}{\displaystyle\int_0^{2\pi}|\Phi'^{(n-1)}(e^{i\tilde\theta})|\Delta\sigma(\tilde\theta)\Theta(\Delta\sigma(\tilde\theta))d\tilde\theta}, \tag{15}$$

where $\Theta(\Delta\sigma(\tilde\theta))$ is the Heaviside function, and $|\Phi'^{(n-1)}(e^{i\theta})|$ is simply the Jacobian of the transformation from mathematical to physical plane. The next growth position θ_n in the mathematical plane, is chosen randomly with respect to the probability $P(\theta)d\theta$. At the chosen position on the crack, i.e., $z=\Phi^{(n-1)}(e^{i\theta_n})$, we want to advance the crack with a region whose area is the typical process zone for the material that we analyze. According to [4] the typical scale of the process zone is K^2/σ_c^2, where K is a characteristic fracture toughness parameter. Denoting the typical *area* of the process zone by λ_0, we achieve growth with an auxiliary conformal map $\phi_{\lambda_n,\theta_n}(\omega)$ that maps the unit circle to a unit circle with a bump of area λ_n centered at $e^{i\theta_n}$. An example of such a map is given by [8]

$$\begin{aligned}\phi_{\lambda,0}(w)=w\Bigg\{\frac{(1+\lambda)}{2w}(1+w)\Bigg[1+w+w\\\times\left(1+\frac{1}{w^2}-\frac{2}{w}\frac{1-\lambda}{1+\lambda}\right)^{1/2}\Bigg]-1\Bigg\}^a,\end{aligned} \tag{16}$$

$$\phi_{\lambda,\theta}(w)=e^{i\theta}\phi_{\lambda,0}(e^{-i\theta}w). \tag{17}$$

Here the bump has an aspect ratio a, $0\leqslant a\leqslant 1$. In our work below we use $a=2/3$. To ensure a fixed size step in the physical domain we choose

$$\lambda_n=\frac{\lambda_0}{|\Phi^{(n-1)\prime}(e^{i\theta_n})|^2}. \tag{18}$$

Finally the updated conformal map $\Phi^{(n)}$ is obtained as

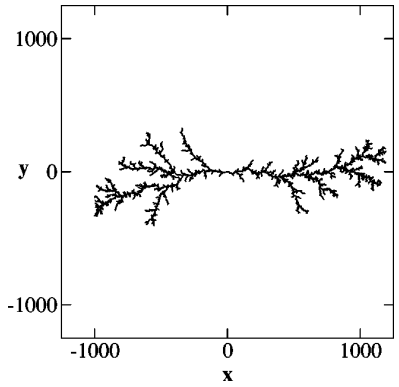

FIG. 1. A typical fracture pattern that is obtained from iterated conformal maps. What is seen is the boundary of the fractured zone, which is the mapping of the unit circle in the mathematical domain onto the physical domain. Notice that the pattern becomes more and more ramified as the the fracture pattern develops. This is due to the enhancement of the stress field at the tips of the growing pattern.

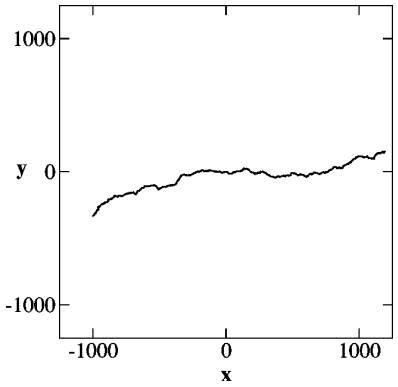

FIG. 2. A typical backbone of the fracture pattern. This is the projection onto the *x*-*y* plane of the experimentally observed boundary between the two parts of the material that separate when the fracture pattern hits the lateral boundaries.

$$\Phi^{(n)}(\omega)=\Phi^{(n-1)}(\phi_{\lambda_n,\theta_n}(\omega)). \tag{19}$$

The recursive dynamics can be represented as iterations of the map $\phi_{\lambda_n,\theta_n}(w)$,

$$\Phi^{(n)}(w)=\phi_{\lambda_1,\theta_1}\circ\phi_{\lambda_2,\theta_2}\circ\cdots\circ\phi_{\lambda_n,\theta_n}(\omega). \tag{20}$$

Every given fracture is determined completely by the random itinerary $\{\theta_i\}_{i=1}^{n}$. Eq. (14) together with Eq. (20) offer an analytic expression for the transverse stress field at any stage of the crack propagation.

Figure 1 exhibits a typical fracture pattern that is obtained with this theory, with $\sigma_\infty=1$, after 10 000 growth events. The threshold value of σ_c for the occurrence of the first event [cf. Eq. (14)] is $\sigma_c=2$. We always implement the first event. For the next growth event the threshold is $\sigma_c=2.9401\ldots$. We, thus, display in Fig. 1 a cluster obtained with $\sigma_c=2.94$, to be as close as possible to the quasistatic limit. Note that here we could opt to represent a disordered material by a random value of σ_c [16]. With fixed σ_c, one should observe that as the pattern develops, the stress at the active zone increases, and we get progressively away from the quasistatic limit. Indeed, as a result of this, for fixed boundary conditions at infinity, there are more and more values of θ for which Eq. (15) does not prohibit growth. Since the tips of the patterns are mapped by $\Phi^{(n)-1}$ to larger and larger arcs on the unit circle, the support of the probability $P(\theta)$ increases, and the fracture pattern becomes more and more ramified as the process advances. The geometric characteristics of the fracture pattern are *not* invariant to the growth. For this reason it makes little sense to measure the fractal dimension of the pattern, this is not a stable characteristic, and it will change with the growth. On the other hand, we should realize that the fracture pattern is not what is observed in typical experiments. When the fracture hits the boundaries of the sample, and the sample breaks into two parts, all the side branches of the pattern remain hidden in the damaged material, and only the backbone of the fracture pattern appears as the surface of the broken parts. The backbone does not suffer from the geometric variability discussed above. In Fig. 2 we show the backbone of the pattern displayed in Fig. 1. This backbone is representative of all the fracture patterns. We should note that in our theory there are no lateral boundaries, and the backbone shown does not suffer from finite size effects that may very well exist in experimental realizations.

In determining the roughness exponent of the backbone, we should note that a close examination of it reveals that *it is not a graph*. There are overhangs in this backbone, and since we deal with mode III fracturing, the two pieces of material *can* separate leaving these overhangs intact. Accordingly, one should not approach the roughness exponent using correlation function techniques, these may introduce serious errors when overhangs exist [18]. Rather, we should measure, for any given r, the quantity [19]

$$h(r)\equiv\langle\max\{y(r')\}_{x<r'<x+r}-\min\{y(r')\}_{x<r'<x+r}\rangle_x. \tag{21}$$

The roughness exponent ζ is then obtained from

$$h(r)\sim r^{\zeta}, \tag{22}$$

if this relation holds. To get good statistics we average, in addition to all x for the same backbone, over many fracture patterns. The result of the analysis is shown in Fig. 3.

We find that the roughness exponent for the backbone exhibits a clear crossover from 0.54 for shorter distances r to 0.75 for larger distances. Within the error bars these results are in a surprising agreement with the numbers quoted experimentally, see, for example, [19]. The short length scale exponent of order 0.5 is also in agreement with recent simulational results of a lattice model [7] (which is by definition a short length scale solution). Bouchaud [19] proposed that the crossover stems from transition between slow and rapid fracture, from the "vicinity of the depinning transition" to the "moving phase" in her terms. Obviously, in our theory we solve the quasistatic equation all along, and there is no change of physics. Nevertheless, as we observed before, the

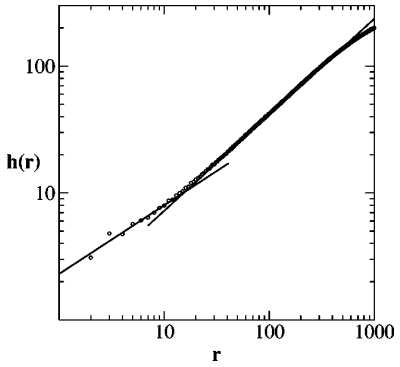

FIG. 3. $h(r)$ averaged over all the backbone and over 70 fracture patterns each of which is 10 000 fracture events. There is a crossover between a scaling law with roughness exponent 0.54 ± 0.05 to and exponent of 0.75 ± 0.02.

fracture pattern begins with very low ramification when the stress field exceeds the threshold value only at few positions on the fracture interface. Later it evolves to a much more ramified pattern due to the increase of the stress fields at the tips of the mature pattern. *The scaling properties of the backbone reflect this crossover*. We propose that this effect is responsible for the crossover in the roughening exponent of the backbone. We are not in a position to claim that the correspondence in roughening exponents indicates that mode III is in the same universality class as the experiment. In fact, the analysis of [20] indicates that mode III is not in the same universality class as mode I and II. It is not impossible however that the mechanism for the crossover in exponents (when it occurs) is similar in all cases.

We have, thus, demonstrated that iterated conformal maps offer an efficient method for studying fracture patterns. Here we considered only mode III quasistatic patterns. The theory for mode I and mode II is available and will be presented elsewhere [16]. The generalization to dynamical scaling, in which Eq. (1) is considered including the time derivatives is akin to the transition from electrostatics to electrodynamics. This is still an attractive goal for the road ahead.

We are indebted to S. Ciliberto for getting us interested in this problem and to J. Fineberg for some very useful discussions. This work had been supported in part by the Petroleum Research Fund, the European Commission under the TMR program, and the Naftali and Anna Backenroth-Bronicki Fund for Research in Chaos and Complexity. A.L. was financially supported by the Minerva Foundation, Munich, Germany.

[1] N.I. Muskhelishvili, *Some Basic Problems in the Mathematical Theory of Elasticity* (Noordhoff, Groningen, 1952).
[2] L.D. Landau and E.M. Lifshitz, *Theory of Elasticity*, 3rd ed. (Pergamon, London, 1986).
[3] J. Fineberg and M. Marder, Phys. Rep. **313**, 1 (1999), and references therein.
[4] H.J. Herrmann and S. Roux, *Statistical Models for the Fracture of Disordered Media* (North-Holland, Amsterdam, 1990), and references therein.
[5] L. Slepian, Dokl. Akad. Nauk. SSSR **258**, 561 (1981) [Sov. Phys. Dokl. **26**, 538 (1981)].
[6] M. Marder and X. Liu, Phys. Rev. Lett. **71**, 2417 (1993).
[7] A. Parisi, G. Caldarelli, and L. Pietronero, e-print arXiv:cond-mat/0004374.
[8] M.B. Hastings and L.S. Levitov, Physica D **116**, 244 (1998).
[9] B. Davidovitch, H.G.E. Hentschel, Z. Olami, I. Procaccia, L.M. Sander, and E. Somfai, Phys. Rev. E **59**, 1368 (1999).
[10] B. Davidovitch, M.J. Feigenbaum, H.G.E. Hentschel, and I. Procaccia, Phys. Rev. E **62**, 1706 (2000).
[11] B. Davidovitch, A. Levermann, and I. Procaccia, Phys. Rev. E **62**, R5919 (2000).
[12] M. Barber, J. Donley, and J.S. Langer, Phys. Rev. A **40**, 366 (1989).
[13] See, for example, J. Kertész in [4].
[14] E. Louis and F. Guinea, Europhys. Lett. **3**, 871 (1987).
[15] F. Barra, B. Davidovitch, and I. Procaccia, e-print cond-mat/0105608; Phys. Rev. E (to be published).
[16] F. Barra, A. Levermann, and I. Procaccia (unpublished).
[17] See, for example, Ref. [3], Sec. 2.3. There is no universal agreement on the experimental velocity law, and other choices can be made here.
[18] Z. Olami, I. Procaccia, and R. Zeitak, Phys. Rev. E **52**, 3402 (1995).
[19] E. Bouchaud, J. Phys.: Condens. Matter **9**, 4319 (1997).
[20] S. Ramanathan, D. Ertaş, and D. S Fisher, Phys. Rev. Lett. **79**, 873 (1997).

4.2 Quasi-static fracture problems: all modes

Physical Review E

Volume **66** (2002)

page 066122

PHYSICAL REVIEW E **66**, 066122 (2002)

Quasistatic brittle fracture in inhomogeneous media and iterated conformal maps: Modes I, II, and III

Felipe Barra,* Anders Levermann, and Itamar Procaccia
Department of Chemical Physics, The Weizmann Institute of Science, Rehovot, 76100, Israel
(Received 7 May 2002; published 18 December 2002)

The method of iterated conformal maps is developed for quasistatic fracture of brittle materials, for all modes of fracture. Previous theory, that was relevant for mode III only, is extended here to modes I and II. The latter require the solution of the bi-Laplace rather than the Laplace equation. For all cases we can consider quenched randomness in the brittle material itself, as well as randomness in the succession of fracture events. While mode III calls for the advance (in time) of one analytic function, modes I and II call for the advance of two analytic functions. This fundamental difference creates different stress distribution around the cracks. As a result the geometric characteristics of the cracks differ, putting mode III in a different class compared to modes I and II.

DOI: 10.1103/PhysRevE.66.066122 PACS number(s): 62.20.Mk

I. INTRODUCTION

The theory of quasistatic fractures in brittle media [1–5] calls for solving different equations depending on the mode of fracture. In this paper we present an approach based on iterated conformal maps which can be adapted to solve all three modes of fracture (known as modes I, II, and III), including the effects of inhomogeneities and randomness of the brittle material itself.

Basically, the theory of fracture in brittle continuous media is based on the equation of motion for an isotropic elastic body in the continuum limit [1]

$$\rho \frac{\partial^2 \mathbf{u}}{dt^2} = (\lambda + \mu)\nabla(\nabla \cdot \mathbf{u}) + \mu \nabla^2 \mathbf{u}. \tag{1}$$

Here $\mathbf{u}$ is the field describing the displacement of each mass point from its location in an unstrained body and ρ is the density. The constants μ and λ are the Lamé constants. In terms of the displacement field the elastic strain tensor is defined as

$$\epsilon_{ij} \equiv \frac{1}{2}\left(\frac{\partial u_i}{\partial x_j} + \frac{\partial u_j}{\partial x_i} \right). \tag{2}$$

For the development of a crack the important object is the stress tensor, which in linear elasticity is written as

$$\sigma_{ij} \equiv \lambda \delta_{ij} \sum_k \epsilon_{kk} + 2\mu \epsilon_{ij}. \tag{3}$$

When the stress component which is tangential to the interface of a crack exceeds a threshold value σ_c, the crack can develop. When the external load is such that the tangential stress exceeds only slightly the threshold value, the crack develops slowly, and one can neglect the second time derivative in Eq. (1). This is the quasistatic limit, in which after each growth event one needs to recalculate the strain field by solving the Lamé equation

$$(\lambda + \mu)\nabla(\nabla \cdot \mathbf{u}) + \mu \nabla^2 \mathbf{u} = 0. \tag{4}$$

The three "pure" modes of fracture that can be considered are determined by the boundary conditions, or load, at infinity. These are

$$\sigma_{xx}(\infty) = 0; \quad \sigma_{yy}(\infty) = \sigma_\infty; \quad \sigma_{xy}(\infty) = 0 \quad \text{(mode I)}, \tag{5}$$

$$\sigma_{xx}(\infty) = 0; \quad \sigma_{yy}(\infty) = 0; \quad \sigma_{xy}(\infty) = \sigma_\infty \quad \text{(mode II)}. \tag{6}$$

We will study the fracture patterns of these two modes in two-dimensional materials. Mode III calls for a third dimension z, since

$$\sigma_{zy}(y \to \pm\infty) = \sigma_\infty \quad \text{(mode III)}. \tag{7}$$

Such an applied stress creates a displacement field $u_z(x,y)$, $u_x = 0$, $u_y = 0$ in the medium. Thus, in spite of the third dimension, the calculation of the strain and stress tensors remain two dimensional. Nevertheless, the equations to be solved in mode III and modes I and II are different. In mode III fracture $\nabla \cdot \mathbf{u} = 0$, and the Lamé equation reduces to Laplace's equation

$$\Delta u_z \equiv \partial^2 u_z / \partial x^2 + \partial^2 u_z / \partial y^2 = 0, \tag{8}$$

and therefore u_z is the real part, Re $\chi(z)$, of an analytic function $\chi(z)$,

$$\chi(z) = u_z(x,y) + i\xi_z(x,y), \tag{9}$$

where $z = x + iy$. The boundary conditions far from the crack and on the crack interface can be used to find this analytic function. On the other hand, for mode I and mode II fractures in plane elasticity one introduces [1] the Airy potential $U(x,y)$ such that

*Present address: Department Fisica, Facultad de Ciencias Fisicas y Matematicas, Universidad de Chile, Casilla 487-3, Santiago, Chile.

 ©2002 The American Physical Society

$$\sigma_{xx}=\frac{\partial^2 U}{\partial y^2};\quad \sigma_{xy}=-\frac{\partial^2 U}{\partial x\partial y};\quad \sigma_{yy}=\frac{\partial^2 U}{\partial x^2}. \tag{10}$$

The Airy potential U solves the bi-Laplacian equation [2]

$$\Delta\Delta U(x,y)=0. \tag{11}$$

The solution of the bi-Laplacian equation can be written in terms of *two* analytic functions $\phi(z)$ and $\eta(z)$ as

$$U(x,y)=\mathrm{Re}[\bar{z}\varphi(z)+\eta(z)]. \tag{12}$$

This difference requires therefore a separate discussion of mode III and modes I and II.

The problem of quasistatic crack propagation is difficult not only because it is hard to solve Eq. (4) for an arbitrarily shaped crack. Another source of difficulty is that the equation does not dictate how to propagate a crack when the stress tensor exceeds the threshold value σ_c. In this paper we consider only two-dimensional, or effectively two-dimensional (i.e, thin slabs) brittle materials in x,y. We can then describe a crack of arbitrary shape by its interface $\vec{x}(s)$, where s is the arc length which is used to parametrize the contour. We will use the notation (t,n) to describe, respectively, the tangential and normal directions at any point on the two-dimensional crack interface. The literature is quite in agreement that the velocity of propagation of the crack has a normal component which is some function of $\sigma_{tt}(s)-\sigma_c$ for mode I and II, and of $|\sigma_{zt}(s)|-\sigma_c$ for mode III. In both cases σ_c is a measure of the strength of the material, and fracture occurs only if the local stress tensor at the boundary of the crack exceeds this quantity (which can also be a random function of position). Although it is plausible that the normal velocity will depend on the excess stress, there is no proof that this is indeed so. Moreover, there is hardly a consensus on what that function the excess stress might be. The simplest choice [6,7] is a linear function,

$$v_n(s)=\alpha\Delta\sigma\equiv\alpha(\sigma_{tt}(s)-\sigma_c(s)),\quad \text{(modes I, II)}, \tag{13}$$

$$v_n(s)=\alpha\Delta\sigma\equiv\alpha(|\sigma_{zt}(s)|-\sigma_c(s)),\quad \text{(mode III)}, \tag{14}$$

when $\Delta\sigma\geqslant 0$, and $v_n(s)=0$ otherwise. Other velocity laws are possible [9]. In our study of mode III fracture we will examine also a quadratic and an exponential velocity law

$$v_n(s)=\alpha(|\sigma_{zt}(s)|-\sigma_c(s))^2\quad \text{(mode III)}, \tag{15}$$

$$v_n(s)=e^{\alpha(|\sigma_{zt}(s)|-\sigma_c(s))}\quad \text{(mode III)}. \tag{16}$$

It is important to study these variants of the velocity law to ascertain the degree of universality of the geometric characteristics of the resulting cracks. One of our results is that these characteristics *may depend* on the velocity law. While this may be a disappointment from the point of view of fundamental physics, it may help to identify the correct physical mechanisms of fractures in different media. The lack of universality is even more obvious when we add quenched noise, or random values of $\sigma_c(s)$. The geometric characteristics of the cracks may depend on the probability distribution of random values of $\sigma_c(s)$. Again this may give a handle on the characterization of inhomogeneous brittle materials.

At any point in time there can be more than one position s on the interface for which $v_n(s)$ does not vanish. We choose the next growth position randomly with a probability proportional to $v_n(s)$ [7,8]. There we extend the crack by a fixed area of the size of the "process zone" (and see below for details). This is similar to diffusion limited aggregation (DLA) in which a particle is grown with a probability proportional to the gradient of the field. One should note that another model could be derived in which all eligible fracture sites are grown simultaneously, growing a whole layer whose local width is $v_n(s)$. This would be more akin to Laplacian growth algorithms, which in general give rise to clusters in a different universality class than DLA [10,11].

In Sec. II we discuss the growth algorithm in terms of iterated conformal maps. In Sec. III this method is applied to mode III quasistatic fracture. A preliminary report of the method for this case was presented in Ref. [12]. In Sec. IV we present new results including the consequences of the different velocity laws (15) and (16), and those of quenched randomness. We discuss the geometric properties of the fracture patterns, including issues of roughening and exponents. We point out that the roughening exponents are not always well defined, since the fracture patterns do not have stationary geometric characteristics. There is an increased tendency for ramification as the fracture develops. This is reflected in an apparent increase in the roughening exponents of the backbone of the pattern. In Sec. V we discuss the theory of modes I and II fracture. Sec. VI presents the results. We will see that the fracture patterns in modes I and II are much less rough than in mode III (for the same velocity law), in agreement with the analysis of Ref. [13]. We will conclude the paper in Sec. VII. The main conclusion is that mode III results in cracks whose geometric characteristics are in a different class than modes I and II. The former creates cracks that exhibit a cross over in the averaged roughening exponent from about 0.5 to a higher scaling exponent on the larger scales. In contrast, modes I and II create cracks that are not rough on the large scales. Quenched randomness may affect the geometry of the cracks as is exemplified and discussed in this paper.

II. THE METHOD OF ITERATED CONFORMAL MAPS FOR FRACTURE

The direct determination of the strain tensor for an arbitrary shaped (and evolving) crack is difficult. We therefore proceed by turning to a mathematical complex plane ω, in which the crack is forever circular and of unit radius. Next invoke a conformal map $z=\Phi^{(n)}(\omega)$ that maps the exterior of the unit circle in the mathematical plane ω to the exterior of the crack in the physical plane z, after n growth steps. The conformal map will be univalent by construction, and we can write its Laurent expansion in the form

$$\Phi^{(n)}(\omega)=F_1^{(n)}\omega+F_0^{(n)}+F_{-1}^{(n)}/\omega+F_{-2}^{(n)}/\omega^2+\cdots. \tag{17}$$

For all modes of fracture we take $\Phi^{(0)}(\omega)=\omega$, and the iterative dynamics calls for the calculation of the tangential

component of the stress tensor on the boundary of the crack. The arclength position s in the physical domain is mapped by the inverse of $\Phi^{(n)}$ onto a position on the unit circle $\omega = \exp(i\theta)$. We will be able to compute the stress tensor on the boundary of the crack in the physical domain by performing the calculation on the unit circle. In other words we will compute $\sigma_{tt}(\theta)$ or $\sigma_{zt}(\theta)$ on the unit circle in the mathematical plane. The actual calculation of this component of the stress tensor differs in modes I, II, and mode III. We perform the calculation iteratively, taking the stress as known for the crack after $n-1$ fracture events.

In order to implement the nth cracking event according to one of the required velocity laws (13)–(16), we should choose potential positions on the interface more often when v_n is larger. Consider for example the linear velocity law (13). We construct a probability density $P(\theta)$ on the unit circle $e^{i\theta}$ which satisfies

$$P(\theta) = \frac{|\Phi'^{(n-1)}(e^{i\theta})|\Delta\sigma(\theta)\Theta(\Delta\sigma(\theta))}{\int_0^{2\pi} |\Phi'^{(n-1)}(e^{i\tilde{\theta}})|\Delta\sigma(\tilde{\theta})\Theta(\Delta\sigma(\tilde{\theta}))d\tilde{\theta}}, \quad (18)$$

where $\Theta(\Delta\sigma(\tilde{\theta}))$ is the Heaviside function, and $|\Phi'^{(n-1)}(e^{i\theta})|$ is simply the Jacobian of the transformation from mathematical to physical plane. The next growth position, θ_n in the mathematical plane, is chosen randomly with respect to the probability $P(\theta)d\theta$. At the chosen position on the crack, i.e. $z=\Phi^{(n-1)}(e^{i\theta_n})$, we want to advance the crack with a region whose area is the typical process zone for the material that we analyze. According to Ref. [3] the typical scale of the process zone is K^2/σ_c^2, where K is a characteristic fracture toughness parameter. Denoting the typical *area* of the process zone by λ_0, we achieve growth with an auxiliary conformal map $\phi_{\lambda_n,\theta_n}(\omega)$ that maps the unit circle to a unit circle with a bump of area λ_n centered at $e^{i\theta_n}$. An example of such a map is given by [14,15]

$$\phi_{\lambda,0}(w) = w^{1-a}\left\{\frac{(1+\lambda)}{2w}(1+w) \times\left[1+w+w\left(1+\frac{1}{w^2}-\frac{2}{w}\frac{1-\lambda}{1+\lambda}\right)^{1/2}\right]-1\right\}^a \quad (19)$$

$$\phi_{\lambda,\theta}(w) = e^{i\theta}\phi_{\lambda,0}(e^{-i\theta}w). \quad (20)$$

Here the bump has an aspect ratio a, $0 \leqslant a \leqslant 1$. In our work below we use $a=1/2$. To ensure a fixed size step in the physical domain we choose

$$\lambda_n = \frac{\lambda_0}{|\Phi^{(n-1)\prime}(e^{i\theta_n})|^2}. \quad (21)$$

Finally the updated conformal map $\Phi^{(n)}$ is obtained as

$$\Phi^{(n)}(\omega) = \Phi^{(n-1)}(\phi_{\lambda_n,\theta_n}(\omega)). \quad (22)$$

The recursive dynamics can be represented as iterations of the map $\phi_{\lambda_n,\theta_n}(w)$,

$$\Phi^{(n)}(w) = \phi_{\lambda_1,\theta_1}\circ\phi_{\lambda_2,\theta_2}\circ\ldots\circ\phi_{\lambda_n,\theta_n}(\omega). \quad (23)$$

Every given fracture pattern is determined completely by the random itinerary $\{\theta_i\}_{i=1}^n$.

We should stress at this point that this method of development of the fracture pattern is not purely based on linear elasticity. Every growth step advances the fractured zone over an area of the order of λ_0. This represents events that occur in the "process zone," in which plastic flows are taking place, and which are not within the realm of elasticity theory, linear or not. We also note that the fracture patterns shown below are the results of this iterated growth process, and the stress field is computed again after each growth step. The deformation due to the stress field is not represented in the patterns, being an effect of second order.

III. MODE III QUASISTATIC FRACTURE

In this section we discuss how to compute the stress tensor when the load is mode III, using the method of iterated conformal maps. The first step is the determination of the boundary conditions that the analytic function (9) needs to satisfy.

A. Boundary conditions in mode III

Far from the crack as $y \to \pm\infty$ we know $\sigma_{zy} \to \sigma_\infty$ or using the stress-strain relationships Eq. (3) we find that $u_z \approx [\sigma_\infty/\mu]y$. Thus the analytic function must have the form

$$\chi(z) \to -i[\sigma_\infty/\mu]z \quad \text{as } |z| \to \infty. \quad (24)$$

Now on the boundary of the crack the normal stress vanishes, i.e.,

$$0 = \sigma_{zn}(s) = \partial_n u_z = -\partial_t \xi_z. \quad (25)$$

This means that ξ_z is constant on the boundary. We choose the gauge $\xi_z = 0$, which in turn is a boundary condition making the analytic function $\chi(z)$ real on the boundary of the crack,

$$\chi(z(s)) = \chi(z(s))^*. \quad (26)$$

B. The stress tensor for mode III

Following the basic strategy we consider now a circular crack in the mathematical domain. The strain field for such a crack is well known [2], being the real part of the function $\chi^{(0)}(\omega)$ where

$$\chi^{(0)}(\omega) = -i[\sigma_\infty/\mu](\omega - 1/\omega). \quad (27)$$

This is the unique analytic function obeying the boundary conditions $\chi^{(0)}(\omega) \to -i[\sigma_\infty/\mu]\omega$ as $|\omega| \to \infty$, while on the unit circle $\chi^{(0)}(\exp(i\theta)) = \chi^{(0)}(\exp(i\theta))^*$. To find the corresponding function in the physical plane is particularly easy for mode III. Since the real part of the function $\chi(z)$ is

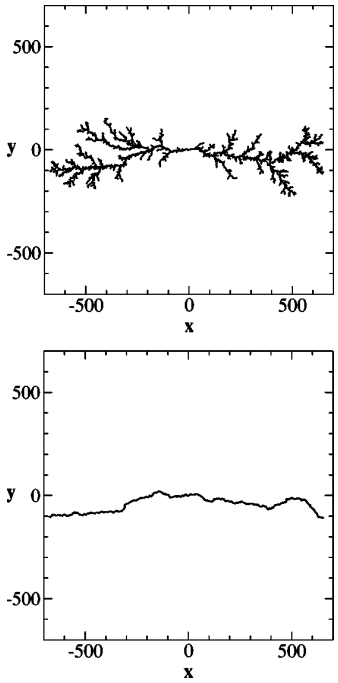

FIG. 1. Upper panel: a typical mode III fracture pattern that is obtained from iterated conformal maps. What is seen is the boundary of the fractured zone, which is the mapping of the unit circle in the mathematical domain onto the physical domain. Notice that the pattern becomes more and more ramified as the the fracture pattern develops. This is due to the enhancement of the stress field at the tips of the growing pattern. Lower panel: the backbone of the fracture pattern. This is the projection onto the x-y plane of the experimentally observed boundary between the two parts of the material that separate when the fracture pattern hits the lateral boundaries.

analytic, it satisfied Laplace's equation automatically. We only need to make sure that it satisfies the boundary conditions. However, if we have a good solution in the mathematical plane, we need just to compose it with an analytic function that takes us from the physical to the mathematical plane. The required analytic function $\chi^{(n)}(z)$ is given by the expression

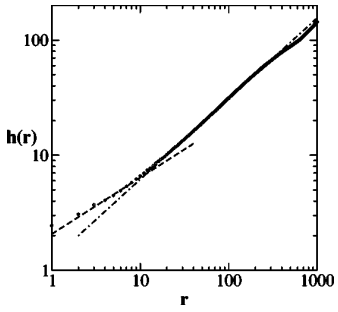

FIG. 2. $h(r)$ averaged over all the backbone and over 20 fracture patterns each of which of 10 000 fracture events. There is a crossover between a scaling law with roughness exponent 0.49 ± 0.08 to an exponent of 0.70 ± 0.05.

$$\chi^{(n)}(z) = -i[F_1^{(n)}\sigma_\infty/\mu][\Phi^{(n)-1}(z) - 1/\Phi^{(n)-1}(z)]. \tag{28}$$

(If $\Phi^{(n)}$ is conformal, $\Phi^{(n)-1}$ is analytic by definition). From this we should compute now the tangential stress tensor,

$$\begin{aligned}\sigma_{zt}(s) &= \mu \partial_t u_z = \mu \,\mathrm{Re}\left[\frac{\partial \chi^{(n)}(z)}{\partial s}\right] \\ &= \mu \,\mathrm{Re}\left[\frac{\partial \chi^{(n)}(\Phi^{(n)}(e^{i\theta}))}{\partial \theta}\,\frac{\partial \theta}{\partial s}\right] \\ &= -\,\mathrm{Re}\frac{iF_1^{(n)}\sigma_\infty \dfrac{\partial}{\partial \theta}(e^{i\theta} - e^{-i\theta})}{|\Phi'^{(n)}(e^{i\theta})|} \\ &= 2\sigma_\infty F_1^{(n)} \frac{\cos\theta}{|\Phi'^{(n)}(e^{i\theta})|},\end{aligned} \tag{29}$$

on the boundary. Eqs. (29) together with Eq. (23) offer an analytic expression for the tangential stress field at any stage of the crack propagation.

IV. RESULTS FOR MODE III

A. Linear velocity law

Figure 1 exhibits in the upper panel a typical fracture pattern that is obtained with this theory, with $\sigma_\infty = 1$, after 10 000 growth events. The threshold value of σ_c for the occurrence of the first event [cf. Eq. (29)] is $\sigma_c = 2$. We always implement the first event. For the next growth event the threshold of σ_c is $2.34315\cdots$. We thus display in Fig. 1 a cluster obtained with $\sigma_c = 2.00$, to be close to the quasistatic limit. Note that here we could opt to represent a disordered material by a random value of σ_c, and see Sec. IV C. With fixed σ_c, one should observe that as the pattern develops, the stress at the active zone increases, and we get progressively away from the quasistatic limit. One could perform a different calculation, relaxing the stress at infinity such as to keep the growth close to threshold. But with fixed boundary conditions at infinity, there are more and more values of θ for which Eq. (18) does not prohibit growth. Since the tips of the patterns are mapped by $\Phi^{(n)-1}$ to larger and larger arcs on the unit circle, the support of the probability $P(\theta)$ increases, and the fracture pattern becomes more and more ramified as the process advances. The geometric characteristics of the fracture pattern are *not* invariant to the growth. For this reason it makes little sense to measure the fractal dimension of the pattern; this is not a stable characteristic, and it will change with the growth. On the other hand, we should realize that the fracture pattern is not what is observed in typical experiments. When the fracture hits the boundaries of the sample, and the sample breaks into two parts, all the side-branches of the pattern remain hidden in the damaged material, and only the backbone of the fracture pattern appears as the surface of the broken parts. In the lower panel of Fig. 1 we show the backbone of the pattern displayed in the upper panel.

This backbone is the representative of all the fracture patterns with the linear velocity law. We should note that in our theory there are no lateral boundaries, and the backbone shown does not suffer from finite size effects which may very well exist in experimental realizations.

In determining the roughness exponent of the backbone, we should note that a close examination of it reveals that *it is not a graph*. There are overhangs in this backbone, and since we deal with mode III fracturing, the two pieces of material *can* separate leaving these overhangs intact. Accordingly, one should not approach the roughness exponent using correlation function techniques; these may introduce serious errors when overhangs exist [16]. Rather, we should measure, for any given r, the quantity [17]

$$h(r) \equiv \langle \max\{y(r')\}_{x<r'<x+r} - \min\{y(r'\}_{x<r'<x+r} \rangle_x . \tag{30}$$

The roughness exponent ζ is then obtained from

$$h(r) \sim r^{\zeta}, \tag{31}$$

if this relation holds. To get good statistics we average, in addition to all x for the same backbone, over many fracture patterns. The result of the analysis is shown in Fig. 2.

We find that the roughness exponent for the backbone exhibits a clear crossover from about 0.5 for shorter distances r to about 0.70 for larger distances. Within the error bars these results are in a surprising agreement with the numbers quoted experimentally, see for example, Ref. [17]. The short length scale exponent of order 0.5 is also in agreement with recent simulational results of a lattice model [18] (which is by definition a short length scale solution). Bouchaud [17] proposed that the crossover stems from transition between slow and rapid fracture, from the "vicinity of the depinning transition" to the "moving phase" in her terms. Obviously, in our theory we solve the quasistatic equation all along, and there is no change of physics. In addition, there is no reason to expect the experiment to be a pure mode III, and as we will see below modes I and II do not show similar roughening. Nevertheless, as we observed before, the fracture pattern begins with very low ramification when the stress field exceeds the threshold value only at few positions on the fracture interface. Later it evolves to a much more ramified pattern due to the increase of the stress fields

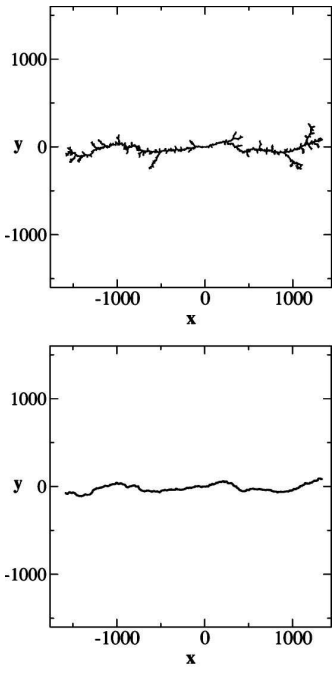

FIG. 3. Upper panel: fracture pattern for mode III fracture with the quadratic law (15), with 10 000 fracture events. Lower panel: the backbone of the pattern.

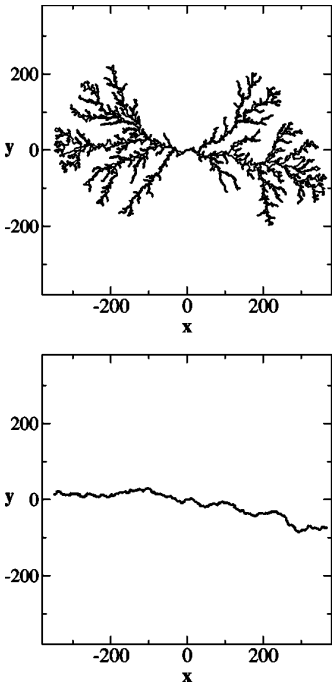

FIG. 4. Upper panel: fracture pattern for mode III fracture with the exponential law (16), with $\alpha = 0.1$, with 10 000 fracture events. Lower panel: the backbone of the pattern.

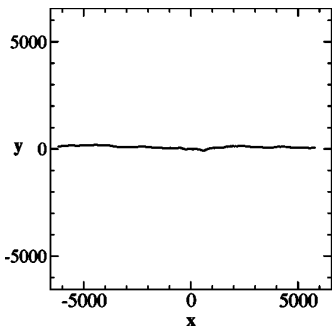

FIG. 5. Fracture pattern for mode III fracture with the exponential law (16), with $\alpha = 1$, with 10 000 fracture events. In this case the fracture pattern and the backbone are the same.

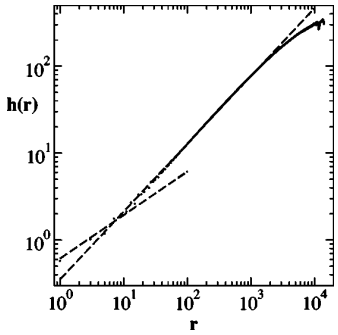

FIG. 6. $h(r)$ averaged over 20 fracture patterns with the exponential velocity law with $\alpha=1$. Each of the patterns consists of 10 000 fracture events. There is a cross over between a scaling law with roughness exponent of about 0.50 at short length scales to an apparent scaling exponent of about 0.78.

at the tips of the mature pattern. *The scaling properties of the backbone reflect this crossover*. We propose that this effect is responsible for the crossover in the roughening exponent of the backbone. On the other hand, this nonstationarity in the geometric characteristics should be handled with care, since it may mean that there is no definite roughening exponent, as it may depend on *where* the analysis is done, near the center of the fracture patterns or near the edge. We will return to this delicate issue after reviewing the results of other velocity laws.

B. Other velocity laws

It should be stressed that there is no reason to believe that the scaling exponents are invariant to the change of the velocity law. In Figs. 3, 4, and 5 we show the fracture patterns and their corresponding backbones for the quadratic velocity law (15) and for two different exponential laws (16). We find that the quadratic law makes little difference with respect to the linear law. The roughening plot is similar, and the scaling exponents appear the same. The exponential velocity law

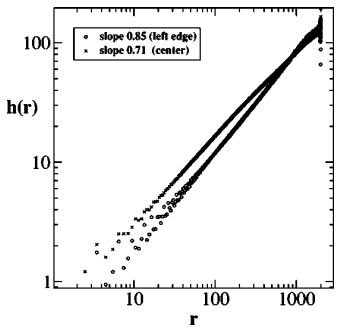

FIG. 7. $h(r)$ averaged over 20 fracture patterns with the exponential velocity law with $\alpha=1$. In this calculation we concentrate on parts of the pattern shown in Fig. 5, one near the center and the other near the edge, each consisting of $r=2000$. The apparent exponents differ, being 0.71 at the center and 0.85 near the edge. The average behavior with exponent 0.78 seen in Fig. 6 should therefore be interpreted with extra care.

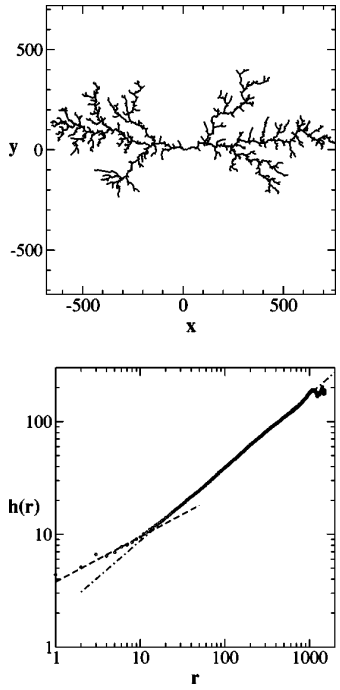

FIG. 8. Upper panel: fracture pattern for mode III fracture with the linear velocity law and quenched randomness with a flat distribution, $\sigma_{max}=15$, with 10 000 fracture events. Lower panel: the function $h(r)$ after averaging over 20 patterns. The scaling exponents are about 0.4 and 0.65 for the smaller and larger scales, respectively.

changes the degree of ramification, and therefore calls for a careful discussion of the roughening plots. Examine the function $h(r)$ for the pattern in Fig. (5) (see Fig. 6). While the small scale roughening exponent of about 0.5 is reproduced, it appears that the large scale exponent is now higher, about 0.78. The question to be asked therefore is whether the scaling exponent is not invariant to the velocity law. In our opinion this question is ill posed since the scaling exponent itself *depends on where is it measured*. As we said before, the fracture pattern tends to become more ramified as it grows. This is reflected in the roughening properties. To make this point clearer, we have taken the pattern of Fig. 5 as a test case, and computed the apparent scaling exponents for short parts of the fracture pattern, limiting the maximal value of r to 2000. By doing so, we can concentrate on a region near the center of the pattern, and on a region near the edge. The results of this exercise are presented in Fig. 7 What is found is that the apparent scaling exponent depends on the region of measurements. Near the center, where the pattern is less ramified, the exponent is smaller than near the edge where the pattern is more ramified. The average exponent reported in Fig. 6 which is analogous to what is reported in experiments, has therefore a limited value. It may not be interpreted as a "true" scaling exponents. Its value may well depend on the actual length of the pattern that is investigated.

We are therefore not in a position to claim that the correspondence in roughening exponents between the linear law and experiments indicates anything about universality

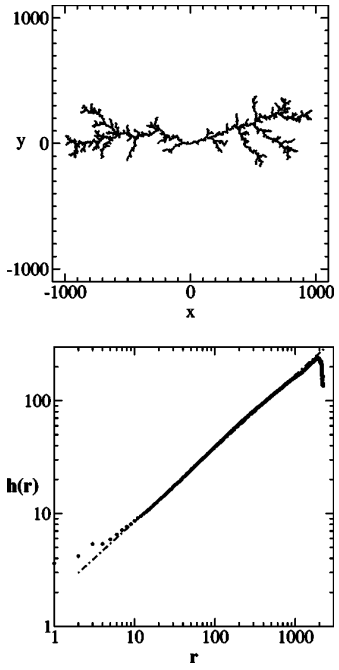

FIG. 9. Upper panel: Fracture pattern for mode III fracture with the linear velocity law and quenched randomness with a power-law distribution, $\beta=2,\sigma_{min}=2$, with 10 000 fracture events. Lower panel: the function $h(r)$ after averaging over 20 patterns. The scaling exponent is about 0.65.

classes. One needs to ascertain very carefully whether measured roughening exponents indicate translationally invariant scaling properties. It is in particular useful to know whether the observed scaling exponents depends on the length of the available fracture pattern.

C. Quenched disorder

To study the effect of quenched randomness we assign *a priori* a random value σ_c to every point in the material (with resolution λ_0). Not having a clear indication from the literature how the randomness of inhomogeneous media should be modeled, we opted for two types of quenched randomness. The first takes the numerical value of $\sigma_c(s)$ from a flat distribution, $0\leqslant\sigma_c\leqslant\sigma_{max}$ and the second takes a power-law form

$$P(\sigma_c)\propto\sigma_c^{-\beta} \quad \text{for} \quad \sigma_c>\sigma_{min}. \tag{32}$$

For reasonable values of σ_{max} the flat distribution did not lead to a qualitative change in the fracture patterns. In Fig. 8 we show the pattern and the function $h(r)$ for the case $\sigma_{max}=15$. The typical crossover that we see in systems without quenched disorder remains here, albeit with apparently smaller exponents, of about 0.4 and 0.65.

On the other hand, a power-law distribution of quenched randomness may lead to very interesting qualitative change in fracture pattern. While high values of β in Eq. (32) are still in qualitative agreement with all previous results (see Fig. 9 with $\beta=2$), lower values of β lead to a new phenomenon. The availability of very high values of σ_c results in effective blocking for the evolution of the fracture. The crack develops along continuous (sometime curved) lines, and then it suddenly gains sharp turns. In Fig. 10 we show the typical patterns obtained for $\beta=1.1$. It is amusing to note that these patterns are reminiscent of what is exhibited in a number of experiments and see, for example, the pictures in Ref. [17]. It is not obvious, however, how to offer quantitative measures for comparison. It appears to the present authors that this subject of fracture with quenched randomness deserves a careful separate study in which experimental and theoretical methods were combined to gain further insights on the questions at hand.

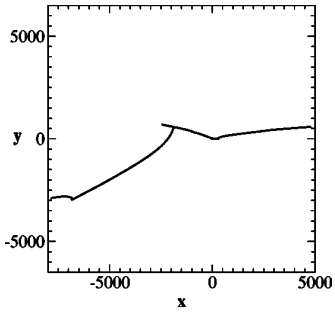

FIG. 10. Fracture pattern for mode III fracture with the linear velocity law and quenched randomness with a power-law distribution, $\beta=1.1,\sigma_{min}=0.2$.

V. THEORY FOR MODES I AND II

In order to compute the stress tensor at the boundary of the crack for modes I and II loading, we turn to the solution of Eq. (11). Since we employ conformal techniques, we are limited to solving Eq. (11) in two-dimensions. Although we realize that three-dimensional solutions may introduce additional physics and quantitative changes [13], we trust that a controlled solutions of Eq. (11) in two-dimensions will shed useful light on the questions of crack geometry, roughening, and scaling.

A. Boundary conditions and removal of freedoms

The boundary conditions at infinity are given by Eqs. (5) and (6). The conditions on the boundary of the crack are

$$\sigma_{xn}(s)=\sigma_{yn}(s)=0 \quad \text{on the boundary.} \tag{33}$$

Using Eq. (10) these boundary condition are rewritten as

$$\partial_t\left[\frac{\partial U}{\partial x}+i\frac{\partial U}{\partial y}\right]=0 \quad \text{on the boundary.} \tag{34}$$

Note that we do not have enough boundary conditions to determine $U(x,y)$ uniquely. In fact we can allow in Eq. (12) arbitrary transformations of the form

$$\varphi\rightarrow\varphi+iCz+\gamma, \tag{35}$$

$$\psi \to \psi + \tilde{\gamma}, \quad \psi \equiv \eta', \tag{36}$$

where C is a real constant and γ and $\tilde{\gamma}$ are complex constants. This provides five degrees of freedom in the definition of the Airy potential. Two of these freedoms are removed by choosing the gauge in Eq. (34) according to

$$\frac{\partial U}{\partial x} + i \frac{\partial U}{\partial y} = 0 \quad \text{on the boundary.} \tag{37}$$

It is important to stress that whatever the choice of the five freedoms the values of the stress tensor are unaffected, and see Ref. [2] for an exhaustive discussion of this point. Computing Eq. (37) in terms of Eq. (12) we arrive at the boundary condition

$$\varphi(z) + z\overline{\varphi'(z)} + \overline{\psi(z)} = 0 \quad \text{on the boundary.} \tag{38}$$

To proceed we represent $\varphi(z)$ and $\psi(z)$ in Laurent form.

$$\varphi(z) = \varphi_1 z + \varphi_0 + \varphi_{-1}/z + \varphi_{-2}/z^2 + \cdots,$$

$$\psi(z) = \psi_1 z + \psi_0 + \psi_{-1}/z + \psi_{-2}/z^2 + \cdots. \tag{39}$$

This form is in agreement with the boundary conditions at infinity that disallow higher-order terms in z. The remaining freedoms are now used to choose $\varphi_0 = 0$ and φ_1 real. Then, using the boundary conditions (5) and (6), we find

$$\varphi_1 = \frac{\sigma_\infty}{4}; \quad \psi_1 = \frac{\sigma_\infty}{2} \quad \text{mode I,}$$

$$\varphi_1 = 0; \quad \psi_1 = i\sigma_\infty \quad \text{mode II.} \tag{40}$$

B. The conformal map and its consequences

The conformal map is identical in form and meaning to the one introduced above and successfully applied to mode III. On the other hand, at present we do not solve the Laplace equation, and our fundamental solution (12) is *not* the real part of an analytic function. We thus cannot simply solve in the mathematical plane and compose with the inverse of the conformal map.

In terms of the conformal map we will write our unknown functions $\varphi(z)$ and $\psi(z)$ as

$$\varphi(z) \equiv \tilde{\varphi}(\Phi^{(n)-1}(z)), \quad \psi(z) \equiv \tilde{\psi}(\Phi^{(n)-1}(z)). \tag{41}$$

Using the Laurent form (17) of the conformal map the linear term at $\omega \to \infty$ is determined by Eqs. (41). We therefore can write

$$\tilde{\varphi}(\omega) = \varphi_1 F_1^{(n)} \omega + \tilde{\varphi}_{-1}/\omega + \tilde{\varphi}_{-2}/\omega^2 + \cdots,$$

$$\tilde{\psi}(\omega) = \psi_1 F_1^{(n)} \omega + \tilde{\psi}_0 + \tilde{\psi}_{-1}/\omega + \tilde{\psi}_{-2}/\omega^2 + \cdots. \tag{42}$$

The boundary condition (38) is now read for the unit circle in the ω plane. Denoting $\epsilon \equiv \exp(i\theta)$ and

$$u(\epsilon) \equiv \sum_{n=1}^{\infty} \tilde{\varphi}_{-n}/\epsilon^n, \quad v(\epsilon) \equiv \sum_{n=0}^{\infty} \tilde{\psi}_{-n}/\epsilon^n, \tag{43}$$

we write

$$u(\epsilon) + \frac{\Phi^{(n)}(\epsilon)}{\overline{\Phi'^{(n)}(\epsilon)}}\,\overline{u'(\epsilon)} + \overline{v(\epsilon)} = f(\epsilon). \tag{44}$$

The function f is a known function that contains all the coefficients that were determined so far,

$$f(\epsilon) = -\varphi_1 F_1^{(n)} \epsilon - \frac{\Phi^{(n)}(\epsilon)}{\overline{\Phi'^{(n)}(\epsilon)}} \varphi_1 F_1^{(n)} - \frac{\overline{\psi_1} F_1^{(n)}}{\epsilon}. \tag{45}$$

C. Solution by power series

To solve the problem we need to compute the coefficients $\tilde{\varphi}_n$ and $\tilde{\psi}_n$. To this aim we first represent

$$\frac{\Phi^{(n)}(\epsilon)}{\overline{\Phi'^{(n)}(\epsilon)}} = \sum_{-\infty}^{\infty} b_i \epsilon^i. \tag{46}$$

The function $f(\sigma)$ has also an expansion of the form

$$f(\epsilon) = \sum_{-\infty}^{\infty} f_i \epsilon^i. \tag{47}$$

In the discussion below we assume that the coefficients b_i and f_i are known. In fact what is computed in our procedure is the conformal map $\Phi^{(n)}(\omega)$. Thus to compute these coefficients we need to Fourier transform the function $\Phi^{(n)}(\epsilon)/\overline{\Phi'^{(n)}(\epsilon)}$. This is the most expensive step in our solution, since the branch cuts that exist in Eq. (19) rule out the use of fast Fourier transforms. One needs to carefully evaluate the Fourier integrals between the branch cuts. The technique how to track the position of the branch cuts on the unit circle was developed in Refs. [10,11]; after having the branch cuts the integrals are evaluated over 1000 equi-distant points between each pair of branch cuts. Using the last two equations together with Eqs. (43) and (44) we get

$$\tilde{\varphi}_{-m} - \sum_{k=1}^{\infty} k\, b_{-m-k-1} \tilde{\varphi}^*_{-k} = f_{-m}, \quad m = 1,2,\ldots, \tag{48}$$

$$\tilde{\psi}^*_{-m} - \sum_{k=1}^{\infty} k\, b_{m-k-1} \tilde{\varphi}^*_{-k} = f_m, \quad m = 0,1,2,\ldots. \tag{49}$$

These sets of linear equations are well posed. The coefficients $\tilde{\varphi}_{-m}$ can be calculated from Eq. (48) alone, and then they can be used to determine the coefficients $\tilde{\psi}_{-m}$. This is in fact proof that Eq. (44) determines the functions u and v together. This fact had been proven with some generality in Ref. [2].

For cracks with simple geometry this is all that we need. For example for a circular crack (a problem that was explic-

itly solved in Ref. [2]) we simply substitute $\Phi^{(n)}(\omega) = \Phi^{(0)}(\omega) = \omega$, and proceed to solve for $\tilde{\varphi}$ and $\tilde{\psi}$, finding finally

$$\tilde{\varphi}(\omega) = \varphi_1 \omega - \frac{\psi_1^*}{\omega}, \quad \tilde{\psi}(\omega) = \psi_1 \omega - 2\frac{\varphi_1}{\omega} - \frac{\psi_1^*}{\omega^3}. \tag{50}$$

For developing cracks of arbitrary shape this is just the starting point. As before in the solution of mode III we need to compute σ_{tt} from which we construct the probability measure for the first fracture event. The development of the $\Phi^{(n)}$ then follows the same lines as before.

To compute σ_{tt} at the boundary of the crack we use the fact that follows directly from the definitions that

$$\sigma_{xx} + \sigma_{yy} = 4\,\mathrm{Re}[\varphi'(z)] = 4\,\mathrm{Re}\left[\frac{\tilde{\varphi}'(\omega)}{\Phi'^{(n)}(\omega)}\right]. \tag{51}$$

Since this is the trace of the stress tensor, which is invariant under smooth coordinate transformation, it is also equal to $\sigma_{nn} + \sigma_{tt}$. Using the fact that σ_{nn} vanishes on the boundary we can write finally

$$\sigma_{tt}(\epsilon) = 4\,\mathrm{Re}\left[\frac{\tilde{\varphi}'(\epsilon)}{\Phi'^{(n)}(\epsilon)}\right]. \tag{52}$$

This result is of some importance; it shows that to compute the component σ_{tt} of the stress tensor *on the boundary* we do not need to compute $\tilde{\psi}(\epsilon)$ at all. Of course, to know the stress tensor anywhere else in the body we need both functions. For the growth algorithm this is not necessary. We note that $\tilde{\varphi}$ is computed from Eqs. (48), and this contains only b_m with negative m. In order to derive a numerical scheme to compute the tangent stress component σ_{tt} on the crack we now truncate the series for $\tilde{\varphi}$ to get an approximation

$$u(\epsilon) \approx \sum_{n=1}^{N} \tilde{\varphi}_{-n} / \epsilon^n. \tag{53}$$

We see from Eq. (48) that if we wish to compute this series up to an order N, we need to compute the coefficients b_{-j} up to $j \leqslant 2N+1$ and then solve the linear system (48). Note that the approximation in Eq. (53) corresponds to a truncation of the series (46) which in turn corresponds to a truncation of the conformal map $\Phi^{(n)}$. Since we are interested in the macroscopic stress distribution along the fracture rather than in the bumpy microstructure, this effect is of no harm as long as we choose N large enough to resolve the desired patterns.

VI. RESULTS FOR MODES I AND II

A. Geometry without quenched disorder

The actual fracture patterns that we find for modes I and II are dramatically different from those found for mode III for the same velocity law. In Fig. 11 we show the fracture patterns for the linear velocity law after about 800 fracture events. First, modes I and II are very similar, except for the obvious 45° tilt in mode II due to the tilt of the symmetry axis of the loading. The highly ramified structure seen in mode III is gone, and the resulting patterns are more akin to the exponential velocity law in mode III, cf. Fig. 5. The roughening plot $h(r)$ (Fig. 12) is also qualitatively different from mode III with the same velocity law. We do not observe a crossover to a higher exponent, indicating that there is no increased roughening at large scales. Indeed, for these modes of fracture the stress field is found to be very highly peaked at the tip of the fracture pattern. Moreover, when there appear deviations towards side branching they are quickly corrected in later growth. To make this point clearer we present in Fig. 13 the stress field at the boundary of the crack in the vicinity of the tip. One can observe that the stress component is such that the slight tilt of the tip will be corrected at the

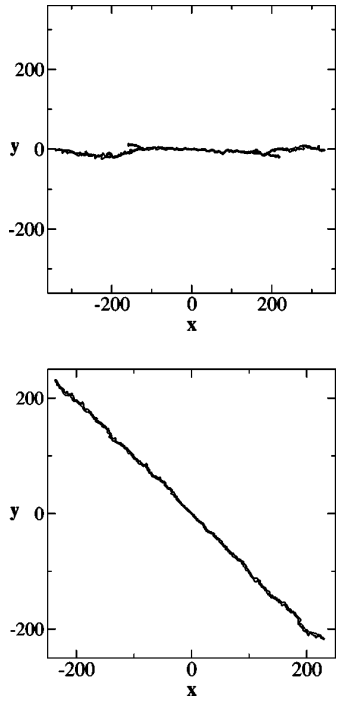

FIG. 11. Upper panel: fracture pattern for mode I with the linear velocity law. Lower panel: fracture pattern for mode II with the linear velocity law.

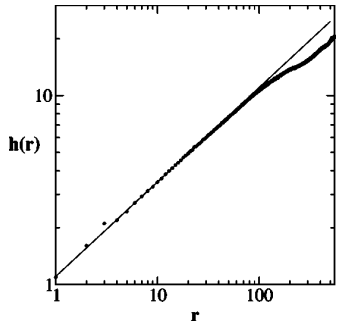

FIG. 12. The function $h(r)$ for mode I fracture, averaged over 11 fracture patterns. The line indicates a slope of 0.5.

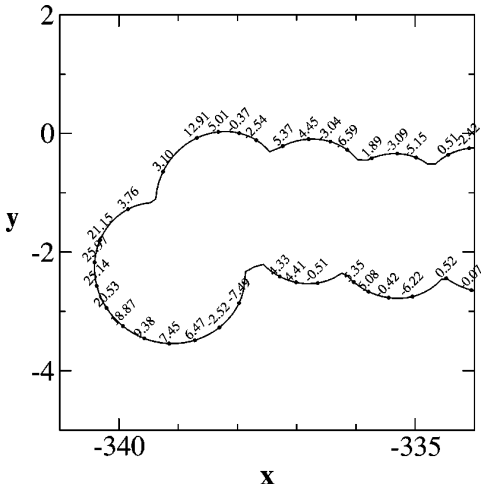

FIG. 13. The stress field at the boundary of the crack in the vicinity of the tip.

next growth event. We therefore do not expect large scale roughening in this mode of fracture.

We should note that similarity in the crack geometries in modes I and II stems from the fact that we distinguish these two modes only by boundary conditions at infinity. Without material anisotropy the crack of mode II chooses an orientation of 45°, rendering the local dynamics at the interface identical to mode I, except for the tilt. At present we do not see how to select boundary conditions that load the crack *locally* in mode II. This phenomenon is related to the so-called ''principle of local symmetry'' [19] that underlines the preference of cracks to maximize their mode I loading at the expense of mode II.

B. The effect of quenched disorder

Last, we present cracks with quenched disorder. First we followed the growth of a crack in mode I, using the same strategy of Sec. IV C. In Fig. 14 we show, for example, the crack obtained with σ_c taken from a flat distribution with $\sigma_{max}=10$. Contrary to the case of mode III the effect of quenched disorder on the roughening is not impressive. The

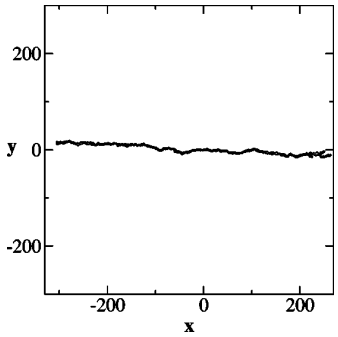

FIG. 14. The fracture pattern in the case of quenched disorder, with σ_c taken from a flat distribution. The pattern is similar to that in Fig. 11, with the same roughening behavior.

roughening exponent is still about 0.5 for small scales, with a failure to roughen on the large scales. This finding remains invariant to change the type of quenched disorder to a power law like Eq. (32). We also do not observe roughening on the large scales when we put quenched disorder, and grow deterministically at the point of highest value of $\sigma_{tt}-\sigma_c$.

VII. CONCLUDING REMARKS

We have presented a solution of the problem quasistatic fracture using the method of iterated conformal map. All modes of fracture can be treated, although mode III is much more straightforward since the equation to be solved is the Laplace equation. The bi-Laplacian equation that is involved in modes I and II requires heavier analysis and more cumbersome numerics. Notwithstanding, we believe that our fracture patterns represent accurate solutions of the problem with the stated laws of evolution.

The geometric characteristics of mode III are different from those of modes I and II. The fracture pattern is very ramified, and if we look at the backbone, (which is what is observed as the boundary between the two parts of the broken material), we find that it is rough on all scales. On smaller scales the roughening exponent is about 0.5, and on larger scales the roughening increases, having an average roughening exponent which depends on the length of the fracture pattern analyzed. The exponent 0.5 is intimately related to the randomness that is introduced by our growth rules. the higher apparent exponents are due to the increased ramification on the larger scales as is explained in Sec. IV. The roughening plots may appear to be in close agreement with some experimental observations, which however are not conducted as mode III. Experimentally one expects that modes I and II are more relevant, but here we do not observe the crossover to roughness characterized by exponents of the order of 0.75. Quite on the opposite, it appears that the roughness saturates, leading to a globally flat fracture patterns on the large scales.

This leaves us with the question of how to interpret the observed roughness in experiments. One possibility is that experiments are not quasistatic, or that in experiments the material has remnant stresses and other sources of quenched disorder. This is the spirit for example of Ref. [20] (and references therein) in which the crossover is tentatively related to damage cavity coalescence. Such possibilities can be put to test. Indeed, we find that mode III is very sensitive to quenched disorder, cf. Sec. IV C. With power-law disorder we can change the geometric characteristic of the fracture patterns altogether. This is not the case, however, with modes I and II, where the priority of the tip in attracting the stress field is overwhelming. These cracks do not appear to roughen on the large scales even with quenched disorder.

In summary, we believe that the experimental observations pose an interesting riddle whose resolution will need a careful assessment of the experimental conditions and their inclusion in the theory. It is our hope that the solution presented above will turn out to be a useful tool in achieving this goal.

ACKNOWLEDGMENTS

We thank Jean-Pierre Eckmann for useful discussions on Fourier transforms in the vicinity of branch cuts. F.B. thanks the ''Fundacion Andes'' and the program ''Inicio de Carrera para Jovenes Cientificos'' (Grant No. C-13760). This work was supported in part by the Petroleum Research Fund, The European Commission under the TMR program and the Naftali and Anna Backenroth-Bronicki Fund for Research in Chaos and Complexity. A.L. was financially supported by the Minerva Foundation, Munich, Germany.

[1] L.D. Landau and E.M. Lifshitz, *Theory of Elasticity*, 3rd ed. (Pergamon, London, 1986).
[2] N.I. Muskhelishvili, *Some Basic Problems in the Mathematical Theory of Elasticity* (Noordhoff, Groningen, 1952).
[3] H.J. Herrmann and S. Roux, *Statistical Models for the Fracture of Disordered Media* (North-Holland, Amsterdam, 1990), and references therein.
[4] J. Fineberg and M. Marder, Phys. Rep. **313**, 1 (1999), and references therein.
[5] L.B. Freund, *Dynamic Fracture Mechanics* (Cambridge University Press, Cambridge, 1998).
[6] M. Barber, J. Donley, and J.S. Langer, Phys. Rev. A **40**, 366 (1989).
[7] See for example, J. Kertész in Ref. [3].
[8] E. Louis and F. Guinea, Europhys. Lett. **3**, 871 (1987).
[9] See, for example, Ref. [4], Sec. II C. There is no universal agreement on the experimental velocity law, and other choices can be made here.
[10] F. Barra, B. Davidovitch, A. Levermann, and I. Procaccia, Phys. Rev. Lett. **87**, 134501 (2001).
[11] F. Barra, B. Davidovitch, and I. Procaccia, Phys. Rev. E (to be published), e-print cond-mat/0105608.
[12] F. Barra, H.G.E. Hentschel, A. Levermann, and I. Procaccia, Phys. Rev. E **65**, R045101 (2002).
[13] S. Ramanathan, D. Ertaş, and D.S Fisher, Phys. Rev. Lett. **79**, 873 (1997).
[14] M.B. Hastings and L.S. Levitov, Physica D **116**, 244 (1998).
[15] B. Davidovitch, H.G.E. Hentschel, Z. Olami, I. Procaccia, L.M. Sander, and E. Somfai, Phys. Rev. E **59**, 1368 (1999).
[16] Z. Olami, I. Procaccia, and R. Zeitak, Phys. Rev. E **52**, 3402 (1995).
[17] E. Bouchaud, J. Phys.: Condens. Matter **9**, 4319 (1997).
[18] A. Parisi, G. Caldarelli, and L. Pietronero, e-print cond-mat/0004374.
[19] B. Cottrell and J.R. Rice, Int. J. Fract. **16**, 155 (1980).
[20] E. Bouchaud, J.P. Bouchaud, D.S. Fisher, S. Ramanathan, and J.R. Rice, J. Mech. Phys. Solids **50**, 1703 (2002).

4.3 Bi-Laplacian growth patterns

Physical Review Letters

Volume **89** (2002)

page 234501

VOLUME 89, NUMBER 23 PHYSICAL REVIEW LETTERS 2 DECEMBER 2002

Bi-Laplacian Growth Patterns in Disordered Media

Anders Levermann and Itamar Procaccia
Department of Chemical Physics, The Weizmann Institute of Science, Rehovot 76100, Israel
(Received 21 August 2002; published 14 November 2002)

Experiments in quasi-two-dimensional geometry (Hele-Shaw cells) in which a fluid is injected into a viscoelastic medium (foam, clay, or associating polymers) show patterns akin to fracture in brittle materials, very different from standard Laplacian growth patterns of viscous fingering. An analytic theory is lacking since a prerequisite to describing the fracture of elastic material is the solution of the bi-Laplace rather than the Laplace equation. In this Letter we close this gap, offering a theory of bi-Laplacian growth patterns based on the method of iterated conformal maps.

DOI: 10.1103/PhysRevLett.89.234501 PACS numbers: 47.54.+r, 47.55.Mh

Pattern formation for two-phase flow instabilities has been intensely studied, both experimentally and theoretically, for the displacement of a viscous fluid from between parallel plates or from a porous medium [1]. In these cases the velocity field $\mathbf{v}(r)$ is well described by Darcy's law $\mathbf{v}(\mathbf{r}) \propto \boldsymbol{\nabla} P(\mathbf{r})$, where $P(\mathbf{r})$ is the pressure. For incompressible fluids $\boldsymbol{\nabla} \cdot \mathbf{v} = 0$, leading to the Laplace equation for the pressure, $\nabla^2 P(\mathbf{r}) = 0$, with appropriate boundary condition on the boundary of the growing pattern and at "infinity." The theory for such "Laplacian growth" patterns in two dimensions [i.e., $\mathbf{r} = (x, y)$] naturally focuses on analytic functions (or their conformal inverse) simply because the Cauchy-Riemann conditions imply that the general solution of the Laplace equation is given by the real part of an analytic function, $P = \mathrm{Re}\{F(z)\}$, where $F(z)$ is the unique analytic function that satisfies the boundary conditions, and $z = x + iy$ [2,3].

Sporadically, over the last decade, there appeared experimental studies in which a low viscosity fluid displaces not a more viscous fluid, but rather a medium which is viscoelastic, like foam [4], clay [5], or a solution of associating polymers [6]. Elastic media are expected to be invaded by fracture, rather than a displacement, and indeed the growth patterns reported in the experiments had features akin to fracture patterns in brittle materials; see Fig. 1. Detailed comparisons with theory were lacking, however, since an appropriate analytic theory did not exist. As is well known (and see below for details), in fracture the relevant equation to solve is the bi-Laplace equation $\nabla^2 \nabla^2 \chi = 0$ with appropriate boundary conditions [7]. The general solution is no longer the real part of an analytic function, but rather

$$\chi(z, \bar{z}) = \mathrm{Re}[\bar{z}\phi(z) + \tilde{\psi}(z)], \tag{1}$$

where $\phi(z)$ and $\tilde{\psi}(z)$ are a pair of analytic functions. Thus conformal techniques are not trivially applicable, and until recently there was no appropriate theoretical method to solve such equations with boundary conditions on an arbitrary ramified boundary. Numerical simulations were limited to lattice discretizations [8], even though lattice anisotropy is a relevant perturbation changing the universality class of the growing patterns. Recent progress in the context of quasistatic fracture [9,10] allows us to offer below an appropriate model for bi-Laplacian growth patterns.

To set up the model imagine a two-dimensional elastic medium with a hole of an arbitrary shape, whose boundary $z(s)$ is parametrized by the arc-length variable s. Into this hole one pushes quasistatically a fluid of pressure P. In equilibrium with this pressure the elastic medium will suffer a displacement field $u(\mathbf{r})$. The strain tensor ϵ_{jk} which results is

$$\epsilon_{jk} \equiv \tfrac{1}{2}(\partial_j u_k + \partial_k u_j). \tag{2}$$

In linear elasticity theory [7] the stress tensor is related to the strain tensor by

$$\sigma_{jk} = \frac{E}{1+\sigma}\left(u_{jk} + \delta_{jk}\frac{\sigma}{1-2\sigma}\sum_l u_{ll}\right), \tag{3}$$

where E and σ are material parameters. Equilibrium inside the elastic medium requires that

$$\sum_k \partial_k \sigma_{jk} = 0, \qquad \text{for all } j. \tag{4}$$

The general solution of these equations in two dimensions is given by

$$\sigma_{xx} = \partial_y^2 \chi, \qquad \sigma_{yy} = \partial_x^2 \chi, \qquad \sigma_{xy} = -\partial_{xy}\chi, \tag{5}$$

FIG. 1. Typical pattern when water is injected into a radial Hele-Shaw cell filled with a solution of associated polymers [6].

 © 2002 The American Physical Society

VOLUME 89, NUMBER 23 PHYSICAL REVIEW LETTERS 2 DECEMBER 2002

where the so-called Airy potential χ fulfills the biharmonic equation

$$\nabla^2\nabla^2\chi = 0. \tag{6}$$

The solution is represented, as said, by Eq. (1). In order to develop the growth pattern we need to compute the tangent component of the stress tensor at the boundary of the pattern, since cracking proceeds only if this component exceeds a threshold σ_c. To define this component and to state the conditions on the boundary of the growth pattern we use the local tangent and normal directions. With α being the angle between the tangent and the x axis at $z(s)$, we define derivatives with respect to the tangent and normal directions according to

$$\partial_t = \cos(\alpha)\partial_x + \sin(\alpha)\partial_y, \qquad \partial_n = \cos(\alpha)\partial_y - \sin(\alpha)\partial_x. \tag{7}$$

The pressure P now must be balanced by the normal component of the stress:

$$\partial_{tt}\chi = \sigma_{nn} = -P = \text{const} \tag{8}$$

on the crack. Since in equilibrium no fluid slips along the boundary,

$$-\partial_{tn}\chi = \sigma_{tn} = \sigma_{nt} = 0 \tag{9}$$

on the crack. The normal component $\partial_{nn}\chi = \sigma_{tt}$ is not determined from the boundary conditions, but is *computed* by solving for $\chi(z, \bar{z})$. Using the fact that $4\partial^2\chi/\partial z\partial\bar{z} = \sigma_{xx} + \sigma_{yy} = \sigma_{tt} + \sigma_{nn}$, we can immediately read from Eq. (1)

$$\sigma_{tt}(z) = P + 4\mathrm{Re}[\phi'(z)], \tag{10}$$

at the boundary. Once we have computed the tangent component of the stress, we may advance the crack if $\Delta\sigma \equiv \sigma_{tt}(z) - \sigma_c > 0$, at a speed which is (on the average) proportional to $\Delta\sigma$ [11,12].

Thus to compute the tangent stress and advance the crack we need to determine only the function $\phi(z)$. The boundary conditions (8) and (9) are expressed in terms of $\phi(z)$ and $\tilde{\psi}(z)$ by using (7) in (8) and (9) to derive $\partial_t\partial_{\bar{z}}\chi = -P[\cos(\alpha) + i\sin(\alpha)] = -P\partial_t z(s)$, where we identify $\partial_t z(s)$ as the unit vector tangent to the boundary. Rewriting this condition as $\partial_t[\partial_{\bar{z}}\chi + Pz] = 0$, we obtain the boundary condition on the interface [13]

$$\phi(z(s)) + z(s)\overline{\phi'(z(s))} + \overline{\psi(z(s))} = -Pz(s) + K, \tag{11}$$

where $\psi(z) \equiv \tilde{\psi}'(z)$ and K is a constant that can be chosen zero with impunity.

The boundary conditions at infinity are obvious, since all stress components have to vanish as $z \to \infty$:

$$\partial_{z\bar{z}}\chi(z, \bar{z}) \to 0, \qquad \partial_{zz}\chi(z, \bar{z}) \to 0 \qquad \text{as } z \to \infty. \tag{12}$$

In light of these conditions $\phi(z)$ must have the form $\phi(z) = i\beta_1 z + \sum_{j=0}^{\infty} u_{-j}z^{-j}$ with β_1 real. The solution of the stress field is invariant under the transformation $\phi \to \phi + iAz + B$ with A real and B a complex constant. We can use this freedom to get rid of β_1 and u_0, and write ϕ in the form

$$\phi(z) = \sum_{j=1}^{\infty} u_{-j}z^{-j}. \tag{13}$$

Similarly from (12) it follows that ψ has the form

$$\psi(z) = \sum_{j=1}^{\infty} v_{-j}z^{-j}. \tag{14}$$

To proceed, invoke a conformal map $z = \Phi^{(n)}(\omega)$ that maps the exterior of the unit circle in the mathematical plane ω to the exterior of the crack in the physical plane z, after n growth steps. The conformal map is univalent by construction, with a Laurent expansion

$$\Phi^{(n)}(\omega) = F_1^{(n)}\omega + F_0^{(n)} + F_{-1}^{(n)}/\omega + F_{-2}^{(n)}/\omega^2 + \ldots \tag{15}$$

and $\Phi^{(0)}(\omega) = \omega$. The arclength position s in the physical domain is mapped by the inverse of $\Phi^{(n)}$ onto a position on the unit circle $\epsilon = \exp(i\theta)$. We will be able to compute the stress tensor on the boundary of the crack in the physical domain by performing the calculation on the unit circle. In other words we will compute $\sigma_{tt}(\theta)$ on the unit circle in the mathematical plane.

We perform the calculation iteratively, taking the stress as known for the crack after $n-1$ fracture events. In order to implement the nth cracking event with average velocity proportional to $\Delta\sigma$, we should choose potential positions on the interface more often when $\Delta\sigma(\theta)$ is larger. We construct a probability density $P(\theta)$ on the unit circle $e^{i\theta}$ which satisfies

$$P(\theta) = \frac{|\Phi'^{(n-1)}(e^{i\theta})|\Delta\sigma(\theta)\Theta(\Delta\sigma(\theta))}{\int_0^{2\pi}|\Phi'^{(n-1)}(e^{i\tilde{\theta}})|\Delta\sigma(\tilde{\theta})\Theta(\Delta\sigma(\tilde{\theta}))d\tilde{\theta}}, \tag{16}$$

where $\Theta[\Delta\sigma(\tilde{\theta})]$ is the Heaviside function, and $|\Phi'^{(n-1)}(e^{i\tilde{\theta}})|$ is simply the Jacobian of the transformation from mathematical to physical plane. The next growth position, θ_n in the mathematical plane, is chosen randomly with respect to the probability $P(\theta)d\theta$. At the chosen position on the crack, i.e., $z = \Phi^{(n-1)}(e^{i\theta_n})$, we want to advance the crack with a given step of fixed length $\sqrt{\lambda_0}$. We achieve growth with an auxiliary conformal map $\phi_{\lambda_n,\theta_n}(\omega)$ that maps the unit circle to a unit circle with a semicircular bump of area λ_n centered at $e^{i\theta_n}$ [14,15]. To ensure a fixed size step in the physical domain we choose

$$\lambda_n = \frac{\lambda_0}{|\Phi^{(n-1)\prime}(e^{i\theta_n})|^2}. \tag{17}$$

Finally the updated conformal map $\Phi^{(n)}$ is obtained as

$$\Phi^{(n)}(\omega) = \Phi^{(n-1)}(\phi_{\lambda_n,\theta_n}(\omega)). \tag{18}$$

The recursive dynamics can be represented as iterations of the map $\phi_{\lambda_n,\theta_n}(w)$,

$$\Phi^{(n)}(w) = \phi_{\lambda_1,\theta_1} \circ \phi_{\lambda_2,\theta_2} \circ \cdots \circ \phi_{\lambda_n,\theta_n}(\omega). \tag{19}$$

Every given fracture pattern is determined completely by the random itinerary $\{\theta_i\}_{i=1}^n$.

We can now represent the boundary conditions (10) in terms of $z(s) = \Phi^{(n)}(\epsilon)$:

$$\phi(\Phi^{(n)}(\epsilon)) + \Phi(\epsilon)\frac{\overline{\phi'(\Phi^{(n)}(\epsilon))}}{\overline{\Phi^{(n)\prime}(\epsilon)}} + \overline{\psi(\Phi^{(n)}(\epsilon))} = -P\Phi^{(n)}(\epsilon). \tag{20}$$

To solve this equation we introduce a power expansion for the ratio

$$\frac{\Phi^{(n)}(\epsilon)}{\overline{\Phi^{(n)\prime}(\epsilon)}} = \sum_{j=-\infty}^{\infty} b_j \epsilon^j. \tag{21}$$

Note that this expansion contains both positive and negative powers of ϵ, whereas Eqs. (13) and (14) contained only negative powers. Nevertheless, upon substituting all the power expansions into Eq. (20), one finds that the determination of the function $\phi(z)$ requires only the negative powers of ϵ [10], with the coefficients satisfying the system of equations

$$u_{-l} - \sum_{j=1}^{\infty} j\overline{u}_{-j} b_{-(j+l+1)} = -pF_{-l}. \tag{22}$$

After separating real from imaginary parts, one finds an infinite system of linear equations. In practice we truncate at $j_{\max} = 100$ and test for convergence by increasing the order. Note that the highest resolved $u_{j_{\max}}$ requires computing the Fourier series (21) to order $2j_{\max} + 1$.

Implementing this procedure with $\Phi^{(0)}(\omega) = \omega$, and choosing $\lambda_0 = 1$, we generate a typical fracture pattern as seen in Fig. 2. What is seen is the map $\Phi^{(7000)}(\epsilon)$ which is topologically a circle. The pattern is self-similar throughout the growth, and contrary to the discretized solution of Ref. [8] we have no lattice and no finite boundaries. Accordingly, there are no boundary induced crossovers of the type found there.

While we can guarantee that the pattern seen is indeed an exact bi-Laplacian pattern under the growth rules adopted here, we cannot guarantee that it is identical to any of the experimental patterns reported in [4–6]. This stems from a few reasons. First, in many experiments there is a mixture of viscous and elastic phenomena, to the point that there are examples of a continuum of growth patterns depending on the relative importance of the two [5,6]. In our theory we solved the bi-Laplacian equation after each growth step; this is relevant in the purely elastic limit. Second, and not less importantly, we

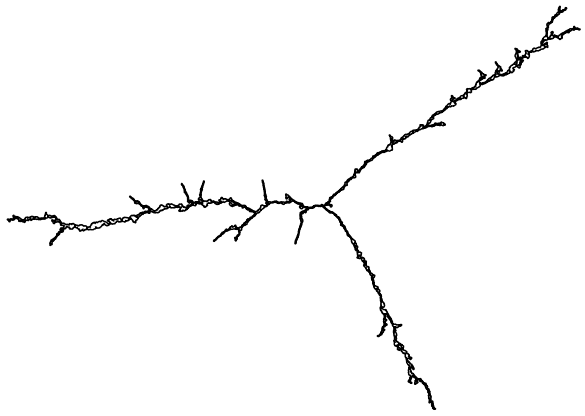

FIG. 2. Typical pattern resulting from a growth of discrete fracture events occurring with the probability $P \approx \Theta(\Delta\sigma)\Delta\sigma$.

advanced the pattern where allowed ($\Delta\sigma > 0$) at a velocity that is proportional (on the average) to $\Delta\sigma$. While this is accepted by a number of authors as a reasonable guess for the rate of growth of a fracture pattern in the quasistatic limit, it is by no means derived from first principles or universally accepted. Needless to say, in our procedure we can adopt any other velocity law without much ado, simply by changing the probability distribution (16). We caution the reader that one does not expect the patterns to be independent of the velocity law [10]. Thus a more complete theory of bi-Laplacian patterns calls for further collaboration between experiments and theory to zero in on a plausible velocity law. Before doing so there is a limited relevance to studying carefully the geometric properties of the patterns obtained with this velocity law or another. Notwithstanding these remarks, we stress that the present theory offers a very convenient tool for assessing the fractal dimension D of the growing patterns. Having a univalent conformal map as in (15), one can invoke the rigorous "1/4" theorem. This theorem states that if R_n is the radius of the minimal circle that contains the pattern after n fracture events, then

$$F_1^{(n)} \le R_n \le 4F_1^{(n)}. \tag{23}$$

Accordingly, one expects that for large n the first Laurent coefficient satisfies

$$F_1^{(n)} \approx \sqrt{\lambda_0} n^{1/D}. \tag{24}$$

One advantage of the present approach is that the first Laurent coefficient $F_1^{(n)}$ is known exactly as

$$F_1^{(n)} = \Pi_{k=1}^n \sqrt{1 + \lambda_k}, \tag{25}$$

which is computable to machine precision. In Fig. 3 we present, in double logarithmic plot, $F_1^{(n)}/\sqrt{\lambda_0}$ vs n. Reading the slope of the least-squares fit yields a dimension $D = 1.4 \pm 0.1$.

VOLUME 89, NUMBER 23 PHYSICAL REVIEW LETTERS 2 DECEMBER 2002

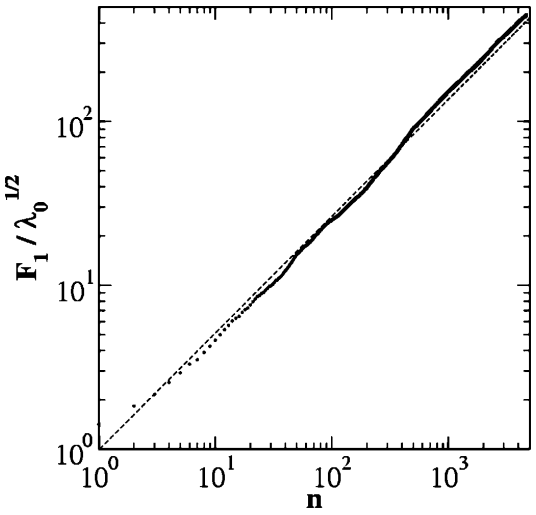

FIG. 3. $F_1^{(n)}/\sqrt{\lambda_0}$ of the pattern in Fig. 2 vs n in a double logarithmic plot. From the slope of the least squares fit we estimate the dimension $D = 1.4 \pm 0.1$.

The method of iterated conformal maps offers convergent calculations of fractal and multifractal properties of the growth patterns. If required, one can use the formalism to obtain highly accurate values of the fractal dimension; cf. [16]. In addition, if the properties of the growth probabilities are of interest from the multifractal point of view, there are available methods to compute these in a convergent scheme [17] that is not available in direct numerical simulations. However, such refinements would be justified only after future work to solidify further the relation between theory and experiment.

We thank Jonathan Tal for his expert help with the SV1 supercomputer at the Weizmann Institute. This work has been supported in part by the Minerva Foundation, Munich, Germany, the Petroleum Research Fund, The European Commission under the TMR program, and the Naftali and Anna Backenroth-Bronicki Fund for Research in Chaos and Complexity.

[1] D. Bensimon, L. P. Kadanoff, S. Liang, B. I. Shraiman, and C. Tang, Rev. Mod. Phys. **58**, 977 (1986).
[2] P. G. Saffman and G. I. Taylor, Proc. R. Soc. London A **245**, 312 (1958).
[3] B. Shraiman and D. Bensimon, Phys. Rev. A **30**, 2840 (1984); S. D. Howison, J. Fluid Mech. **167**, 439 (1986).
[4] A. Lindner, S. Rica, and Y. Couder, in *Proceedings of the Conference on "Recontre du non-Lineaire"* (Paris Onze Editions, Orsay, 1999), p. 68.
[5] E. Lemaire, P. Levitz, G. Daccord, and H. van Damme, Phys. Rev. Lett. **67**, 2009 (1991).
[6] H. Zhao and J. V. Maher, Phys. Rev. E **47**, 4278 (1993).
[7] L. D. Landau and E. M. Lifshitz, *Theory of Elasticity* (Pergamon, London, 1986), 3rd ed.
[8] W. Wang and W. Canessa, Phys. Rev. E **47**, 1243 (1993).
[9] F. Barra, H. G. E. Hentschel, A. Levermann, and I. Procaccia, Phys. Rev. E, **65**, 045101 (2002).
[10] F. Barra, A. Levermann, and I. Procaccia, cond-mat/0205132 [Phys. Rev. E (to be published)].
[11] See, for example, J. Kertész in *Statistical Models for the Fracture of Disordered Media* (North-Holland, Amsterdam, 1990).
[12] H. J. Herrmann and S. Roux, *Statistical Models for the Fracture of Disordered Media* (Ref. [11]), and references therein.
[13] N. I. Muskhelishvili, *Some Basic Problems in the Mathematical Theory of Elasticity* (Noordhoff, Groningen, 1952).
[14] M. B. Hastings and L. S. Levitov, Physica (Amsterdam) **116D**, 244 (1998).
[15] B. Davidovitch, H. G. E. Hentschel, Z. Olami, I. Procaccia, L. M. Sander, and E. Somfai, Phys. Rev. E **59**, 1368 (1999).
[16] B. Davidovitch, A. Levermann, and I. Procaccia, Phys. Rev. E **62**, R5919–R5922 (2000).
[17] B. Davidovitch, M. H. Jensen, A. Levermann, J. Mathiesen, and I. Procaccia, Phys. Rev. Lett. **87**, 164101 (2001).

5 Discussion

The work presented in this thesis deals with the subject of pattern formation in two very different nonlinear physical systems: on the one hand the field of Laplacian growth patterns and on the other hand the propagation of fracture in brittle elastic media.

For the model of Diffusion Limited Aggregation we were able to compute the full fractal spectrum of the harmonic measure and give a geometrical interpretation of its phase transition at a negative $q_c = -0.2 \pm 0.05$. Next to our previous work [37] on the scaling properties of DLA this computation was the first application of the Hastings-Levitov formalism [46] that shows the full power of the approach of iterated conformal maps. Several previous attempts to compute the fractal spectrum of DLA date back more than a decade [40, 41]. These attempts had to be unsuccessful because of the strong variation of the harmonic measure from the fjords to the tips of the cluster and their direct numerical approach. The method of iteration of conformal maps on the contrary provides an analytic expression for the harmonic measure of a DLA cluster. It is therefore possible to compute the measure and specifically its negative moments to machine precision.

In an attempt to understand the relation of Diffusion Limited Aggregation to the hydrodynamic flow in a Hele-Shaw cell, we introduce the $\beta-\mathcal{C}-$model. This model interpolates between DLA and parallel Laplacian growth. We were able to show that parallel growth yields in two-dimensional clusters, i.e. is non-fractal. By arguing that the Hele-Shaw patterns do not have a lower dimension than parallel Laplacian growth patterns, we conjectured that the Hele-Shaw flow is two-dimensional. This conjecture contradicts previous speculations that in the limit of vanishing surface tension Hele-Shaw flow patterns have the same fractal dimension as DLA clusters [13, 81, 82]. In

order to verify this conjecture it would be desirable for the future to further investigate the relation between Hele-Shaw flow in the limit of vanishing surface tension and parallel Laplacian growth. However, the similarity of the clusters which were obtained from direct numerical simulations with the $\beta - \mathcal{C}-$model clusters, are encouraging (compare figure 8). Previous work on Laplacian flows in a channel geometry (Saffman-Taylor problem) were focused on the role of surface tension in the formation of the flow pattern [26-28, 34]. Our work suggests that further analytical insight may be gained by focusing on the parallelity of the growth rather than the surface tension parameter. Since the boundary conditions become much simpler for zero surface tension, an analytic approach might be possible.

The second focus of the thesis is the investigation of quasi-static fracture propagation. We provide a method to compute the stress field outside complex structures for arbitrary loadings. The fracture pattern is given by the conformal map from its exterior to the exterior of the unit circle. In contrast to previous work it is possible to investigate arbitrarily complicated shapes and therefore to compute statistical quantities such as roughness exponents and distributions of branching angles. These quantities can be verified experimentally. Currently, a microscopic theory for fracture propagation is lacking. Candidates for such a theory such as the existence of a plastic process zone [57] or the Grinfeld instability [75, 83] can be implemented in the framework of the presented method. The comparison of the resulting statistical quantities with experimental data can then be used to verify these microscopic theories.

The model of bi-Laplacian growth describes the displacement of viscoelastic material by a fluid in the limit of very high Deborah numbers, i.e. when the elastic effects dominate the viscous ones. Similar to DLA, this

model can be used as a paradigm for the spontaneous emergence of fractals in nature. The bi-Laplacian patterns are qualitatively different from Laplacian DLA patterns. The fractal dimension of the bi-Laplacian clusters is lower than for DLA. Furthermore the branching angles are significantly larger in the biharmonic case than in the harmonic. These differences yield from the elastic nature of the underlying problem and can be examined in experiment. The investigation of the relation of Laplacian and bi-Laplacian growth opens a wide range of possible future work, spanning from the introduction of a combined model for visco-elastic displacement to the investigation of parallelity in the growth as in the $\beta - \mathcal{C}-$model.

A The iteration of conformal maps

The method of iteration of conformal maps provides the technical basis for this dissertation. It was introduced by Hastings and Levitov in 1998 [46]. This appendix contains some basic formulars related to the technique most which have been published elsewhere in less detail [47].

A.1 The fundamental map

The influence of the exact shape of the fundamental map on the resulting clusters has not been fully investigated yet and provides an interesting mathematical challenge in itself. We know that it is crucial that the bump, i.e. the local deformation of the unit circle caused by the map, has to be strictly local. Maps which allow tails that cover the entire unit circle, eventually lead to an unintentional growth in the fjords and numerically to a loss of conformality. Obeying this restriction, different fundamental maps have been used for the generation of clusters [84, 85]. For the work presented in this thesis we used the original map, introduced by Hastings and Levitov in 1998 [46]

$$\phi_j(w) \equiv \phi_{\lambda_j,\theta_j}(w) \equiv e^{i\theta_j}\phi_{\lambda_j}\left(e^{-i\theta_j}w\right) \tag{19}$$

with

$$\phi_\lambda(w) = w^{1-a}\cdot\left[\frac{1+\lambda}{2}\,\frac{1+w}{w}\,\left(1+w+\sqrt{w^2-2\,\frac{1-\lambda}{1+\lambda}\,w+1}\right)-1\right]^a \tag{20}$$

where $0 < a < 1$ determines the aspect ratio of the bump[3]. The map (20) is conformal outside the unit circle. It has two branch points $A_\pm$ on the unit circle

$$A_\pm \equiv e^{\pm i\alpha} \equiv \frac{1-\lambda}{1+\lambda} \pm i\,\frac{2\sqrt{\lambda}}{1+\lambda} \qquad \text{with} \quad \alpha = \arctan\left(\frac{2\sqrt{\lambda}}{1-\lambda}\right) \tag{21}$$

[3]Some investigations on the influence of the aspect ratio have been carried out by Davidovitch et.al. [47]

which are given by the vanishing of the sqare root in (20). These branch points sharply define the borders of the local deformation of the unit circle caused by the map, i.e. for $\theta \notin [-\alpha, +\alpha]$ it is $|\phi_\lambda(e^{i\theta})| = 1$.

Riemanns theorem demands furthermore that the fundamental function, mapping conformally the exteriors of two bounded regions onto each other, grows linearly at infinity. For the given map we get from equation (20)

$$\phi_\lambda(w) \sim (1+\lambda)^a \cdot w \qquad \text{as} \quad w \to \infty \tag{22}$$

Since ϕ_n is conformal, its inverse exists. For the special case $a = 0.5$ it can be easily found to be

$$\phi_j^{-1}(z) \equiv \phi_{\lambda_j,\theta_j}^{-1}(z) \equiv e^{i\theta_j}\phi_{\lambda_j}^{-1}\left(e^{-i\theta_j}z\right) \tag{23}$$

with

$$\phi_\lambda^{-1}(z) = \frac{\sqrt{1+\lambda} - z}{1 - \sqrt{1+\lambda}\, z} \cdot z \tag{24}$$

A.2 The conformal transformation

The property of linear increase at infinity carries over from the fundamental map to its iteration

$$\Phi_n(w) \equiv \phi_n \circ ... \circ \phi_1(w) \sim \left(\prod_{j=1}^{n} (1+\lambda_j)^a\right) \cdot w \qquad \text{as} \quad w \to \infty \tag{25}$$

and its inverse Φ_n^{-1}. Consequently, the field (4) goes logarithmically at infinity

$$P(z) = \Re\left[\log\left(\Phi_n^{-1}(z)\right)\right] \sim \log(|z|) \qquad \text{as} \quad z \to \infty \tag{26}$$

This property garanties the normalizability of the harmonic measure (2) or constant water flux in the terminology of the Hele-Shaw flow. The first Laurent coefficient of Φ_n can be read directly from equation (25)

$$F_1^{(n)} = \prod_{j=1}^{n} (1+\lambda_j)^a \tag{27}$$

$F_1^{(n)}$ is a measure for the radius of the cluster with n bumps $R^{(n)}$ which follows rigorously through the inequalities

$$F_1^{(n)} \leq R^{(n)} \leq 4\, F_1^{(n)} \tag{28}$$

Consequently, in the cases where $\sqrt{\lambda_0}$ is the only length scale in the cluster, simple scaling analysis provides a measure for the mass-radius-dimension D

$$\frac{\lambda_0 \cdot n}{\lambda_0} \sim \frac{\text{cluster area}}{\text{smallest box area}} \sim \left(\frac{\text{cluster radius}}{\text{smallest box length}}\right)^D \sim \left(\frac{F_1^{(n)}}{\sqrt{\lambda_0}}\right)^D \tag{29}$$

Thus in the limit of small particles ($\lambda_0 \to 0$) and large clusters ($n \to \infty$) the first Laurent coeeficient scales as

$$F_1^{(n)} \sim \sqrt{\lambda_0} \cdot n^{1/D} \tag{30}$$

Furthermore, it was shown by Davidovitch, Levermann and Procaccia that even before entering this linear regime, the first Laurent coefficient is a non-linear scaling function of the variable $x \equiv \sqrt{\lambda_0} \cdot n^{1/D}$ [37]. This allows the computation of the fractal dimension D from the early stages of the growth for clusters of the order of ten particles.

B Parallel Laplacian growth and radial Hele-Shaw flow

In both Parallel Laplacian growth as defined through the $\beta - \mathcal{C}-$model with $(\beta = 2, \mathcal{C} = 1)$ and the hydrodynamic flow in a Hele-Shaw cell an interface is propagated according to a Laplacian field $\mathcal{P}$. In the limit of small λ_0 the normal velocity of each point of the interface is proportional to the gradient of the local field, in both models, and the interface advances at all points in parallel. The viscous fingering that occurs in a Hele-Shaw cell is due to an instability of the surface which amplifies perturbations of a circular interface that have a wave number $k < k_{st}$ where the critical wave number k_{st} goes with the surface tension parameter σ as [17]

$$k_{st} \propto \sigma^{-1/2} \tag{31}$$

The $\beta - \mathcal{C}-$model shows the same instability, but the perturbation is intrinsically given in the model through the roughness of the interface due to its composition out of bumps. This roughness tends to zero, i.e. the perturbation decreases, as λ_0 goes to zero. The $\beta - \mathcal{C}-$model for $(\beta = 2, \mathcal{C} = 1)$ is stochastic through the random choice of the position of the first bump in each layer.

The main difference between Parallel Laplacian growth and Hele-Shaw flow is due to the UV-regularization. In the Hele-Shaw cell the surface tension of the displacing fluid determines the boundary condition for the Laplacian field

$$\mathcal{P}_{HS}\left(z(s)\right) = \sigma\kappa\left(z(s)\right) \tag{32}$$

where $z(s)$ is a position on the interface and $\kappa\left(z(s)\right)$ is the curvature of the interface at $z(s)$. Thus the surface tension supresses the growth of small

scale perturbations and therefore provides a UV regularization of the growth, i.e. it prevents the occurence of finit time singularities, such as cusps in the interface.

In the $\beta - \mathcal{C}-$model, on the other hand, the Laplace equation is solved with

$$\mathcal{P}_{\beta\mathcal{C}}\left(z(s)\right) = 0 \tag{33}$$

on the boundary, i.e. no surface tension is applied. The UV regularization is provided by the bumpiness of the interface. The largest wave numbers of the interface is given by the smallest bump added in a given layer. This smallest bump is grown in the deepest fjord of the cluster and not at the tips. It can therefore not lead to a cusp formation.

The described differences between Hele-Shaw flow and Parallel Laplacian growth are mathematically significant since Laplace's equation is solved, in the two cases, with different boundary conditions. We conjecture however that the large scale properties, and in particular the fractal dimension $D = D_0$, of the clusters that are grown by the two models are the same in the limits of small surface tension and small λ_0. Though a mathematical proof of this conjecture has not been achieved yet, the comparison of the clusters shown in figure 8 suggest that neither the particular mechanism of UV regularization nor the particular source of the randomness introduced into the model, determine the large scale structure of the clusters. Similar as in the model of Diffusion Limited Aggregation (DLA) where the microscopical shape of the particles does not determine the macroscopic properties of the clusters. In the case of DLA it was shown [37] that direct numerical simulations with circular particles yield the same dimension of $D = 1.71$ as the Hastings-Levitov algorithm [46] using half-circular particles.

In the presented work we do not use the equality of the large scale prop-

erties of Parallel Laplacian growth clusters and the Hele-Shaw patterns. Instead we argue, that the fractal dimension of the later cannot be smaller than the dimension of the $\beta - \mathcal{C}-$clusters. As described above, the main differences between the β-$\mathcal{C}$-model and the continuous Laplacian growth are the bumpiness of the surface and the character of the UV-regularization. The first can only result in an increased instability and should therefore at most decrease the dimension of the β-$\mathcal{C}$-model compared to the Hele-Shaw flow. A similar argument holds with respect to the difference in UV-regularization. Any finite value of surface tension introduces a length-scale cut-off into the Hele-Shaw problem which is fixed for the duration of the flow. In the β-$\mathcal{C}$-model, on the other hand, the length scale regularization decrease from layer to layer for any positive value of β. This again should favor the development of smaller branches and decreased fractal dimension.

Future work should be done to clarify the exact relationship between the Hele-Shaw flow and Parallel Laplacian growth and put their equivalence in the limit of zero surface tension and $\lambda_0 \to 0$ on a mathematically sound basis.

C The quasi-static limit of fracture propagation

The basic equation for time-dependent elasticity problems is momentum balance, i.e. the so-called the Lamé euqation [67]

$$\partial_{tt}\mathbf{u} = c_d^2 \nabla (\nabla \cdot \mathbf{u}) - c_s^2 \nabla \times (\nabla \times \mathbf{u}) + \mathbf{f} \tag{34}$$

where $\mathbf{u}$ is the displacement vector and $\mathbf{f}$ is an externally applied body force such as gravity. The dilatational wave speed c_d and the shear wave speed c_s are material constants which can be expressed through the density of the material ρ and the Lamé coefficients λ and μ

$$c_d = \sqrt{\frac{\lambda + 2\mu}{\rho}} \quad \text{and} \quad c_s = \sqrt{\frac{\mu}{\rho}} \tag{35}$$

c_d and c_s set the velocity scale for fracture problem. Thus if L is the length of the fracture under consideration than $\tau_{qs} \equiv \max(Lc_d, Lc_s)$ is the time after which elastic waves have traveled the distance of the fracture length.

In order to assess the validity of the assumption of quasi-static fracture propagation the time period τ_{qs} has to be compared to the time period between successive fracture events τ_{fe}. Thus the quasi-static limit is valid if

$$\tau_{fe} \gg \tau_{qs} \equiv \max(Lc_d, Lc_s) \tag{36}$$

References

[1] H.J.S. Hele-Shaw. On the motion of a viscous fluid between two parallel plates. *Nature*, 58:34, 1898.

[2] P.G. Saffman and Sir G. Taylor. The penetration of a fluid into porous medium or hele-shaw cell containing a more viscous liquid. *Proc. R. Soc. London*, A245:312, 1958.

[3] T.A. Witten and L.M. Sander. Diffusion-limited aggregation, a kinetic critical phenomenon. *Phys. Rev. Let.*, 47(19):1400, 1981.

[4] E. Ben-Jacob, R. Godbey, N.D. Goldenfeld, J. Koplik, H. Levine, T. Mueller, and L.M. Sander. Experimental demonstration of the role of anisotropy in interfacial pattern formation. *Phys. Rev. Let.*, 55:1315, 1985.

[5] Y. Couder, N. Gérard, and M. Rabaud. Narrow fingers in the saffman-taylor instability. *Phys. Rev. A*, 34:5175, 1986.

[6] E. Ben-Jacob, G. Deutscher, P. Garik, N.D. Goldfeld, and Y. Lareah. Formation of a dense branching morphology in interfacial growth. *Phys. Rev. Let.*, 57(15):1903, 1986.

[7] S.N. Rauseo, Jr. P.D. Barnes, and J.V. Maher. Development of radial fingering patterns. *Phys. Rev. A*, 35(3):1245, 1987.

[8] P. Tabeling, G. Zocchi, and A. Libchaber. An experimental study of the saffman-taylor instability. *Journal of Fluid Mechanics*, 177:67, 1987.

[9] A. Arnéodo, Y. Couder, G. Grasseau, V. Hakim, and M. Rabaud. Uncovering the analytical saffman-taylor finger in unstable viscous fingering and diffusion-limited aggregation. *Phys. Rev. Let.*, 63(9):984, 1989.

[10] V. Fleury, M. Rosso, J.-N. Chazalviel, and B. Sapoval. Experimental aspects of dense morphology in copper electrodeposition. *Phys. Rev. A*, 44(10):6693, 1991.

[11] M.G. Moore, A. Juel, J.M. Burgess, W.D. McCormick, and H.L. Swinney. Fluactuations in viscous fingering. *Phys. Rev. E*, 65:R030601, 2002.

[12] P. Meakin. Diffusion-controlled cluster formation in 2–6-dimensional space. *Phys. Rev. A*, 27:1495, 1983.

[13] L. Paterson. Diffusion-limited aggregation and two-fluid displacements in porous media. *Phys. Rev. Let.*, 52(18):1621, 1984.

[14] T.C. Halsey, P. Meakin, and I. Procaccia. Scaling structure of the surface layer of diffusion-limited aggregates. *Phys. Rev. Let.*, 56(8):854, 1986.

[15] A.J. Degregoria and L.W. Schwartz. A boundary-integral method for two-phase displacement in hele-shaw cells. *Journal of Fluid Mechanics*, 164:383, 1986.

[16] C. Amitrano, P. Meakin, and H.E. Stanley. Fractal dimension of the accessible perimeter of diffusion-limited aggregation. *Phys. Rev. E*, 40(3):1713, 1989.

[17] T.Y. Hou, J.S. Lowengrub, and M.J. Shelley. Removing the stiffness from interfacial flows with surface tension. *Journ. Comp. Phys.*, 114:312, 1994.

[18] E. Somfai, L.M. Sander, and R.C. Ball. Scaling and crossovers in diffusion limited aggregation. *Phys. Rev. Let.*, 83:5523, 1999.

[19] D.A. Kessler and H. Levine. Microscopic selection of fluid fingering patterns. *Phys. Rev. Let.*, 86:4532, 2001.

[20] J.W. McLean and P.G. Saffman. The effect of surface tension on the shape of fingers in a hele-shaw cell. *Journal of Fluid Mechanics*, 192:455, 1981.

[21] J.-L. Vanden-Broeck. Fingers in a hele-shaw cell with surface tension. *Phys. Fluids*, 26:2033, 1983.

[22] B.I. Shraiman and D. Bensimon. Singularities in nonlocal interface dynamics. *Phys. Rev. A*, 30(5):2840, 1984.

[23] N.G. Makarov. On the distortion of boundary sets under conformal mappings. *Proc. London Math. Soc.*, 51:369, 1985.

[24] L.A. Turkevich and H. Scher. Occupancy-probability scaling in diffusion-limited aggregation. *Phys. Rev. Let.*, 55:1026, 1985.

[25] D. Bensimon, L.P. Kadanoff, S. Liang, B.I. Shraiman, and C. Tang. Viscous flows in two dimensions. *Review of Modern Physics*, 58(4):977, 1986.

[26] B.I. Shraiman. Velocity selection and the saffman-taylor problem. *Phys. Rev. Let.*, 58(19):2028, 1986.

[27] R. Combescot, T. Dombre, V. Hakim, Y. Pomeau, and A. Pumir. Shape selection of saffman-taylor fingers. *Phys. Rev. Let.*, 58(19):2036, 1986.

[28] D.C. Hong and J.S. Langer. Analytic theory of the selection mechanism in the saffman-taylor problem. *Phys. Rev. Let.*, 58(19):2032, 1986.

[29] T.C. Halsey. Some consequences of an equation of motion for diffuse growth. *Phys. Rev. Let.*, 59:2067, 1987.

[30] P.W. Barker and R.C. Ball. Real-space renormalization of diffusion-limited aggregation. *Phys. Rev. A*, 42(10):6289, 1990.

[31] R. Catiero, L. Pietronero, and A. Vespignani. Persistence of screening and self-criticality in the scale invariant dynamics of diffusion limited aggregation. *Phys. Rev. Let.*, 70:3939, 1993.

[32] T.C. Halsey. Diffusion-limited aggregation as branched growth. *Phys. Rev. Let.*, 72(8):1228, 1994.

[33] M.B. Mineev-Weinstein and R. Mainieri. Observation of conservation laws in diffusion limited aggregation. *Phys. Rev. Let.*, 72(6):880, 1994.

[34] M. Siegel and S. Tanveer. Singular perturbation of smoothly evolving hele-shaw solutions. *Phys. Rev. Let.*, 76(3):419, 1996.

[35] M.B. Mineev-Weinstein, P.B. Wiegmann, and A. Zabrodin. Integrable structure of interface dynamics. *Phys. Rev. Let.*, 84:5106, 2000.

[36] B. Davidovitch and I. Procaccia. Analytic theory of fractal growth patterns in 2 dimensions. *Phys. Rev. Let.*, 85:3608, 2000.

[37] B. Davidovitch, A. Levermann, and I. Procaccia. Convergent calculation of the asymptotic dimension of diffusion limited aggregation: Scaling and renormalization of small clusters. *Phys. Rev. E*, 62:R5919, 2000.

[38] M.B. Hastings. Scale-invariant branch distribution from a soluble stochastic model. *Journal of Statistical Physics*, 107:1031, 2002.

[39] M.J. Feigenbaum, I. Procaccia, and B. Davidovich. Dynamics of finger formation in laplacian growth without surface tension. *Journal of Statistical Physics*, 103(5/6):973, 2001.

[40] J. Lee and H.E. Stanley. Phase transition in the multifractal spectrum of diffusion-limited aggregation. *Phys. Rev. Let.*, 61:2945, 1988.

[41] A.B. Harris and M. Cohen. Scaling of negative moments of the growth probability of diffusion-limited aggregates. *Phys. Rev. A*, 41:971, 1990.

[42] R.C. Ball and R. Blumenfeld. Exact results on exponential screening in two-dimensional diffusion-limited aggregation. *Phys. Rev. A*, 44(2):R828, 1991.

[43] C. Amitrano, A. Coniglio, and F. di Liberto. Growth probability distribution in kinetic aggregation processes. *Phys. Rev. Let.*, 57(8):1019, 1986.

[44] T.C. Halsey, B. Duplantier, and K. Honda. Multifractal dimensions and their fluctuations in diffusion-limited aggregation. *Phys. Rev. Let.*, 78:1719, 1997.

[45] H.G.E. Hentschel and I. Procaccia. The infinite number of generalized dimensions of fractals and strange attractors. *Physica D*, 8:435, 1983.

[46] M.B. Hastings and L.S. Levitov. Laplacian growth as one-dimensional turbulence. *Physica D*, 116:244, 1998.

[47] B. Davidovitch, H.G.E. Hentschel, Z. Olami, I. Procaccia, L.M. Sander, and E. Somfai. Diffusion limited aggregation and iterated conformal maps. *Phys. Rev. E*, 59(2):1368, 1999.

[48] F. Barra, B. Davidovitch, and I. Procaccia. Iterated conformal dynamics and laplacian growth. *Phys. Rev. E*, 65:046144, 2002.

[49] J. Fineberg S.P. Gross, M. Marder, and H.L. Swinney. Instability in dynamics fracture. *Phys. Rev. Let.*, 67:457, 1991.

[50] K.J. Måløy, A. Hansen, and E.L. Hinrichsen. Experimental measurements of the roughness of brittle cracks. *Phys. Rev. Let.*, 68:213, 1992.

[51] E. Sharon, S.P. Gross, and J. Fineberg. Local crack branching as a mechanism for instability in dynamic fracture. *Phys. Rev. Let.*, 74:5096, 1995.

[52] E. Sharon, S.P. Gross, and J. Fineberg. Energy dissipation in dynamic fracture. *Phys. Rev. Let.*, 76:2117, 1996.

[53] E. Bouchaud. Scaling properties of cracks. *J. Phys.: Condens. Matter*, 9:4319, 1997.

[54] P. Daguier, B. Nghiem, E. Bouchaud, and F. Creuzet. Pinning and depinning of crack fronts in heterogeneous materials. *Phys. Rev. Let.*, 78:1062, 1997.

[55] J.F. Boudet and S. Ciliberto. Interaction of sound with fast crack propagation. *Phys. Rev. Let.*, 80:341, 1998.

[56] J. Fineberg and M. Marder. Instability in dynamic fracture. *Physics Reports*, 313, 1999.

[57] H.J. Herrmann and S. Roux. *Statistical Models for the Fracture of Disordered Media.* North Holland Amsterdam, 1990.

[58] P. Meakin. Stress distribution for a rigid fractal embedded in a two-dimensional elastic medium. *Phys. Rev. A*, 36:325, 1987.

[59] W. Wang and E. Canessa. Biharmonic pattern selection. *Phys. Rev. E*, 47:1243, 1993.

[60] F.F. Abraham, D. Brodbeck, R.A. Rafey, and W.E. Rudge. Instability dynamics of fracture: A computer simulation investigation. *Phys. Rev. Let.*, 73:272, 1994.

[61] S.I. Heizler, D.A. Kessler, and H. Levine. Mode-i fracture in a nonlinear lattice with viscoelastic forces. *Phys. Rev. E*, 66, 2002.

[62] J.G. Swadener, M.I. Baskes, and M. Nastasi. Molecular dynamics simulation of brittle fracture in silicon. *Phys. Rev. Let.*, 89:085503, 2002.

[63] S. Ramanathan, D. Ertac, and D.S. Fisher. Quasistatic crack propagation in heterogeneous media. *Phys. Rev. Let.*, 79:873, 1997.

[64] S. Ramanathan and D.S. Fisher. Dynamics and instabilities of planar tensile cracks in heterogeneous media. *Phys. Rev. Let.*, 79:877, 1997.

[65] N.I. Muskhelishvili. *Some basic problems of the mathematical theory of elasticity.* P. Noordhoff Ltd, 1953.

[66] L.D. Landau and E.M. Lifschitz. *Theory of Elasticity.* Pergamon, London, 3rd edition, 1986.

[67] L.B. Freund. *Dynamic fracture mechanics.* Cambridge University Press, 1998.

[68] M. Kardar, G. Parisi, and Y.-C. Zhang. Dynamic scaling of growing interfaces. *Phys. Rev. Let.*, 56, 1986.

[69] L.S. Aranson, V.A. Kalatsky, and V.M. Vinokur. Continuum field description of crack propagation. *Phys. Rev. Let.*, 85:118, 2000.

[70] A. Karma, D.A. Kessler, and H. Levine. Phase-field model of mode iii dynamic fracture. *Phys. Rev. Let.*, 87, 2001.

[71] K. Kassner, C. Misbah, J. Müller, J. Kappey, and P. Kohlert. Phase-field modelling of stress-induced instabilities. *Phys. Rev. E*, 63, 2001.

[72] L.O. Eastgate, J.P. Sethna, M. Rauscher, and T. Cretegny. Fracture in mode i using a conserved phase-field model. *Phys. Rev. Let.*, 65:036117, 2002.

[73] H. Zhao and J.V. Maher. Associating-polymer effects in a hele-shaw experiment. *Phys. Rev. E*, 47:4278, 1993.

[74] E. Lemaire, P. Levitz, G. Daccord, and H. Van Damme. From viscous fingering to viscoelastic fracturing in colloidal fluids. *Phys. Rev. Let.*, 67:2009, 1991.

[75] E.A. Brener and V.I. Marchenko. Surface instabilities in cracks. *Phys. Rev. Let.*, 81:5141, 1998.

[76] A. Levermann and I. Procaccia. New algorithm for parallel laplacian growth by iterated conformal maps. *Phys. Rev. Let.*, 2003. (submitted).

[77] Sir H. Lamb. *Hydrodynamics.* Dover Publications, 1945. Reprint from 1879.

[78] G.K. Batchelor. *An introduction to fluid dynamics.* Cambridge University Press, 1967.

[79] E. Guyon, J.-P. Hulin, L. Petit, and C.D. Mitescu. *Physical Hydrodynamics.* Oxford University Press, 2001.

[80] A. Lindner, S. Rica, and Y. Couder. Digitation visqueuse dans une mousse. In *rencontre du non-linéaire 1999*, 1999.

[81] T. Vicsek. *Fractal growth phenomena.* World Scientific, 1992.

[82] T. Vicsek, M. Shlesinger, and M. Matsushita, editors. *Fractals in natural science*. World Scientific, 1994.

[83] M.A. Grinfeld. Instability of the separation boundary between a non-hydrostatically stressed elastic body and a melt. *Sov. Phys. Dokl.*, 31:831, 1986. originally in: Dokl. Akad. Nauk SSSR 282:1139, 1985.

[84] M.G. Stepanov and L.S. Levitov. Laplacian growth with separately controlled noise and anisotropy. *Phys. Rev. E*, 63:061102, 2001.

[85] R.C. Ball, N.E. Bowler, L.M. Sander, and E. Somfai. Off-lattice noise reduction and the ultimate scaling of diffusion-limited aggregation in two dimensions. *Phys. Rev. E*, 66:026109, 2002.

Acknowledgments

I would like to thank Itamar Procaccia for his endless enthusiasm which often revived my own. The close scientific contact he shares with his colleagues and students is an inspiration. I am grateful for his support during my time in Israel and the not always easy period of my Ph.D. I could not have had a better advisor.

I am grateful to Felipe Barra for the discussions about science and about life in general. I hope that I learned from his patience, kindness and scientific accuracy. It is wonderful to have these qualities combined in one person.

Yoram Cohen was rarely tired to discuss Israeli politics with me and I am grateful for his support, his critical point of view and the inside into Israeli society that I obtained from it.

I would like to thank George Hentschel for the close colaboration and exciting discussions we shared during his visits to the Weizmann Institute.

Many people supported me during my time at the Institute. For this I am grateful to Anna Pomyalov, Batya Reindorf, Benny Davidovitch, David Mukamel, Eli Tziperman, Joel Stavans, Peter Stern, Tali Arbus, Tomer Volansky.

Thank you to Armin, Bernhard, Claude, Debby, Felipe, Holger, Jara, Kadmiel, Kika, Liz, Marco, Michel, Monika, Nina, Paolo and Yoram for being friends.